Infrared and Thermal-Desorption Spectroscopy of H_2 and D_2 in Metal Organic Frameworks

an Honors Thesis presented to
the Department of Physics and Astronomy
of Oberlin College

Kai Shinbrough
March 2017

To my Grandmother Elaine and to my Mother Kathryn, the smartest and the wisest people I know...

Executive Summary

In this thesis we provide an introduction to the use of Metal-Organic Frameworks (MOFs) for hydrogen storage and for the separation of hydrogen isotopologues, H_2 and D_2. MOFs are a class of materials comprised of 'building-block' metal-oxide clusters connected by organic ligands, which have the capacity to adsorb molecules such as hydrogen through weak, physisorptive mechanisms. We provide some background on the quantum mechanical structure of hydrogen isotopologues, the structure of a few state-of-the-art MOFs, the quantum mechanics of infrared spectroscopy, and the desorption dynamics of adsorbates generally. We provide a description of the experimental apparatus and procedure used in this work to acquire thermal desorption (TD) and simultaneous, *in situ* infrared (IR) spectra. Notably, this apparatus makes use of a pressure gauge to record TD spectra—to the best of the author's knowledge, this is the first time such an apparatus has been created and shown to produce reproducible, physically-informative TD spectra. We demonstrate the potential of this novel spectroscopic technique on three MOFs, as we report their respective TDS and IR signatures. The agreement between our TDS and IR techniques is remarkable, as is the amount of information apparent in the TD spectra, and the agreement of our TD spectra with those in the literature. With our simple technique we are able to clearly distinguish the TD spectra of H_2 and D_2, allowing for the evaluation of MOFs with respect to their isotopologue separating ability.

In addition to a proof of concept as to the proficiency of the experimental apparatus, this work presents two main findings: that the desorption of hydrogen isotopologues from MOFs does not follow the coverage-independent Polanyi-Wigner equation, and that stronger binding MOFs exhibit diminishing returns with respect to their ability to separate hydrogen isotopologues via temperature programming.

As we argue on several occasions in this thesis, the TD spectra of hydrogen desorbing

from the MOFs examined with our technique do not obey the coverage-independent Polanyi-Wigner equation. This is foremost demonstrated by the poor *ab initio* fits of our spectra to the equation. This result is also corroborated by the coverage dependence of the TD spectra of Co-MOF-74 (dobdc), however, and further by the ramp rate dependence of these spectra. In demonstrating this result, we advise against the use of the coverage-independent Polanyi-Wigner equation—and analysis techniques based off of it—when considering the desorption of hydrogen from MOFs. As these techniques have begun to feature prominently in the literature, this result proves exceedingly pertinent.

We arrive at the latter conclusion by examining the MOFs reported on as a group, and examining the separation of H_2 and D_2 TD peaks as a function of MOF binding energy. We conclude through experimental as well as through computational techniques that the prospect of temperature-programmed separation through total desorption of H_2 and total adsorption of D_2 is exceedingly bleak. This surprising result rules out the most straightforward use of MOFs for hydrogen isotopologue separation, what we name Zero Point Energy Separation (ZPES) at a single site. As the field surrounding MOFs tacitly assumes this as a promising possibility, again this result proves exceedingly pertinent. The prospect of more imaginative uses of MOFs for temperature-programmed isotopologue separation remains open, as does the possibility of isotopologue separation through other mechanisms involving MOFs.

Contents

List of Figures

List of Tables

Chapter 1: Introduction and Background

1.1 Motivation

1.1.1 H_2 – D_2 Separation

Increasingly dire environmental consequences, rising cost, and unreliable access point to the unsustainability of the United States' reliance on fossil fuels [1]. On the other hand, the abundance and accessibility of molecules containing hydrogen along with the negligible environmental effects associated with its consumption point toward the viability of hydrogen as a dependable, domestic fuel source [1–3]. There is accordingly ample motivation for adopting the so called "hydrogen economy," and while the remaining challenges for its realization are not small in magnitude, they are few in number. According to the most recent United States Department of Energy (DOE) report on hydrogen and fuel cell technologies, these remaining challenges are: mitigating the cost of hydrogen production, arriving at a viable method for hydrogen storage, and creating the infrastructure necessary for hydrogen delivery from production to storage to use [4]. The lattermost of these challenges we take to be primarily an issue of economic and governmental incentive. The challenge of mitigating hydrogen production cost, as well as the challenge of efficiently storing hydrogen, however, falls in the purview of scientific inquiry. This work is directed, in part, toward addressing these two key challenges. This section will further motivate and describe an integral part of the effort to mitigate the cost of hydrogen production, namely the purification and separation of hydrogen from other gases, while Section 1.1.2 will address the challenge of hydrogen storage.

Hydrogen is currently industrially produced through four main processes: the gasification of coal, the steam reforming of natural gas, the dissociation of ammonia, and the electrolysis of water [5]. In all of these processes there is a demonstrable need for efficient, high-volume gas separation, specifically in the preparing of input gas streams, separating of process gases, and purifying of output streams [3]. The separation of molecular hydrogen (H_2) and its isotopologue molecular deuterium (D_2) is of particular interest, as the separated deuterium can be used in a number of applications ranging from neutron moderation in nuclear reactors [6] to drug development and medical detection as a tracer element [7, 8]. The separation of D_2 from H_2 is also, given the similarity of the gases, considerably more difficult than the separation of H_2 and other gases; if a more economically viable method for the separation of H_2 and D_2 is achieved, the process may be transferable to the separation of H_2 from other gases, and thus may help mitigate the cost of hydrogen production. Table 1.1 summarizes the possible processes for industrial separation of 'light' water (H_2O) and 'heavy' water (D_2O), though only water electrolysis, distillation techniques, and chemical exchanges have been used commercially [6]. (More information on each process is available in Ref. [6].) This separation of light and heavy water is a proxy for the separation of molecular hydrogen and deuterium. There is currently no fast, energy efficient process for this separation that possesses a large separation factor (>5).

A body of research motivated by this lack of a suitable process for H_2–D_2 separation has formed around Metal Organic Frameworks (MOFs) and other nanoporous adsorbents, which have the potential to selectively adsorb deuterium out of a gaseous hydrogen-deuterium mixture [9]. MOFs are porous crystalline structures with extremely large surface area densities, and are comprised of metal-oxide clusters connected by organic ligands [10]. The chief interest in and advantage of MOFs is their "chemical tunability"—MOFs can be synthesized in a variety of structures with differing adsorption characteristics, surface area densities, and porosities by connecting different metal-oxide clusters with different organic ligands in a building-block fashion [10]. The separation factor, or selectivity, of MOFs and other adsorbents (α) is defined as the ratio in equilibrium of the molar fraction of D_2 in the adsorbed (θ) and gas (x) phases over that fraction for H_2:

$$\alpha = \frac{\theta_{\mathrm{D_2}}/\mathrm{x}_{\mathrm{D_2}}}{\theta_{\mathrm{H_2}}/\mathrm{x}_{\mathrm{H_2}}}. \tag{1.1}$$

MOFs have the advantage of fast natural exchange rates, and MOF selectivities as high as 12 have been reported in the literature at 60 K [11]. Though no comprehensive study has been performed on the energy efficiency and cost of gas separation processes involving

Process	Separation Factor	Energy Use	Natural Exchange Rate
Distillation of H_2O	1.015 - 1.055	Very High	Moderate - Slow
Distillation of Liquid H_2	1.5	Moderate	Slow
Water Electrolysis	5 - 10	Very High	Fast
Laser Isotope Separation	>20,000	Moderate	Slow
Water-Hydrogen Sulphide Exchange	1.8 - 2.3	High	Fast
Ammonia-Hydrogen Exchange	2.8 - 6	Moderate	Slow - Catalyst Needed
Amino-Methane-Hydrogen Exchange	3.5 - 7	Moderate	Slow - Catalyst Needed
Water-Hydrogen Exchange	2 - 3.8	Moderate	Negligible - Catalyst Needed

Table 1.1: Industrial processes for the separation of light water (H_2O) and heavy water (D_2O), respective separation factors, and qualitative descriptions of the energy needed and the natural exchange rates for each process, adapted from Ref. [6]. None of these processes possess a high separation factor (>5), energy efficiency, and a fast natural exchange rate.

MOFs, they are widely considered to be a promising technology for hydrogen isotopologue separation [3, 4, 9–13].

There are two mechanisms that usually underly the separating ability of MOFs, and other porous adsorbents generally: Kinetic Quantum Sieving (KQS), and what is referred to in the literature as Chemical Affinity Quantum Sieving (CAQS) [12]. First proposed by Beenakker, et al., KQS is a mechanism by which adsorbents with pore diameters on the order of the molecular hard-core of H_2 (∼0.24-0.31 nm) plus its de Broglie wavelength (∼0.1 nm at 77 K) can sieve D_2 out of an isotopologue mixture [14]. This sieving occurs due to the presence of a higher diffusion barrier for lighter isotopologues with larger de Broglie wavelengths, and, at low temperature, results in heavier isotopologues diffusing more rapidly into the porous material [14]. CAQS, on the other hand, is a somewhat misleading name for the sieving process wherein D_2 is preferentially adsorbed onto a strongly attracting adsorption site [12]. The different molecular masses of hydrogen's isotopologues result in different zero point energies when these isotopologues are adsorbed, and this difference in zero point energy leads to a difference in adsorption enthalpy that favors the adsorption of more massive isotopes. Assuming the site potential can be modeled as a simple harmonic oscillator, this zero point energy is proportional to the angular frequency of the isotopologue in its ground state (ω), and this angular frequency is inversely proportional to the square root of the isotopologues molecular mass (m). In general then, isotopologues with larger mass have smaller zero point energies and larger adsorption enthalpies. For the quantum simple harmonic oscillator, the zero point energy (E_0) of a hydrogen isotopologue in a quadratic potential well is given by:

$$E_0 = \frac{1}{2}\hbar\omega, \tag{1.2}$$

where $\hbar$ is the reduced Planck constant [15]. Since the angular frequency ω is given by:

$$\omega = \sqrt{\frac{k}{m}}, \tag{1.3}$$

where k is the characteristic spring constant [15], those molecules with larger mass have smaller zero point energies. Given that for the case of hydrogen isotopologues these masses are constant (and differ by a multiple of the mass of a neutron), if our goal is to maximize the difference in zero point energy, we want to maximize k—a measure of how attractive the adsorption site is. In the case of hydrogen adsorption in porous adsorbents, this means that those adsorbents with higher magnitude adsorption enthalpies, or stronger binding energies (E_b), lead to larger separations in the zero point energies of hydrogen isotopologues; Figure 1.1 displays this relationship qualitatively for a more physical potential well (in this case, the Buckingham Potential). As alluded to above, the term Chemical Affinity Quantum Sieving is at least slightly misleading, as all hydrogen isotopologues are chemically identical. As this process relies on the exploitation of differing zero point energies, we instead refer to this process as Zero Point Energy Separation (ZPES) in the remainder of this work.

Within ZPES, there are two straightforward ways to achieve isotope separation: through what we will call the 'preferential adsorption' mechanism and the 'temperature-programmed separation' mechanism. For ease of notation we will limit the discussion of these options to MOFs, though it is important to note that they apply to all porous adsorbents.

In the more straightforward case of preferential adsorption, a gaseous isotopic mixture is loaded into a MOF (or any porous substrate), and that MOF preferentially adsorbs heavier isotopologues in proportion to its selectivity. This process is depicted in Figure 1.2.

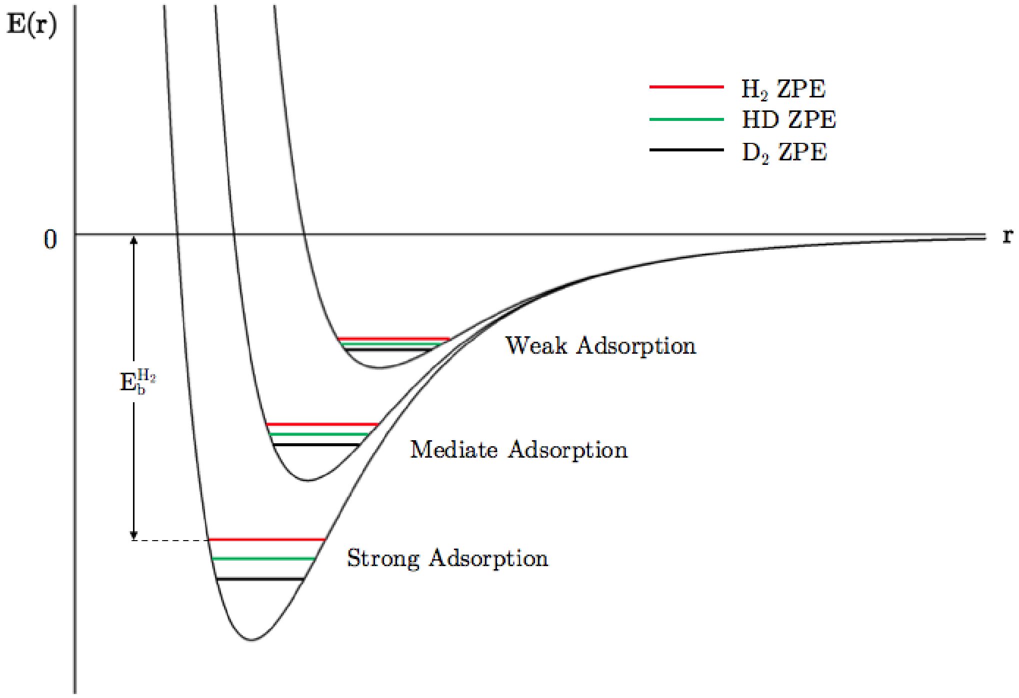

Figure 1.1: Qualitative depiction of Zero Point Energy Separation (ZPES), adapted from Ref. [13]. Owing to its smaller molecular mass, H_2 has a larger zero point energy than the heavier hydrogen isotopologues, and thus experiences a weaker binding energy when interacting with a MOF. The independent variable ‘r’ refers to the location of the adsorbed species’ center of mass.

To elucidate the process, consider the case of a MOF with selectivity $\alpha = 4$ (for D_2 over H_2) and 100 adsorption sites. If this MOF is exposed to a large amount of gaseous H_2 and D_2 in a 50:50 mixture at a temperature below the MOF’s characteristic temperature of adsorption (∼77 K in Figure 1.2), 4 times as many D_2 molecules will be adsorbed as H_2. The remaining gaseous mixture will thereby be depleted of D_2, and the adsorbed mixture will be enriched to a 20:80 H_2 to D_2 mixture. By exposing the MOF to a large amount of gaseous H_2 and D_2, we are effectively taking the limit of large x_{D_2} and x_{H_2} in the selectivity Equation (1.1). In this way we arrive at the ratio of adsorbed D_2 (θ_{D_2}) to H_2 (θ_{H_2}) of α (in our example, 4):

$$\lim_{x_{D_2}\to\infty}\lim_{x_{H_2}\to\infty}\alpha = \lim_{x_{D_2}\to\infty}\lim_{x_{H_2}\to\infty}\frac{\theta_{D_2}/x_{D_2}}{\theta_{H_2}/x_{H_2}} = \frac{\theta_{D_2}}{\theta_{H_2}} = \alpha. \tag{1.4}$$

The remaining unadsorbed gaseous mixture can be evacuated and cycled to another mass of unsaturated MOF before heating the system to release the 20:80 adsorbed mixture.

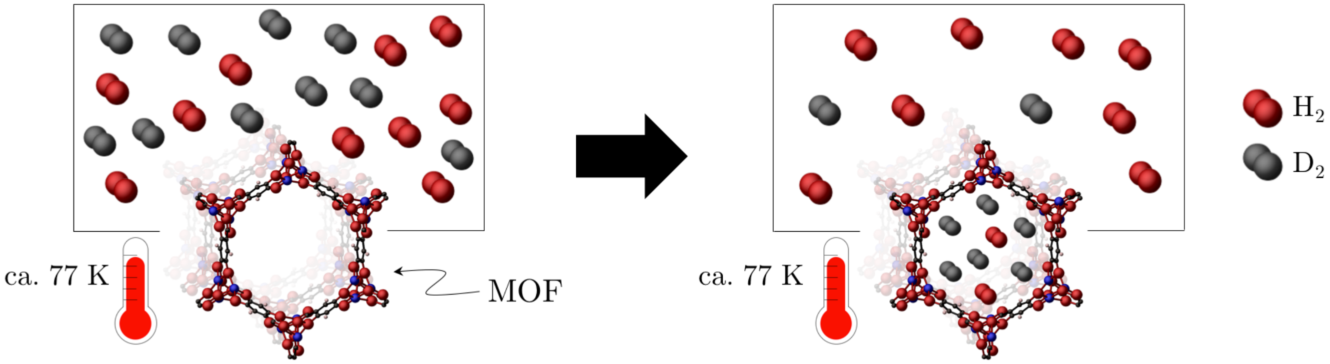

Figure 1.2: Qualitative depiction of the preferential adsorption mechanism for ZPES. A MOF exposed to a large amount H_2:D_2 mixture at some temperature below the characteristic temperature of adsorption (∼77 K) will preferentially adsorb D_2 according to the ratio determined by the MOF's selectivity. The remaining gas has been depleted of D_2.

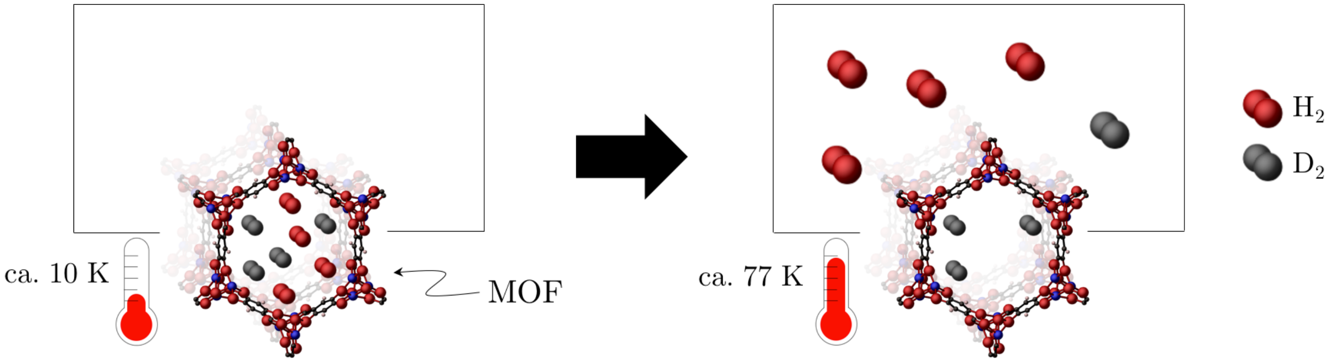

Figure 1.3: Qualitative depiction of the temperature-programmed separation mechanism for ZPES. A MOF exposed to an amount of H_2 and D_2 with total number of molecules less than or equal to the MOF's number of adsorption sites will, at some sufficiently low temperature (∼10 K), adsorb all molecules of both isotopologue. Upon heating to a characteristic temperature of desorption (∼77 K), all H_2 molecules will desorb while some D_2 will remain in the adsorbed phase. The resulting gas has been depleted of D_2 and the adsorbed phase has been enriched.

Depicted in Figure 1.3 is the mechanism of temperature-programmed separation. While the preferential adsorption mechanism for separation relies on gas-adsorbed phase equilibrium and exploitation of the MOF's selectivity, the temperature-programmed mechanism relies on kinetics and driving the system out of equilibrium. In this scheme, a MOF is exposed to an amount of an isotopic mixture with total number of molecules less than or equal to the number of adsorption sites in the MOF. The MOF is then cooled to a sufficient temperature such that near-all the gas molecules are adsorbed (∼10 K in Figure 1.3). Upon heating the MOF to a characteristic temperature of desorption (∼77 K in Figure 1.3), gas molecules of higher zero point energy will desorb at a faster rate than those of lower zero point energy, and the resulting gaseous mixture will be depleted of higher mass isotopologues while the adsorbed phase mixture will be enriched with these isotopologues. We can understand the presence of this characteristic temperature with consideration of the following argument: Given that the probability of a molecule desorbing from a MOF increases exponentially with temperature, upon heating the MOF at a constant rate the majority of adsorbed molecules will desorb at a some temperature which is mainly determined by the binding energy. Since the binding energy of hydrogen isotopologues depend on their zero point energy, each isotopologue will have a different, characteristic temperature. If this difference in characteristic temperature is large enough, heating followed by evacuation can be used to separate out molecules in a manner reminiscent of distillation. For the example case of a MOF with 100 adsorption sites, suppose 50 molecules of H_2 and 50 molecules of D_2 are exposed to the MOF and the system is cooled to a temperature such that all 50 molecules of each isotopologue are adsorbed. If the temperature of the system is raised to some characteristic temperature of desorption and is left at this temperature for a sufficient period of time, all 50 H_2 molecules will have desorbed, while most—say 40—D_2 molecules will not have. This process results in a gaseous mixture with a H_2:D_2 ratio of 50:10, and an adsorbed phase purely of D_2. Again the molecules in the gas phase can be cycled into another mass of unsaturated MOF for further purification, while the adsorbed mixture can be heated until it is simply gas phase D_2.

It is perhaps worth noting that the temperatures in Figures 1.2 and 1.3 are not based on physical information other than the author's observation that 77 K seems to be sufficient to adsorb hydrogen isotopologues in most MOFs, while to the best of the author's knowledge 10 K is sufficient to adsorb hydrogen isotopologues in all MOFs.

The work presented in this thesis primarily applies to the temperature-programmed separation mechanism of ZPES in MOFs. Through a novel form of Thermal-Desorption Spectroscopy (TDS), the desorption characteristics and selectivity of several MOFs are explored. The results attained through this TDS technique are corroborated by a well-established infrared spectroscopic approach throughout. The MOFs investigated in this thesis may or may not come to be used commercially—all that can be said with certainty is that they exhibit selectivities higher than the processes currently in commercial use. The work presented in this thesis should accordingly be interpreted as a proof of concept rather than an attempt to establish an industrially competitive system. Investigation of these MOFs also sheds light upon the adsorption and desorption characteristics of MOFs generally, and can aid in the intentional design of MOFs with larger selectivities. As the body of research on MOF synthesis grows, it is evident that in order to create a MOF more suitable for gas separation or hydrogen storage, physically-informed structural decisions must be made—there are simply too many combinations of ligands and metal groups to systematically synthesize and test each in the search for an optimally binding MOF. This work aims to provide detailed physical insight into the interactions and kinetics of hydrogen adsorption and desorption in a select few state-of-the-art MOFs.

1.1.2 H_2 Storage

In Section 1.1.1 the hydrogen economy was motivated generally, and the following three challenges for its realization were identified: (1) mitigating the cost of hydrogen production, (2) arriving at a viable method for hydrogen storage, and (3) creating the infrastructure necessary for hydrogen delivery from production to storage to use [4]. While challenge (3) is taken as an issue of economic and governmental incentive (—which, in many states and countries, has already begun [16, 17]), challenges (1) and (2) were identified as those that may be overcome with scientific development. The preceding section addressed the challenge of mitigating hydrogen production cost by creating novel gas separation technologies based on the intelligent application of Metal Organic Frameworks. This section aims to motivate and describe the use of MOFs for hydrogen storage.

Molecular hydrogen has the highest energy content per unit mass of any fuel, however in its gaseous state it has one of the lowest energy contents per unit volume [4]. The challenge and value of hydrogen storage is then in maximizing hydrogen per volume while minimizing any additional mass and volume of the storage system. The most common metric for this characteristic of hydrogen storage systems is the percentage by weight (wt%), defined as the ratio of stored hydrogen mass to total storage system mass (that is, the sum of the mass of the stored hydrogen and the mass of the storage system absent of hydrogen). The DOE has set the long-term goal of 7.5 wt% for hydrogen storage systems that can be used in light-weight hydrogen fuel cell vehicles (passenger vehicles, forklifts, etc.) [18].

Fuel cell vehicles impose additional constraints on hydrogen storage systems. For a hydrogen storage system to be viable for use in a vehicle it must pose no greater risk to a passenger than a gasoline tank, and it must exhibit fully reversible, fast adsorption kinetics at room temperature. This former constraint rules out the straightforward option of pressurized H_2 tanks, which, at room temperature, require prohibitively high pressures in order to conform to a car's standard dimensions. The latter constraint means that whatever the storage system, hydrogen must be able to be loaded into, and removed from it on time scales comparable to gasoline in a conventional internal combustion engine. This requirement puts a constraint on the binding energy of a hydrogen molecule to the storage material: the binding energy may not be so low that filling the substrate takes significantly longer than filling up your gas tank, but it may not be so high that once the hydrogen is inside it requires high temperatures to be removed. A value for this optimal binding energy can be derived by requiring the storage system be at equilibrium under ambient conditions, as this ensures only small changes in temperature or pressure would be required to induce hydrogen uptake or its release. We describe such a state of equilibrium at constant temperature and pressure as one wherein the change in Gibbs free energy (ΔG) is zero:

$$\Delta G = \Delta H - T\Delta S = 0. \tag{1.5}$$

Here ΔH is the change in enthalpy of the system, T the system's temperature, and ΔS the system's change in entropy. According to our description of the ideal hydrogen storage system for a fuel cell vehicle, ΔH corresponds to the binding energy of hydrogen to the adsorbing substrate, where T is room temperature (298 K) and where ΔS is dominated by the entropy of hydrogen gas at standard temperature and pressure ($\sim$131 J/K·mol [19]). This straightforwardly brings us to an ideal binding energy for our storage substrate of 38.4 kJ/mol. If the constraint of operating at one atmosphere of pressure is relaxed (which can be done with minimal compromise to safety), Bhatia and Myers have shown that this ideal binding energy can be reduced to 15.1 kJ/mol at room temperature and a loading pressure of 40 atmospheres [20]. This merely constitutes the rosiest picture of hydrogen storage in MOFs however, as others have stipulated the ideal binding energy to be 22-25 kJ/mol and higher, even at elevated pressures [21].

Metal Organic Frameworks (MOFs) are a promising class of materials for hydrogen storage that have emerged only in the past two decades [10]. Due to their extremely high surface area density (often > 1000 m^2/g [10, 20, 22–24]) and physisorbtive mechanism for hydrogen adsorption, MOFs are an attractive candidate for use in fuel cell vehicles. The high surface area density of MOFs allows them to adsorb a considerable amount of H_2 per weight (> 5 wt% [10, 20, 22, 23]), while their physisorbtive properties only weakly bind H_2, allowing desorption with minimal energy expenditure. Unfortunately, to date there is no viable MOF that possesses the target wt% and binding energy set by the DOE. This thesis provides physical insight into the relative successes of current, state-of-the-art MOFs—through providing this insight we hope to aid in the informed development of novel frameworks that meet the criteria set forth by the DOE.

1.2 H_2

As described in Section 1.1.1, H_2 is the lightest isotopologue of hydrogen. As the lightest isotopologue, H_2 has the largest zero point energy when adsorbed to a surface. This aspect of H_2 figures prominently into the ZPES method of hydrogen isotopologue separation, and leads to a large zero point motion. We will elaborate upon the zero point motion of H_2 in this section and discuss the zero point motion of the other hydrogen isotopologues in the sections immediately following. We will also touch on a few emergent properties that pertain to spectroscopy of hydrogen isotopologues and their quantum dynamics.

When discussing the zero point motion of adsorbed hydrogen isotopologues, we concern ourselves with the motion of two nuclei [15]. Since, in the case of H_2, these two nuclei are protons and thus indistinguishable fermions, the wavefunction of the molecule as a whole must be antisymmetric under exchange. This means that if the spin part of the molecule's wavefunction is symmetric under exchange, the rotational part of its wavefunction must be antisymmetric, and vice versa. Since protons are spin-$1/2$ particles, the total spin state of an adsorbed H_2 molecule may be $S = 0$ or $S = 1$. These two possible spin states lead to two forms of hydrogen with slightly different quantum dynamics: para-hydrogen with nuclei in the anti-symmetric $S = 0$ spin state and symmetric rotational wavefunction (i.e. even rotational quantum number J), and ortho-hydrogen with nuclei in the symmetric $S = 1$ spin state and anti-symmetric rotational wavefunction (i.e. odd rotational quantum number J). Since ortho-hydrogen is triply degenerate and para-hydrogen is non-degenerate, and since the energy splitting between the two states is only on the order of 0.75 meV, at room temperature the ratio of ortho- to para-hydrogen is, on average, 3:1. Traditionally it is thought that this ratio remains static in the absence of spin-flipping magnetic groups, even at temperatures as low as 10 K [24,25]. Recent theoretical studies have shown ortho to para conversion may occur even in the absence of such magnetic groups however [26]. In any case, as MOFs often contain such magnetic groups, ortho to para conversion often occurs in adsorbed H_2. For several of the MOFs discussed in this work ortho to para conversion in fact occurs on time scales short enough that it is perceptible with time-varying infrared spectra.

Another pertinent feature of free H_2 is its lack of a permanent dipole moment, and the related lack of a change in dipole moment upon changes of energy. This is a feature that results from its homonuclear nature and the equal sharing of electrons between nuclei in every state of free H_2. This feature makes free H_2 infrared inactive, as to absorb a photon a molecule must change its dipole moment upon absorption. In the case of adsorbed H_2 however, weak physisorbtive Van der Waals forces distort the electron cloud of H_2, induce a dipole moment, and importantly allow for changes in dipole moment upon absorption of a photon. This makes adsorbed phase H_2 infrared active.

1.3 HD

Hydrogen deuteride, deuterium hydride, or—more simply—HD is the isotopologue of molecular hydrogen comprised of a hydrogen atom bonded to a deuterium atom. This isotopologue has a zero point energy and zero point motion between those of H_2 and D_2. Unlike either H_2 or D_2 however, HD has distinguishable nuclei. This heteronuclear property eliminates the wavefunction symmetrization requirements, and at low temperature all molecules of HD relax to the $J = 0$ state. This heteronuclear nature also results in the presence of a weak dipole moment. HD is thus theoretically infrared active even in its free state.

1.4 D_2

D_2 has the smallest zero point energy of the hydrogen isotopologues under study in this thesis (—technically tritium has a yet smaller zero point energy), and consists of two bosonic nuclei—a proton and a neutron in each. The wavefunction of the molecule as a whole must accordingly be symmetric under exchange. This means that if the spin part of the molecule's wavefunction is antisymmetric under exchange, so too must be the rotational part of its wavefunction, and vice versa. Since deuterium nuclei are spin-1 particles, the total spin state of an adsorbed D_2 molecule may be $S = 0$, $S = 1$, or $S = 2$. Since all even S spin states are symmetric, both $S = 0$ and $S = 2$ spin state deuterium possess symmetric rotational wavefunctions (i.e. even rotational quantum number J), whereas antisymmetric $S = 1$ spin state deuterium possesses an antisymmetric rotational wavefuntion (and odd quantum number J). As the m quantum number ranges from -S to S, there are 6 total states consistent with symmetric spin and rotational wavefunctions for deuterium—1 state for $S = 0$ (where $m = 0$), and 5 states for $S = 2$ corresponding to $m =$ -2, -1, 0, 1, 2. For antisymmetric spin and rotational wavefunctions there are 3 total states, corresponding to $S = 1$ and $m =$ -1, 0, 1. These degeneracy considerations lead to a ratio of 2:1, symmetric to antisymmetric deuterium at room temperature [25]. In the absence of conversion-causing groups this ratio is also remarkable static, even at temperatures as low as 10 K [25]. As with H_2, since MOFs often contain such conversion-causing groups, the conversion from symmetric to antisymmetric D_2 often occurs in adsorbed D_2. For several of the MOFs discussed in this work this conversion occurs on time scales on the order of seconds to minutes.

Just as with H_2, another pertinent feature of D_2 is its lack of a permanent dipole moment. This feature makes free D_2 infrared inactive, but, as with H_2, adsorbed phase D_2 is infrared active (though in general less infrared active than H_2).

1.5 Metal Organic Frameworks Under Consideration

As stated previously, Metal Organic Frameworks (MOFs) are porous crystalline structures with extremely large surface area densities. MOFs are comprised of metal-oxide clusters connected by organic ligands [10], and are particularly valuable due to their "chemical tunability"—MOFs can be synthesized in a variety of structures with differing adsorption characteristics, surface area densities, and porosities by connecting different metal-oxide clusters with different organic ligands in a building-block fashion [10]. In the following sections we give a brief overview of the MOFs under consideration in this thesis. These MOFs are Co-MOF-74 (dobdc), Co-MOF-74 (*m*-dobdc), and VSB-5—three of the top-performing MOFs synthesized to date in terms of binding energy and surface area density.

All of the following MOFs possess coordinatively unsaturated 'open-metal' adsorption sites. After initial synthesis, the metal atoms in the MOFs are bonded to the structure of the MOF as well as so-called 'guest' molecules. After activation—the process of heating the MOF for an extended period of time (between ∼4-12 hours) under vacuum—these guest molecules are removed, and the metal atoms are left coordinatively unsaturated. This creates an adsorption site with a strong binding energy (∼10 kJ/mol as opposed to ∼5 kJ/mol in MOFs without coordinatively unsaturated open-metal sites) [22]. As they lead to stronger binding energies, we are particularly interested in probing the adsorption and desorption properties of these sites.

1.5.1 Co-MOF-74 (dobdc)

Some of the most well-documented and highest performing MOFs in terms of binding energy are the members of the isostructural M-MOF-74 series, where M is a stand-in for one of six metals—either manganese (Mn), iron (Fe), cobalt (Co), nickel (Ni), copper (Cu), or zinc (Zn). First synthesized by Rosi, et al. in 2005 [27], the M-MOF-74 series has been given alternate names M_2(dhtp), M/DOBDC, and M-CPO-27. The M-MOF-74 series is ideal for investigation of the interaction between H_2 and metals due to the ability to exchange metal species and isolate the variable of metal choice. However, in this work we limit our investigation to Co-MOF-74. More specifically, we limit our investigation to Co-MOF-74 (dobdc) and Co-MOF-74 (*m*-dobdc), where (dobdc) denotes the organic ligand 2,5-dioxido-1,4-benzenedicarboxylate and where (*m*-dobdc) denotes an isomer of this ligand, 4,6-dioxido-

1,3-benzenedicarboxylate. This section aims only to outline the basic structure of Co-MOF-74 (dobdc). Section 3.1 provides information on its desorption properties.

Co-MOF-74 (dobdc) has chemical formula:

$$\mathrm{Co_2(C_8H_2O_6)}, \tag{1.6}$$

and molar mass ~ 312 g/mol. Co-MOF-74 (dobdc) has BET surface area 1056 $\mathrm{m^2/g}$ [23] and isosteric heat of adsorption 10.8 kJ/mol [28]. Powder X-ray and neutron diffraction experiments reveal Co-MOF-74 (dobdc) to have space group $R\bar{3}$ with hexagonally symmetric pores, as shown in Figure 1.4 [22, 28]. Both diffraction techniques show Co-MOF-74 (dobdc) to have at least four binding sites, each with hexagonal symmetry. The primary, strongest-binding site (site 1 in Figure 1.4) arises from the coordinatively unsaturated open metal [22]. The benzene-like linker in Co-MOF-74 (dobdc) has been theorized to contribute to the hydrogen adsorption in site 3, as labeled in Figure 1.4 [29].

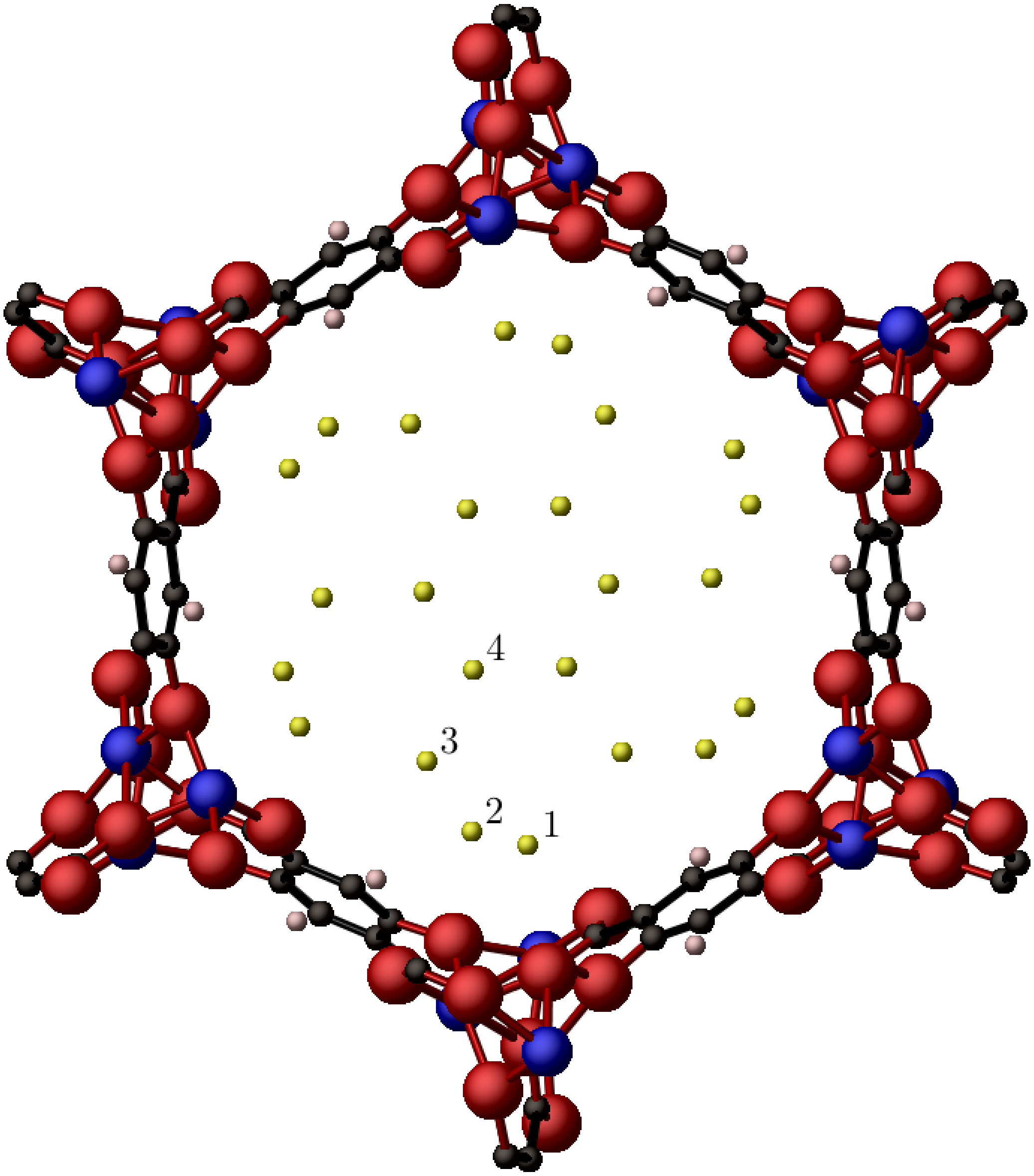

Figure 1.4: Crystal structure of a single pore of metal-organic framework Co-MOF-74 (dobdc), as determined through powder X-ray and neutron diffraction [22, 28]. Red spheres represent oxygen atoms, blue spheres represent cobalt atoms, black spheres represent carbon atoms, light pink spheres represent hydrogen atoms, and yellow spheres represent adsorbed H_2 molecules in the four labeled adsorption sites (adsorption sites labeled in order of binding energy magnitude).

1.5.2 Co-MOF-74 (*m*-dobdc)

Co-MOF-74 (*m*-dobdc) is another top-performing MOF in the M-MOF-74 series. Synthesized in 2014, the structure of Co-MOF-74 (*m*-dobdc) is outlined in this section, while its desorption properties are investigated in Section 3.2.

Co-MOF-74 (*m*-dobdc) differs from Co-MOF-74 (dobdc) only in the structure of its organic ligand. As shown in Figure 1.5, the organic ligand (*m*-dobdc) is an isomer of (dobdc). Accordingly, Co-MOF-74 (*m*-dobdc) has the same chemical formula (formula (1.6)) and molar mass as Co-MOF-74 (dobdc). This change, though in some ways minute, has been shown to have a substantive effect. Co-MOF-74 (*m*-dobdc) has a reported isosteric heat of adsorption of 11.5 kJ/mol and BET surface area of 1264 m^2/g [28], both of which are larger than in Co-MOF-74 (dobdc). X-ray and neutron diffraction experiments have also been performed on Co-MOF-74 (*m*-dobdc), and reveal it to have space group $R3m$ and structure shown in Figure 1.6 [28]. Again diffraction techniques reveal at least four binding sites.

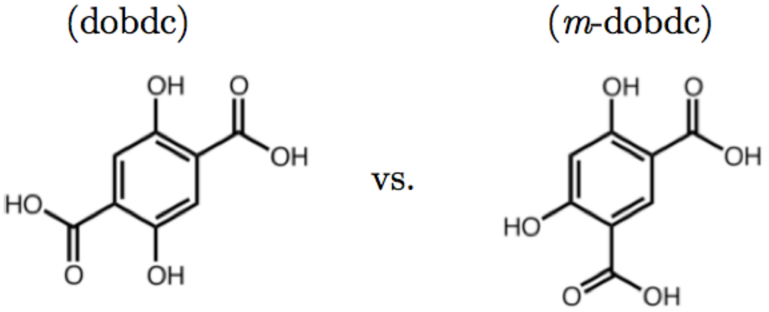

Figure 1.5: Comparison of organic ligand isomers (dobdc) and (*m*-dobdc).

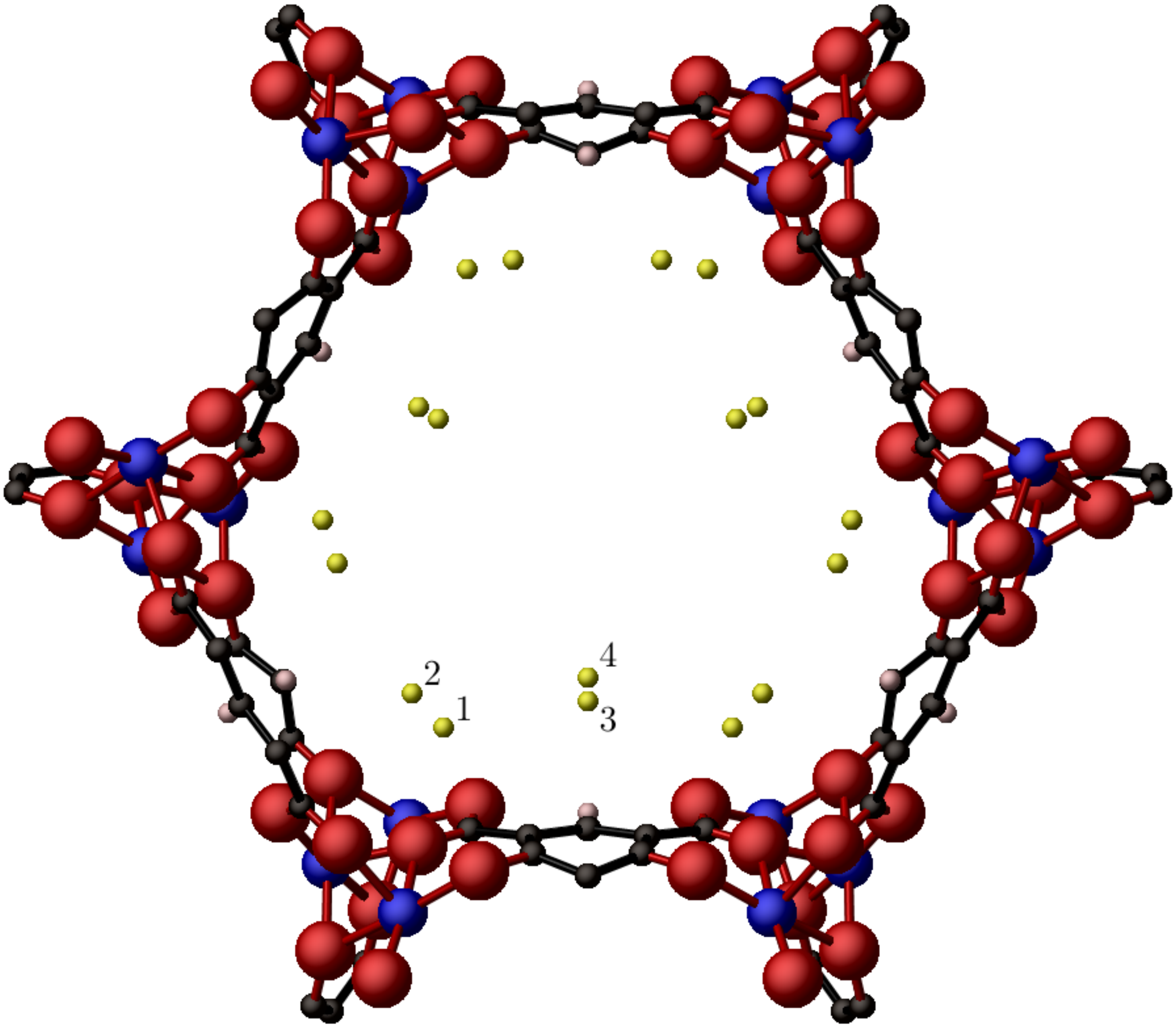

Figure 1.6: Crystal structure of a single pore of metal-organic framework Co-MOF-74 (*m*-dobdc), as determined through powder X-ray and neutron diffraction [28]. Red spheres represent oxygen atoms, blue spheres represent cobalt atoms, black spheres represent carbon atoms, light pink spheres represent hydrogen atoms, and yellow spheres represent adsorbed H_2 molecules in the four labeled adsorption sites (adsorption sites labeled in order of binding energy magnitude).

1.5.3 VSB-5

From the perspective of hydrogen storage and gas separation, the primary insufficiency of all MOFs to date has been in binding energy. By studying the successes of one of the top-performing frameworks in this department, we hope to inform what properties in general lead to increased binding energy. This is the approach we undertake in this work as we study the framework VSB-5. This section provides a brief overview of the structure and properties of VSB-5, while Section 3.3 provides information on its desorption properties, which have been discovered through application of infrared spectroscopy and a novel form of thermal-desorption spectroscopy.

Nickel (II) Phosphate VSB-5 (Versailles-Santa-Barbara-5) is a framework with nickel metal clusters and chemical formula:

$$\mathrm{Ni_{20}[(OH)_{12}(H_2O)_6][(HPO_4)_8(PO_4)_4] \cdot 12H_2O}. \tag{1.7}$$

VSB-5 has a Brunauer-Emmet-Teller (BET) surface area of 500 ± 10 m^2/g, reportedly the largest to date for open-framework metal phosphate materials [30]. X-ray powder diffraction reveals VSB-5 to have a pore diameter of 12.8 Å, centro-symmetric space group $P6_3/m$, and crystallographic structure and atomic coordinates which lead to the single pore structure shown in Figure 1.7. (Figure 1.7 was created in the program CrystalMaker with atomic coordinates given by Ref. [31].) As calculated from chemical formula (1.7), VSB-5 has a molar mass of $\sim$2850 g/mol. VSB-5 has been shown to possess coordinatively unsaturated Ni^{2+} sites, which contribute to its strong physisorption of H_2 in at least three distinct sites within a pore [30, 31]. These three sites are labeled in Figure 1.7; within a single pore, each site has hexagonal symmetry about the pore axis.

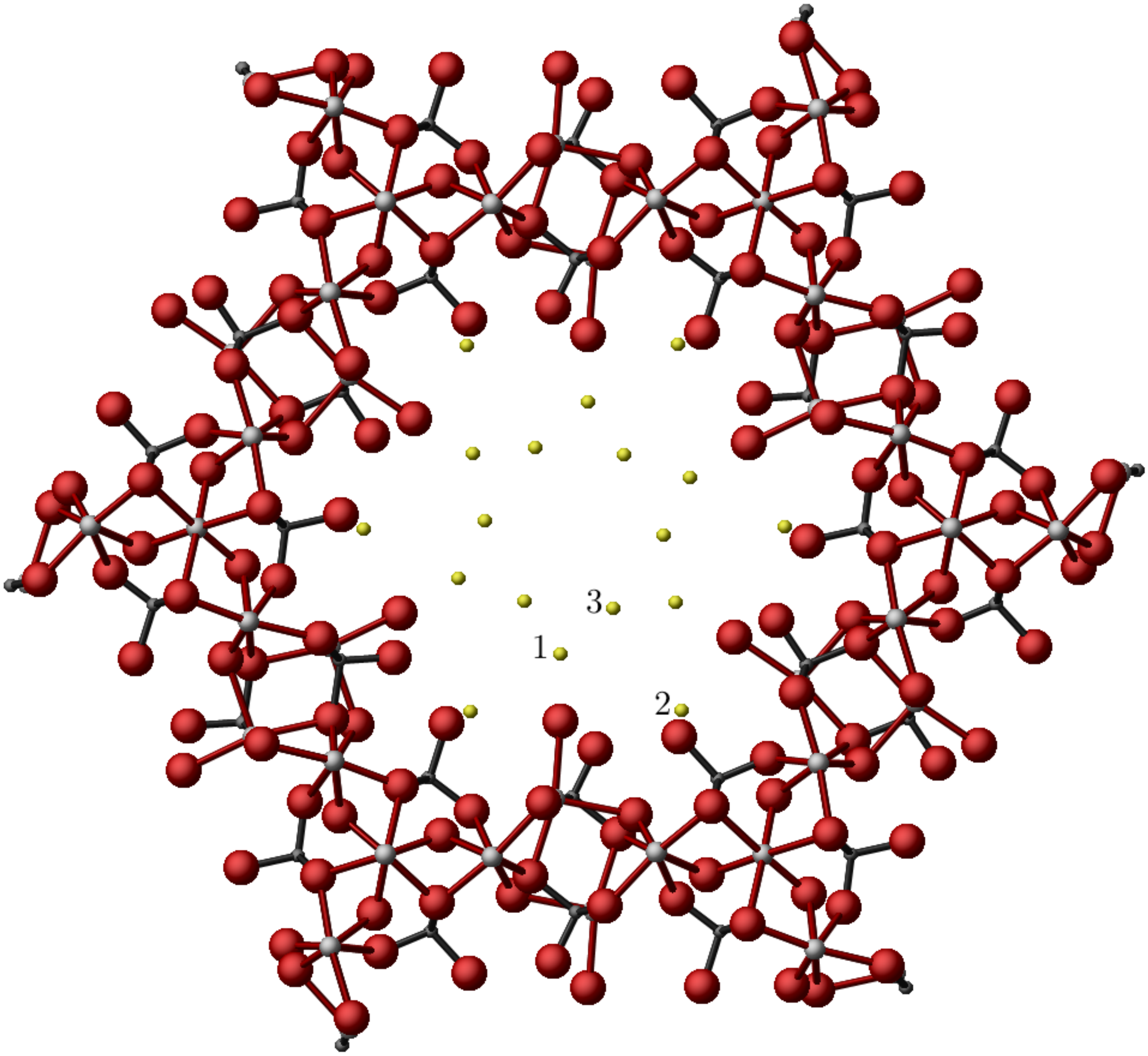

Figure 1.7: Crystal structure of a single pore of zeolitic framework VSB-5, as determined through X-ray powder diffraction [30]. Red spheres represent oxygen atoms, light gray spheres represent nickel atoms, dark gray spheres represent phosphorous atoms, and yellow spheres represent adsorbed H_2 molecules in the three labeled adsorption sites (adsorption sites labeled in order of binding energy magnitude).

1.6 Infrared Spectroscopy

One major technique used in this work is infrared spectroscopy—more specifically, Fourier Transform Infrared Spectroscopy (FTIR) dependent on the use of a Michelson interferometer. As there is an abundance of literature available on FTIR and Michelson interferometry generally [32–35], we will only touch upon those physical mechanisms involved in FTIR and instead direct most of our efforts toward elucidating the quantum mechanics of motion for infrared transitions of hydrogen isotopologues adsorbed in MOFs.

To be infrared active, a transition of a molecule from one energy state to another must result in a change in molecular dipole moment [15]. As alluded to in Sections 1.2 and 1.4, since molecular hydrogen and deuterium are homonuclear and share electrons equally between nuclei, every transition hydrogen or deuterium makes—vibrational, rotational, translational, or any combination of the three—does not result in a change of electric dipole moment (and, since magnetic effects in these systems are generally much smaller than electric effects, we only concern ourselves with changes in electric dipole moment). This makes free hydrogen and deuterium infrared inactive. However, when adsorbed into a MOF, the electron cloud of these molecules can be distorted in such a way that a dipole moment is induced. This makes adsorbed phase hydrogen and deuterium infrared active. This is one of two mechanisms by which hydrogen and deuterium are made infrared active, and is usually referred to as the 'overlap mechanism.' In the general case, infrared molecular transitions are characterized by the quantum mechanical transition moment

$$\vec{\mu}^e_{nm} = \langle n|\vec{\boldsymbol{\mu}}^{\boldsymbol{e}}|m\rangle, \tag{1.8}$$

where $|n\rangle$ and $|m\rangle$ are two molecular states with energies E_n and E_m, respectively, and where $\vec{\boldsymbol{\mu}}^{\boldsymbol{e}}$ is the electric dipole moment operator, defined as:

$$\vec{\boldsymbol{\mu}}^{\boldsymbol{e}} = \sum_i q_i \vec{d}_i. \tag{1.9}$$

Here q_i is a charge and $\vec{d}_i$ is its accompanying displacement vector, usually taken with respect to the molecule's center of mass. The energy of such a transition must be

$$\Delta E_{\text{transition}} = E_n - E_m = \hbar\omega_0 \tag{1.10}$$

where we have suggestively written this energy as $\hbar$ (the reduced Planck constant) multiplied by some angular frequency ω_0, and where we have made the implicit assumption $E_n > E_m$. In infrared spectroscopy, when we concern ourselves with infrared transitions we are concerned with transitions that can be mediated by photons. As a result of their changing electric field, these mediating photons can be modeled as causing a time-dependent perturbation to the Hamiltonian of the system (in our case, the MOF–adsorbed-species system). As derived in Ref. [15], first-order time-dependent perturbation theory applied to such a perturbation leads to the following proportionality describing the probability of a transition from state $|m\rangle$ to state $|n\rangle$:

$$P_{nm} \propto \frac{|\vec{\mu}^{e}_{nm}|^2}{(\omega_0 - \omega)^2 + \gamma^2}. \tag{1.11}$$

Here ω is the angular frequency of the mediating photon, and γ is a damping term arising from lifetime broadening described below. This relationship describes a Lorentzian distribution of transition probability centered about ω_0. Thus a photon with angular frequency ω_0 has the highest likelihood of causing a transition of the molecule from $|m\rangle$ to $|n\rangle$ (as we might have expected), while photons with other frequencies cause this transition with probability given by proportionality (1.11).

In the case of infrared spectroscopy of hydrogen isotopologues adsorbed in MOFs, and in the case of almost all physical applications, this Lorentzian distribution is smeared out due to physical imperfections and lifetime broadening. In our case these imperfections correspond to inhomogeneities in the crystal lattice of the MOF and the occasional presence of adsorbed impurities. Assuming a Gaussian distribution of inhomogeneities and impurities, this can be thought of as producing a Gaussian distribution of Lorentzian peaks (or, otherwise, a smearing out of the Lorentzian distribution). The quantum mechanical effect of lifetime broadening also contributes to the size of these peaks; this effect is a result of the energy-time uncertainty principle

$$\Delta E \Delta t \geq \frac{\hbar}{2}, \tag{1.12}$$

applied to translational transitions, where ΔE is the uncertainty in the energy of the transition (which is related to the broadness of the associated peak), and where Δt is the average time it takes an excited adsorbed molecule to relax to the ground state [15]. As lattice-phonon–adsorbate-translation coupling decreases the time it takes for the adsorbate to relax to its ground state (Δt), ΔE increases and translational peaks tend to broaden.

As shown in the Honors Thesis of Christie Simmons [36], the overlap mechanism results in the quantum number selection rules $\Delta J = 0$ and $\Delta m = 0$. The existing nomenclature denotes transitions of this sort Q transitions. These transitions are followed by a number in parenthesis corresponding to the J state; that is, Q(0) denotes the Q transition for para-hydrogen, whereas Q(1) denotes the Q transition for ortho-hydrogen.

A second mechanism for infrared transitions applicable to this work is what has been deemed the 'quadrupole mechanism.' In this case, infrared photons interact not only with the adsorbed molecules, but also with the adsorbate host. If an adsorbed molecule induces a dipole on its host through host–molecule quadrupole interactions, the infrared photon can interact with the dipole moment on the host but affect the dynamics of the adsorbed molecule. Again then the energy of such a transition is given by the difference in energy of excited and non-excited adsorbed molecular state (Equation (1.10)), and the probability of a transition with respect to photon frequency is given by the Lorentzian proportionality (1.11). We bring up this mechanism because molecular hydrogen possesses a permanent quadrupole moment (as can be intuited from a classical picture of its charge geometry) and induces dipoles on MOF sites just as described above. The selection rules for these transitions have been carefully determined in the Honors Theses of Christie Simmons [36] and Hugh Churchill [37]. These selection rules are $\Delta J = 0, \pm 2$ and $\Delta m = 0, \pm 1, \pm 2$. Transitions with $\Delta J = 0$ add to the Q transitions of the overlap mechanism, whereas transitions with $\Delta J = +2$ are referred to as S transitions. These transitions are also generally followed by a number in parenthesis, in this case denoting the initial J state of the molecule; S(0) refers to the transition from $J = 0$ to $J = 2$, and S(1) refers to the transition from $J = 1$ to $J = 3$. Transitions with $\Delta J = -2$ occur with vanishingly small probability, as we take our infrared spectra at cryogenic temperatures wherein adsorbed molecules are already in their ground state and thus cannot make transitions to lower J states (indeed no such states exist, as described in Section 1.1.1 with regard to the concept of a zero point energy!).

Given the geometry of molecular hydrogen isotopologues, each molecule has six spatial modes of motion: one mode describing the internuclear separation (ρ), two angular modes (θ, ϕ) describing the angular orientation of the molecule, and three positional, or translational, modes describing the center of mass of the molecule, usually denoted as (x, y, z). These coordinates are depicted in Figure 1.8. Grouping these degrees of freedom as we have,

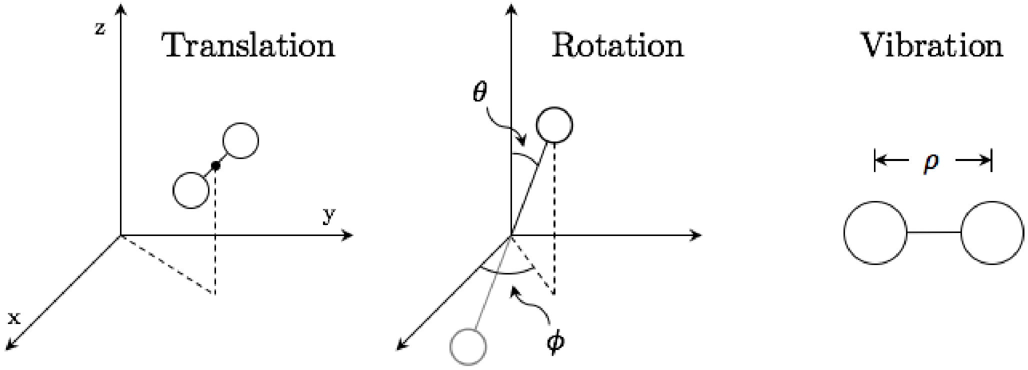

Figure 1.8: Degrees of freedom of hydrogen isotopologues, adapted from Ref. [37].

we see there are three main modes of motion available to confined hydrogen isotopologues: vibrational, rotational, and translational. In the following sections we address each of these modes of motion and the corresponding infrared transitions.

1.6.1 Vibrations

Every transition represented by the infrared spectra in this work involves a vibrational transition. The energy of the fundamental transition from vibrational quantum number $v = 0$ to $v = 1$ for H_2 is $\Delta E_v \approx \frac{1}{2}$ eV. Comparing this to the familiar thermal energy of a molecule at room temperature of $k_B T_{\text{room}} \approx \frac{1}{40}$ eV (where k_B is Boltzmann's constant and T_{room} room temperature), we see that the probability of an H_2 molecule occupying the first vibrationally excited state even at room temperature is exceedingly small. Quantitatively, since thermal population goes as $e^{\Delta E/k_B T}$, the probability of such an excited state occurring at room temperature is $\sim e^{-20}$. At cryogenic temperatures this probability is further reduced, so to an exceedingly good approximation we consider all adsorbed isotopologues to be in the $v = 0$ state. Transitions with $\Delta v = +1$ occur with the largest probability, however $\Delta v = +2$ transitions—named overtone transitions—do occur with large enough probability that they are often apparent in our infrared spectra.

Highly accurate *ab initio* values for the internuclear H_2 potential have been tabulated in the literature [38]. This internuclear interaction potential does not possess an analytic, closed form, though many approximations to it have been proposed. One notable approximation to the *ab initio* potential, the Morse potential, is shown in Figure 1.9. In all of these approxi-

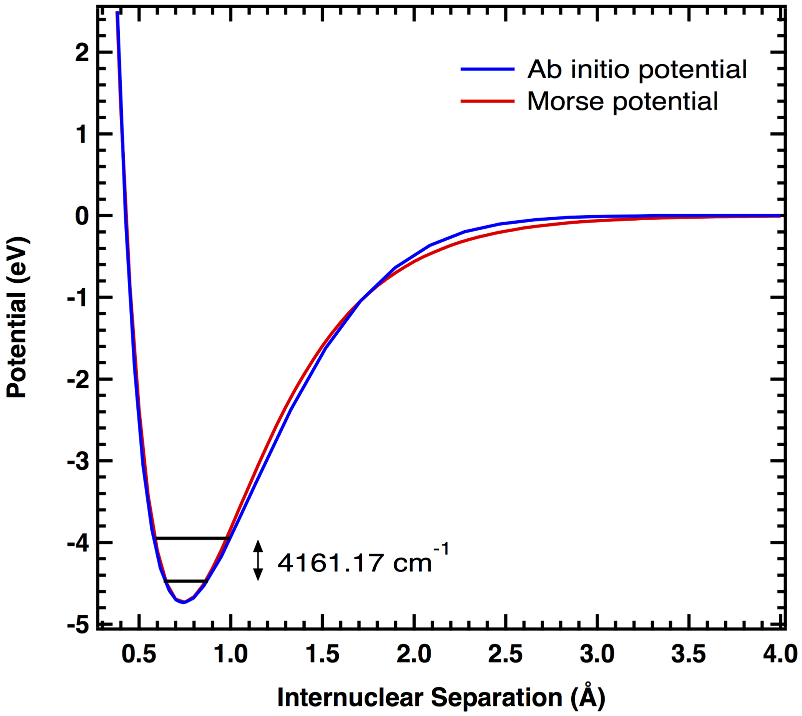

Figure 1.9: *Ab Initio* and Morse potentials for H_2 as a function of internuclear separation, courtesy of Ref. [37].

mations, and indeed in the *ab initio* case, for small oscillations about $\rho = \rho_0$ (where ρ_0 is the equilibrium separation between H atoms) the potential can be approximated as quadratic. Such small oscillations correspond to low lying v states. In this quadratic approximation we follow the usual prescription and model the potential as arising from an internuclear spring with spring constant k_{vib}. Applying Hooke's potential ($V(x) = {}^1\!/\!{}_2 k_{\text{vib}}(\rho - \rho_0)^2$) to the time-independent Schrödinger equation, we arrive at the approximate quantum mechanical energies for H_2 vibrational states of

$$E_{\text{vib}} \approx \left(v + \frac{1}{2}\right) hc\nu_0, \tag{1.13}$$

where h is Planck's constant, c the speed of light, and ν_0 the spatial frequency of the fundamental vibrational transition in H_2, 4161.17 cm^{-1} [36]. This spatial frequency takes the usual form for a spring system:

$$\nu_0 = \frac{\omega_0}{2\pi c} = \frac{1}{2\pi c}\sqrt{\frac{k_{\mathrm{vib}}}{\mu_{\mathrm{H}_2}}}, \tag{1.14}$$

where ω_0 is the angular frequency of the fundamental transition and μ_{H_2} is the reduced mass of H_2.

When adsorbed into a MOF, this fundamental frequency decreases in proportion to the interaction of H_2 and MOF site. Weakly adsorbing sites produce infrared spectral peaks slightly redshifted from 4161.17 cm^{-1} (by $\sim$50 cm^{-1}), while strongly adsorbing sites produce infrared spectral peaks significantly redshifted (by $\sim$100 cm^{-1}) from the fundamental vibrational transition in free H_2 [39].

For other hydrogen isotopologues the spatial frequency of the fundamental vibrational transition is reduced by a factor of $\sqrt{\mu_{\mathrm{XX}}/\mu_{\mathrm{H}_2}}$ in accordance with Equation (1.14), where XX stands for either HD or D_2.

1.6.2 Rotations

Our treatment of the rotational transitions of hydrogen isotopologues adsorbed into MOFs rely on the assumption that these isotopologues act as rigid rotors. A more complete treatment based on the ‘hindered rotor’ model has been performed on hydrogen adsorbed into Zn-MOF-74, wherein a hydrogen molecule is not allowed to rotate freely but instead has a higher or lower potential depending on its orientation [40]. This treatment follows the same approximate prescription and serves more as a correction rather than an alternative to the approach outlined below.

In the rigid rotor approximation we consider the classical energy of a system of two masses connected by a massless rod of length ρ (the internuclear separation), and recast this picture into the quantum mechanical regime. Classically, the energy of such a system is $E = L^2/2I$, where L is the angular momentum of the system and $I = 2m_p(\rho/2)^2 = m_{\mathrm{H}_2}(\rho/2)^2$ its moment of inertia (where m_{H_2} is the mass of a H_2 molecule, twice the mass of a proton m_p). In the quantum mechanical regime L is quantized in terms of $\hbar$ and the rotational quantum number J, as

$$L^2 = \hbar^2 J(J+1), \tag{1.15}$$

and I is recast as

$$I = \frac{1}{4} m_{\mathrm{H}_2} \langle \rho^2 \rangle. \tag{1.16}$$

The quantized energies of this system are now written as

$$E_{\mathrm{rot}} = \frac{2\hbar^2 J(J+1)}{m_{\mathrm{H}_2} \langle \rho^2 \rangle} = hcB_v J(J+1), \tag{1.17}$$

where B_v is a rotational constant that depends on the vibrational state of the molecule (v). For the first two vibrational states of molecular hydrogen, $B_0 = 59.3\ \mathrm{cm}^{-1}$ and $B_1 = 56.4\ \mathrm{cm}^{-1}$ [41].

As Equation (1.17) is proportional to the reciprocal of the reduced mass of the rigid rotor, the rotational constants and rotational energies of isotopologues HD and D_2 are scaled by $1/\sqrt{1.33}$ and $1/\sqrt{2}$, respectively.

As mentioned previously, in the infrared spectra presented in this work every spectral peak involves a vibrational transition, almost exclusively from vibrational state $v = 0$ to $v = 1$. Rotational transitions occur in addition to these vibrational transitions at incident photon energies distributed around $E_{\mathrm{photon}} = E_{\mathrm{vib}} + E_{\mathrm{rot}}$.

1.6.3 Translations

The final mode of motion for hydrogen isotopologues adsorbed into MOFs is the translation of the isotopologue center of mass. While potentially the easiest to envision, the quantized translational motion of hydrogen molecules as a whole is notoriously difficult to model. The Honors thesis of Kinori Rosnow is dedicated to modeling the potential energy landscapes of certain paradigmatic MOFs with isotropic primary binding sites [42]; these potential energy landscapes are necessary for a physically robust treatment of the quantized translational motion of adsorbed molecules, however such a treatment is beyond the scope of this work. It will suffice for our purposes to consider small oscillations about the local minima of these isotropic MOF binding sites, and model these oscillations as occurring in a three-dimensional simple harmonic oscillator potential. This potential takes the form $V(r) = {}^1\!/_2 k_{\mathrm{trans}} r^2$ where r is the distance of the molecule's center of mass from the location of the minimum of the potential. In terms of Cartesian coordinates (x, y, z), $r = \sqrt{x^2 + y^2 + z^2}$, where we have made the implicit assumption that $x = y = z = 0$ occurs at the location of the minimum of the potential well. Taking the same approach as in our discussion of vibrations, we now apply the three-dimensional simple harmonic oscillator potential to the time-independent Schrödinger equation and arrive at the approximate translational energies of

$$E_{\mathrm{trans}} \approx \left(n + \frac{3}{2}\right)\hbar\omega. \tag{1.18}$$

Here n is the translational quantum number, and ω is the quantum mechanical angular translation frequency.

Since the angular translational frequency ω is proportional to the inverse square root of the total mass of the molecule (e.g. $1/\sqrt{m_{\mathrm{H}_2}}$), the translational energies of isotopologues HD and D_2 are scaled by factors of $1/\sqrt{1.5}$ and $1/\sqrt{2}$, respectively, from the H_2 energies.

The spectroscopic data presented in this work suggest that the spacing $\omega/2\pi c$ between translational levels of adsorbed hydrogen isotopologues is on the order of 100 cm^{-1}. As with rotational transitions, translational transitions are represented in our infrared spectra by spectral peaks around incident photon energies of $E_{\mathrm{photon}} = E_{\mathrm{vib}} + E_{\mathrm{trans}}$.

Translational spectral peaks are usually identifiable by their slight blueshift from the fundamental vibrational transition (shifts of $\sim$100 cm^{-1}, as stated) and by their broadness. It is thought that translational peaks are much broader than either rotational or vibrational peaks because impurities and inhomogeneities in the crystal lattice of a MOF cause the potential energy landscape to vary significantly from site to site and from pore to pore.

1.7 Thermal-Desorption Spectroscopy (TDS)

The second major technique used in this work is Thermal-Desorption Spectroscopy (TDS). Alternatively named Temperature-Programmed Desorption (TPD), TDS was originally a technique created and employed to understand surface desorption kinetics. In the past two decades however, body of research has emerged applying TDS to probe the desorption kinetics of molecules adsorbed into MOFs and other substrates [11–13, 43–47].

The procedure for TDS experiments is simple: adsorb a species into/onto a substrate at a sufficiently low temperature, then heat the substrate at a constant rate and record the desorption rate of the species as a function of temperature. For surfaces, this desorption follows an Arrhenius expression called the Polanyi-Wigner equation:

$$r(T) = -\frac{d\theta}{dt} = \nu\ \theta^{n}\ e^{-E_{\mathrm{b}}/k_{\mathrm{B}}T}, \tag{1.19}$$

where r is the desorption rate of the species from the substrate, θ the fractional surface coverage of the species, t the time, ν the aptly named ‘pre-exponential factor’ of desorption with units of frequency, n the order of desorption, E_b the ‘activation’ or binding energy of the species to the substrate, k_B Boltzmann’s constant, and T the temperature of the system. T and t are related by the constant heating rate $\beta = dT/dt$. In its most general form, the Polanyi-Wigner equation above expresses ν and E_b as functions of coverage (θ) and temperature, however here we concern ourselves only with the coverage-independent form of the equation.

To elucidate the dependence of differential Equation (1.19) on the parameters ν, E_b, β, and θ_0, the initial fractional coverage, in Figure 1.10 we present numerical solutions to the first-order, coverage-independent Polanyi-Wigner equation evaluated at systematically differing parameter values. By coverage-independent we mean that ν and E_b are taken to be constant with respect to coverage, time, and temperature. We use the program Mathematica to generate these solutions, employing the Runge-Kutta method with the following procedure: We define the temperature function $T(t) = \beta t + T_0$ for $t \geq 0$ and $T_0 \approx 0$ K (—for computational reasons T_0 may not be exactly 0; exactly, we use $T_0 = 0.001$ K), and a function for the number of desorbed molecules

$$n(t) = n_0 - \theta \; n_\mathrm{max}, \tag{1.20}$$

which is derived from the equation for fractional surface coverage:

$$\theta = \frac{n_0 - n(t)}{n_\mathrm{max}}. \tag{1.21}$$

Here n_0 is the total number of molecules initially adsorbed onto the surface and n_max is the maximum number of molecules that can be adsorbed onto the surface. At some initial surface coverage $\theta_0 = n_0/n_\mathrm{max}$ then, we take $n(t) = 0$. This model assumes that there is only one type of adsorption site, with a uniform, coverage independent binding energy E_b for each site. We further assume that the pre-exponential factor ν is coverage independent, leading us to the differential equation:

$$\frac{d\theta(t)}{dt} \;=\; -\;\nu\;\theta(t)\;e^{-E_\mathrm{b}/(k_\mathrm{B}(\beta t + T_0))}. \tag{1.22}$$

Figure 1.10 shows the numerical solutions to Equation (1.22) with the arithmetical modification given by Equation (1.20). These solutions are single peaks that broaden and shift to higher temperature with increases in heating rate β and binding energy E_b, and with decreases in pre-exponential factor ν. Decreases in initial surface coverage θ_0 simply result in smaller peaks of identical shape; as shown in the inset of Figure 1.10(b), if all of these peaks are divided by their respective θ_0 values, the result is five identical overlaid peaks. The area under the peaks in Figure 1.10 are all proportional to the total number of molecules originally loaded into the system, n_0, except in the case of Figures 1.10(c) wherein the area of each solution has been scaled by β for clarity. Mediate initial values were chosen for relevant parameters. These simulations are in agreement with those performed by Jong and Niemantsverdriet [48], and with the experimental data for H_2 desorption from surface Ag(111) [49].

In this work we present data acquired with a novel form of TDS. To the best of the author's knowledge, in the case of all reported surface TDS and TDS of species adsorbed into MOFs, a mass spectrometer, gas chromatograph, or other apparatus is used that evacuates molecules in the gas phase that have desorbed from the substrate. In this work we present reproducible, physically informative TD spectra acquired with a pressure gauge. As mass spectrometers—the most common apparatus for performing TDS—cost in excess of 75,000 USD [50], the acquisition of TD spectra that are in agreement with the literature while using only a pressure gauge is an important development.

The TD spectra presented in this thesis provide a proof of concept for this novel TDS technique, but this work serves as more than a proof of concept. In the following chapters we present TD spectra of Co-MOF-74 (dobdc), Co-MOF-74 (*m*-dobdc), and VSB-5. While our TD spectra for Co-MOF-74 (dobdc) and VSB-5 are importantly in good agreement with those reported in the literature using more costly and less simple equipment, we also report the TD spectra of Co-MOF-74 (*m*-dobdc), which has yet to be presented in the literature. Our custom apparatus further allows us to analyze the adsorption and desorption behavior of these MOFs as a function of adsorbed hydrogen concentration. As opposed to other techniques presented in the literature, we can extract site-specific adsorption information by loading specific amounts of hydrogen into a MOF. We also corroborate our TD spectra with *in situ* IR spectroscopy, an approach not taken in the literature. Further still, we report on several forms of analysis for TDS of hydrogen isotopologues adsorbed into MOFs generally. In Section 3.1 and 3.4 we conclude that the desorption kinetics of hydrogen isotopologues from MOFs do not follow the coverage-independent Polanyi-Wigner equation, a result we

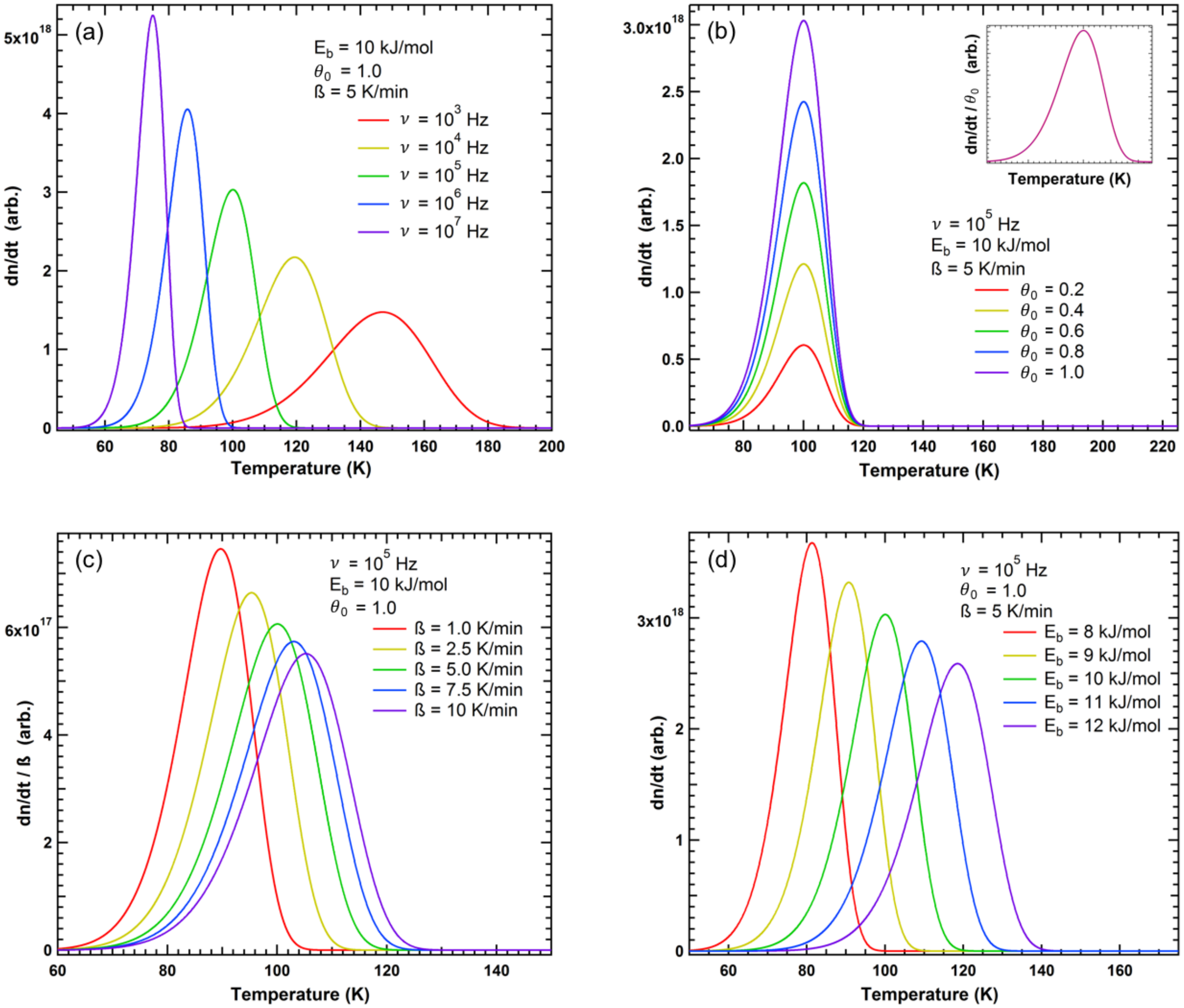

Figure 1.10: Runge-Kutta numerical solutions to the Polanyi-Wigner equation for systematically varying (a) pre-exponential factor ν, (b) initial surface coverage θ_0, (c) heating rate β, and (d) binding energy E_b. Numerical solutions in (b) and (c) are scaled by θ_0 and β, respectively.

attribute to a fundamental difference between 2D and 3D surfaces. The preceding exposition of first-order, coverage-independent Arrhenian desorption serves as a reference with which we will compare the desorption kinetics of hydrogen from MOFs.

The most pertinent concern about our TDS approach is with regard to readsorption. In the evacuation techniques, once an adsorbed molecule desorbs and makes it to the gas phase there is a vanishingly small probability that it will readsorb. The concern is that with the novel technique presented readsorption will almost certainly occur, and this readsorption will alter the nature of the desorption spectra in such a way as to make them meaningless. This concern can be assuaged with three considerations: (1) our desorption spectra for VSB-5 and Co-MOF-74 (dobdc) are in agreement with those presented in the literature using evacuation techniques, (2) the probability of readsorption is minimized with our use of small sample masses (< 10 mg) relative to the amount of hydrogen adsorbed, and (3) while we in fact see indicators of readsorption, the shifts in peak location and shape produced by this effect are small (< 10 K shift of the temperature at peak maximum). See Sections 3.1 and 3.2 for more on consideration (3).

Chapter 2: Experimental Apparatus and Procedure

In this chapter we provide some detail on the experimental apparatus and procedure used to acquire the spectroscopic results presented this thesis. The custom apparatus, which is the result of many years of design, manufacturing, and modification, allows for Fourier Transform Infrared Spectroscopy (FTIR) of hydrogen isotopologues adsorbed into MOFs at liquid helium temperatures. Notably, the apparatus simultaneously allows for Thermal-Desorption Spectroscopy (TDS). The FTIR setup consists primarily of a modified Bomem DA3 Michelson interferometer, equipped with broadband quartz-halogen and silicon-carbide globar infrared sources, a calcium fluoride (CaF_2) beamsplitter, Spectra-Tech Diffuse Reflectance Infrared Fourier Transform Spectroscopy (DRIFTS) optics, and a Mercury-Cadmium-Telluride (MCT) detector. More information on the FTIR spectroscopic equipment can be found in Ref. [51].

TDS is facilitated by a modified, liquid helium Janis ST-300T closed cycle cryostat, which achieves temperatures of the MOF sample as low as 15 K. This temperature is measured by two DT-670 four-probe silicon diode temperature sensors, and is controlled by a Lakeshore Model 331 temperature controller. A mass of a MOF is dosed with hydrogen gases by a Micromeritics ASAP (Accelerated Surface Area and Porosimetry System) 2020 physisorption analyzer. The system temperature is increased steadily by means of a small heating element inside the cryostat, and the pressure of the system during desorption is measured using the ASAP device.

2.1 Diffuse Reflectance Infrared Fourier Transform Spectroscopy (DRIFTS) Apparatus

Hydrogen isotopologues in the adsorbed phase are generally very weakly infrared active. In order to detect absorption of infrared photons by adsorbed hydrogen, a large optical path length through the adsorbent is required. Unfortunately, in the case of MOFs, the adsorbent has a high infrared scattering cross-section—this means that after large optical path lengths through a sample an infrared beam will become diffuse and difficult to measure. Thus there are two competing complications involved in taking infrared spectra of adsorbed phase hydrogen in MOFs: the weak infrared activity of adsorbed hydrogen, which necessitates a long optical path length, and the large scattering cross-section of MOFs, which necessitates a short path length. These competing complications make the most straightforward transmission spectroscopy setup—wherein an infrared beam is sent straight through a MOF and the infrared absorbance is detected—very difficult. Instead, the approach of Diffuse Reflectance Infrared Fourier Transform Spectroscopy (DRIFTS) is employed.

A schematic of the DRIFTS optics used in this work is shown in Figure 2.1. In this scheme, infrared radiation is directed onto a MOF sample by plane and ellipsoidal mirrors. Due to the scattering cross-section of the sample and the non-uniformity in grain shape and size, the incident infrared photons undergo multiple scattering events within the sample before either being absorbed or reflecting out of the sample at an oblique angle. This reflected radiation is collected by another set of ellipsoidal and plane mirrors, and is directed to a liquid nitrogen cooled Mercury-Cadmium-Telluride (MCT) detector. The MOF sample and copper sample holder are kept in a sapphire-windowed steel dome, which is screwed to a copper sample mount. Indium wire is placed between the dome and copper mount to ensure a low-temperature seal. An infrared spectrum is produced from the radiation exiting the DRIFTS optics. Dips in this spectrum correspond to frequencies of radiation absorbed by either the MOF or the adsorbed species. Taking a spectrum of the MOF prior to adsorbing hydrogen into it (or, as the case may be, with the MOF exposed to an inert exchange gas such as helium) allows for differentiation between peaks arising from the MOF and those arising from adsorbed hydrogen.

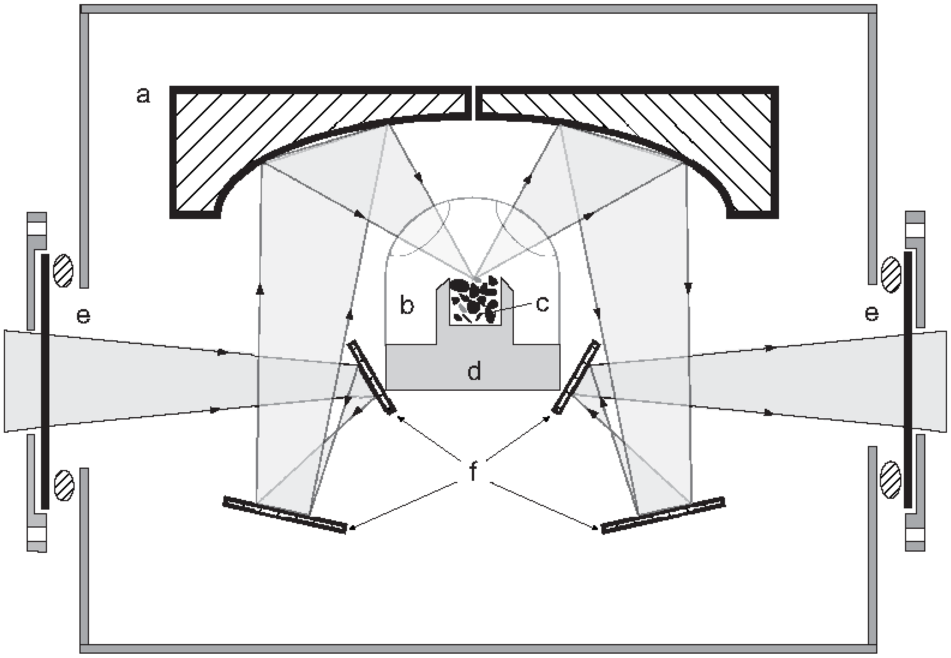

Figure 2.1: Schematic of the Diffuse Reflectance Infrared Fourier Transform Spectroscopy (DRIFTS) optics used in this work. The setup shown is kept under high vacuum ($< 10^{-5}$ mbar). (a) Ellipsoidal mirrors; (b) High-pressure dome; (c) MOF sample; (d) Copper sample holder and mount; (e) CaF_2 windows; (f) Plane mirrors. Image courtesy of [36].

2.2 Low Temperature Apparatus

The chamber shown in Figure 2.1 is kept under vacuum ($< 10^{-5}$ mbar). This evacuation accomplishes two tasks: (1) it removes infrared active molecules in the air (e.g. H_2O and CO_2) that would complicate the infrared spectrum unnecessarily, and (2) it allows for the cooling of the sample by a cryogenic cold finger. A schematic of the cold finger assembly used here is shown in Figure 2.2. The DRIFTS optics discussed in the previous section are shown, as well as a pictorial representation of the modified, liquid helium Janis ST-300T closed cycle cryostat cold finger used in this work. The cryostat has been modified by cutting off the outer vacuum wall, 10 cm above the copper sample mount, so evacuation of the chamber also evacuates the cryostat. This cold finger achieves temperatures as low as 15 K. The 15×12×15 cm welded aluminum vacuum chamber is also outfitted with a vertical alignment stage for the cold-finger–sample-mount assembly, a port for the high-pressure gas line going to the dome containing the sample, and a port for the vacuum line. An Alcatel ATP 100 Turbomolecular pump is used to evacuate the chamber. A small heating element is also in place, allowing control of the sample mount temperature.

The vacuum chamber detailed above is loaded into the large sample compartment of a modified Bomem DA3 Michelson interferometer. A <1 mbar vacuum is maintained within the spectrometer to further remove infrared active air molecules. This interferometer allows for a choice of broadband infrared source—in this work we use either a quartz-halogen or silicon carbide globar source. The Bomem interferometer uses a standard Michelson interferometry setup, as discussed in Section 2.4.1.

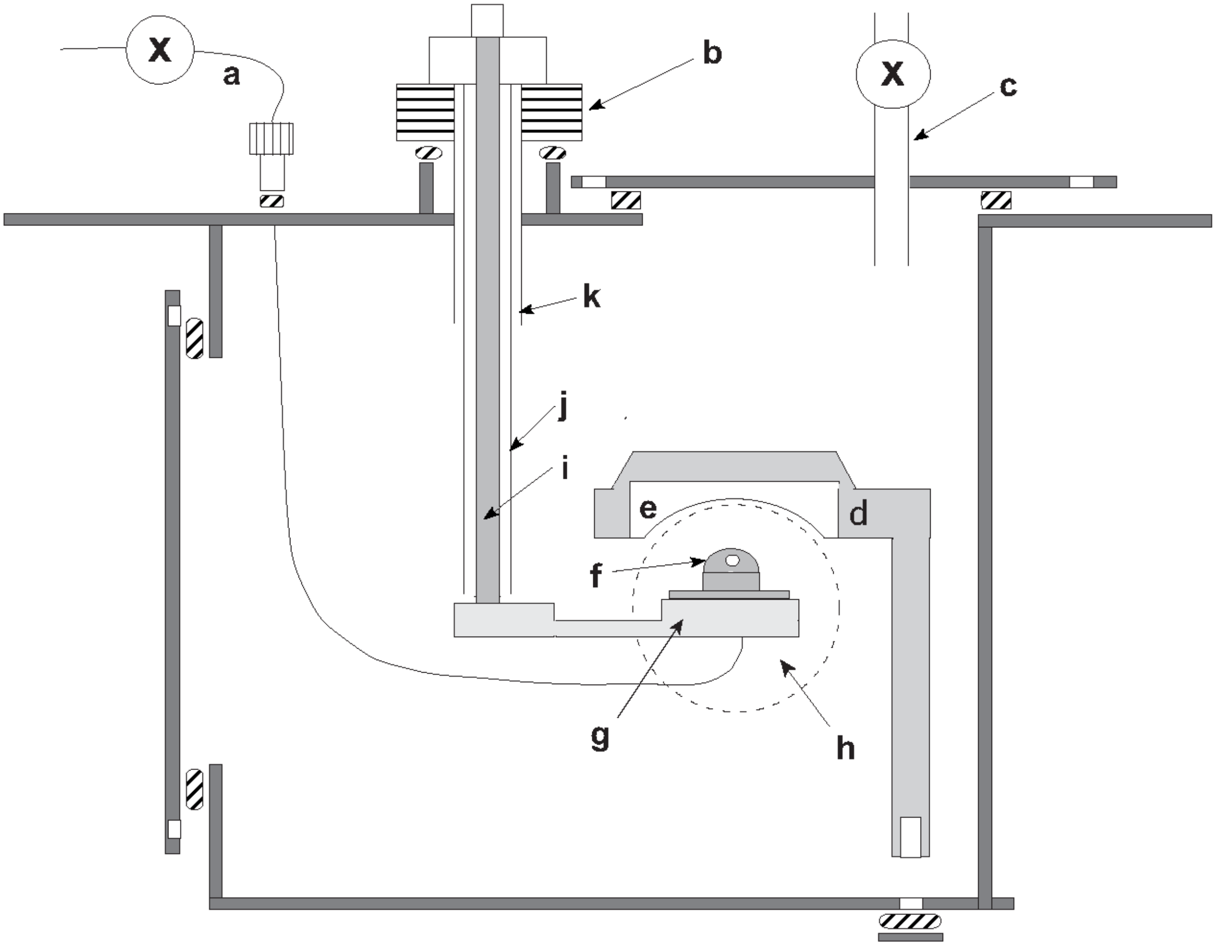

Figure 2.2: Schematic of the box containing the cryostat and Diffuse Reflectance Infrared Fourier Transform Spectroscopy (DRIFTS) optics used in this work. The setup shown is kept under high vacuum ($< 10^{-5}$ mbar). (a) High-pressure gas line; (b) Vertical alignment stage; (c) Vacuum line; (d) DRIFTS optics mount; (e) Ellipsoidal mirror; (f) High-pressure dome; (g) Copper sample mount; (h) CaF_2 window; (i) Cryostat cold finger; (j) Radiation shield; (k) Cryostat vacuum shell. Image courtesy of [36].

2.3 TDS Apparatus

The vacuum chamber, spectrometer, and sample configuration described in the sections above also constitute the apparatus used for TDS, with a few additions. The high-pressure gas line connected to the volume inside the sapphire-windowed steel dome is, on its other end, connected to a Micromeritics ASAP (Accelerated Surface Area and Porosimetry System) Model 2020 physisorption analyzer. This ASAP device allows for dosing of the MOF sample with specified amounts of hydrogen isotopologues (as well as other gases). As the volume inside a portion of the ASAP device is known very accurately, the amount of gas inside that volume can be calculated trivially from the pressure inside the volume using the ideal gas law. We employ two pressure gauges for this task, one high pressure gauge rated from 1 to 1000 mbar, and one low pressure gauge rated from 1 μbar to 10 mbar. The voltages from both pressure transducers are directed to a National Instruments (NI) SCB-68 Terminal Block, which acts as a computer interface allowing pressure measurements to be reported by NI LabVIEW software. The voltage from the temperature transducer of the Lakeshore temperature controller—which measures the temperature of the sample mount—is also directed to the interface and is read by the same LabVIEW software. A schematic of this TDS setup is shown in Figure 2.3.

The pressure gauges used in the ASAP device are Setra Vactron Model 760 and MKS Baratron 627 Series capacitance manometers. These gauges operate on the following principle: A circular electrode in close proximity to the back surface of a diaphragm forms a variable capacitor, where the small volume between electrode and diaphragm is kept at low pressure. As the pressure of the system the gauge is measuring increases, the diaphragm deflects toward the electrode. This causes an increase in the capacitance, which is detected and converted to a highly accurate direct current by an integrated circuit [52]. At most the uncertainty in pressure reading is 0.25%, at 25 μbar [53]. The advantage of these pressure gauges is twofold; they provide highly accurate and precise pressure measurement and need not be recalibrated for different gases.

Two silicon diodes are used to measure and control the temperature of the sample mount—one in the position on the sample mount shown in Figure 2.3, and one on the base of the cryostat cold finger. The use of two diode thermometers allows for precise temperature control with minimal oscillation about the temperature setpoint.

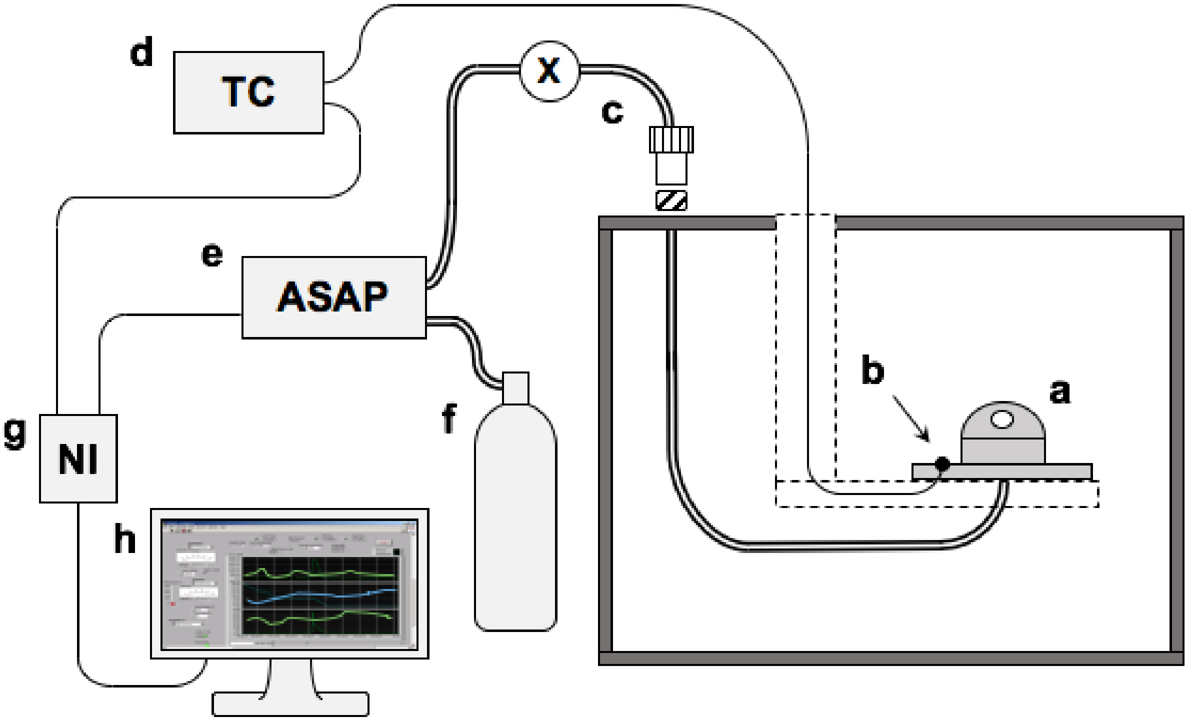

Figure 2.3: Schematic of the thermal-desorption spectroscopy apparatus used in this work. The apparatus builds off those shown in Figures 2.1 and 2.2. (a) High-pressure dome; (b) Four-probe silicon diode thermometer; (c) High-pressure gas line; (d) Temperature controller (TC); (e) Accelerated Surface Area and Porosimetry System (ASAP), responsible for gas dosing; (f) Gas tank connected to ASAP device; (g) National Instruments (NI) computer interface; (h) Computer running NI LabVIEW software, recording temperature and pressure.

2.4 Data Acquisition

2.4.1 Infrared Spectra

Collimated radiation emitted from a broadband, pseudo-blackbody infrared source is split along two perpendicular paths by the CaF_2 beamsplitter mentioned previously. One path consists of an evacuated chamber with a movable mirror at the end, and the other consists of an evacuated chamber with a fixed mirror. Radiation propagates along both paths and is directed back to the beamsplitter by the mirrors. The radiation from the two paths interferes upon recombination at the beamsplitter, and after being directed through the DRIFTS cryostat apparatus detailed above, the interference pattern is measured at the detector as a function of the position of the movable mirror. The movement of this mirror alters the relative phase of the two beams propagating along the paths; when this relative phase is zero, all frequencies of the incident light interfere constructively. This point of total constructive interference is referred to as the point of Zero Path Difference (ZPD), and, as the name suggests, occurs when the optical path length difference between the two arms of the interferometer is zero. The interference pattern as a function of this optical path length difference is referred to as an interferogram. A typical interferogram recorded by our system is shown in Figure 2.4(a), along with its Fourier transform in Figure 2.4(b). The result of this Fourier transform is referred to as a spectrum. Explicitly, the interferogram and spectrum constitute the following complex Fourier transform pair:

$$I(\delta) = \int_{-\infty}^{\infty} S(\nu) e^{i2\pi\nu} d\nu, \tag{2.1}$$

$$S(\nu) = \int_{-\infty}^{\infty} I(\delta) e^{-i2\pi\nu\delta} d\delta. \tag{2.2}$$

Here $I(\delta)$ is the interferogram as a function of optical path length difference δ and $S(\nu)$ is the spectrum as a function of spatial frequency ν. As it is stated in Equations (2.1) and (2.2), this Fourier transform pair is computationally intense to tabulate. The Bomem software accompanying our spectrometer does not perform the continuous Fourier transform. Instead, it uses the well documented fast Fourier transform (FFT) method, which relies heavily on discrete Fourier transformation (DFT), wherein the integrals in (2.1) and (2.2) are recast as discrete sums. For more information on FFT and DFT see Refs. [32, 33], and for more

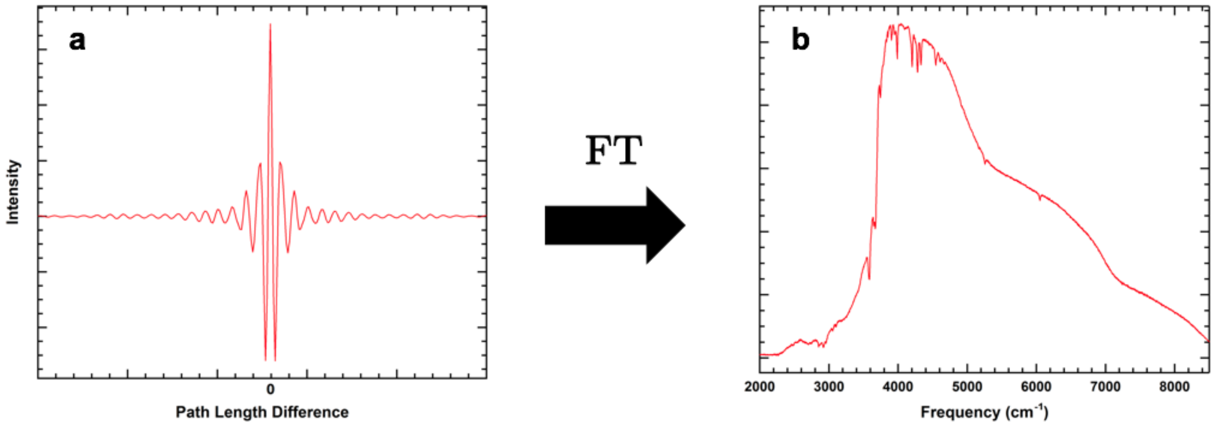

Figure 2.4: (a) A typical interferogram recorded by the spectrometer used in this work. (b) The Fourier transform (FT) of this interferogram, a typical spectrum. (Data taken with Co-MOF-74 (dobdc) at 1 cm^{-1} resolution, averaging 100 scans.)

information on the specific software used in this work see Ref. [54].

In broad strokes then, the Michelson interferometer used in this work measures intensity of infrared radiation as a function of the position of a moving mirror. The resulting interferogram—a plot of intensity versus path length difference between the to arms of the interferometer—can be Fourier transformed to give a spectrum of this intensity as a function of spatial frequency. By placing an infrared active sample after the interferometer, this spectrum gives information on the infrared absorption of the sample.

As the variables in the Fourier transform pair δ and ν must satisfy the inequality $\Delta\delta\Delta\nu \geq 1$ [55], the frequency resolution of an FTIR spectrometer is determined by the distance traveled by the movable mirror, $\Delta\delta$. A larger $\Delta\delta$ corresponds to a smaller $\Delta\nu$, so the further the movable mirror travels, the better the frequency resolution of the corresponding spectrum. Conveniently, this resolution is usually reported in wavenumbers (cm^{-1}), making the distance traveled by the mirror simply the reciprocal of the resolution. The inconvenience of this convention is that better, or 'higher' resolution spectra are in fact taken at resolutions corresponding to smaller wavenumbers. The natural drawback to higher resolution scans then, is that it takes longer for the mirror to move the larger distances that are required. This is a particularly pertinent concern in the case of *in situ* IR spectroscopy during TDS, when IR spectra are obtained while the sample temperature is continuously increasing and conditions of the adsorbed hydrogen are continuously changing. The spectra presented in the next chapter are taken at resolutions of either 4 or 1 cm^{-1} and are averages of 100 or 2000 scans, where one scan is defined by the movement of the mirror from one extremum to the other extremum and back. In 4 cm^{-1} spectra the mirror moves $1/4$ cm from extremum to extremum, at a speed of ∼1 cm/sec; thus 1 scan takes ∼$1/2$ a second, and 100 scans takes ∼50 seconds. 100 scan 1 cm^{-1} spectra take ∼200 seconds, and 2000 scan 1 cm^{-1} spectra take just over one hour to complete.

A few miscellaneous comments on the functioning of the spectrometer used in this work are warranted: A common concern with precision spectrometers of the sort used here is with regards to tilting or wobbling of the movable mirror as it travels. Any tilting of this mirror affects how the beams from the two arms of the interferometer recombine, and thus affects the precision and accuracy of the spectrometer as a whole. The Bomem DA3 spectrometer incorporates a compensating mechanism that automatically adjusts the orientation of the mirror to maintain the alignment and assuage this concern. Another concern inherent to precision spectroscopy is how we know the exact position of the movable mirror, and by extension how we know the exact optical path length difference between the two interferometer arms. One could simply approximate the movement of the mirror as occurring at a constant velocity and calculate the position of the mirror accordingly, however this approach is insufficient when considering the turnaround points of the movable mirror. The spectrometer used here instead determines the relative position of the two mirrors to high accuracy with the use of an auxiliary helium-neon (HeNe) laser. As the wavelength of HeNe lasers are known very accurately [56] and the interference pattern of HeNe laser light in a Michelson interferometer is equally well known, based on the measured interference pattern of the HeNe beam, the optical path length difference between interferometer arms can be tabulated with sufficient accuracy.

By placing a MOF after this interferometer (in the apparatus discussed above) and before the detector, we can determine the spectrum of this MOF and thereby determine the spatial frequencies of its infrared absorption. By subsequently loading hydrogen into the MOF, we can determine the spatial frequencies of the hydrogen's infrared absorption.

2.4.2 Thermal-Desorption Spectra

The procedure for acquisition of TD spectra presented in this work is straightforward. An amount of hydrogen isotopologue gas is adsorbed into a MOF at a temperature cool enough to allow for adsorption yet warm enough to allow the adsorbed molecules to reach thermal equilibrium. Loading the adsorbate at this temperature ensures that the individual adsorbing molecules find global potential minima rather than being stuck in local potential minima—so-called 'secondary sites.' Empirical evidence suggests a loading temperature of 77 K is sufficient for this purpose, and, conveniently, is consistent with the boiling point of nitrogen, a common point of reference in the literature. The isotopologue–MOF, adsorbate–adsorbent system is then cooled at a sufficiently slow rate to a temperature such that near-all isotopologue molecules are adsorbed into these global potential minima. Empirical evidence shows a rate of 5 K/min to a temperature of 15 K to be sufficient for these purposes. The sample is then heated at a constant rate and the pressure of the desorbing molecules is recorded as a function of temperature. Pressure is then converted to number of molecules desorbed with application of the ideal gas law

$$PV = nk_{\mathrm{B}}T, \tag{2.3}$$

where P is a pressure, V a volume, n the number of molecules, and T a temperature. The resulting function for number of molecules desorbed is differentiated with respect to time. This differentiation leads to the function $\frac{dn}{dt}$, which can be plotted against temperature in accord with the approach described in Section 1.7.

When converting from pressure to number of molecules desorbed, we rely on the assumption that the volume of the dome is at a temperature given by our measured temperature function, $T(t)$, and that the relevant volume of the ASAP device is at room temperature, $T_{\mathrm{room}} = 293$ K. We have measured the volume of our dome to be $V_{\mathrm{dome}} = 1.93(2)$ cm^3, and the relevant volume of the ASAP device to be $V_{\mathrm{ASAP}} = 48.5(1)$ cm^3. We further assume that the pressure $P(t)$ read in the ASAP device volume is the same as the pressure within the dome, leading to the following function for desorbed molecules with time t:

$$n(t) = \frac{P(t)}{k_{\mathrm{B}}}\left(\frac{V_{\mathrm{ASAP}}}{T_{\mathrm{room}}} + \frac{V_{\mathrm{dome}}}{T(t)}\right) \tag{2.4}$$

Standard error propagation through Equation (2.4)—with an overestimate of the uncertainty in $P(t)$ of 0.25% (the largest uncertainty cited by the manufacturer [53]), an uncertainty in T_{room} of 1%, uncertainty in $T(t)$ of 5%, and uncertainties in V_{ASAP} and V_{dome} given above—leads to an overestimate in random uncertainty of $n(t)$ of 6%.

The generalized procedure for taking the thermal-desorption and *in situ* infrared spectra presented in this work is then the following: The MOF–dome system is evacuated and cooled to ~77 K. As MOFs generally have very low thermal conductivity, there is a natural worry that the temperature of the MOF will not be the same as the temperature of our thermometer; as such, 1 mbar of helium (He) exchange gas is loaded into the dome volume at this point to establish constant temperature. Helium is chosen as it is largely inert and only adsorbs into a MOF at the lowest of temperatures (<20 K). This 1 mbar value refers to the pressure of He inside V_{ASAP}. Such a small amount is chosen so as not to complicate our TD spectra unnecessarily, while still ensuring constant temperature. A 100 scan, 1 cm^{-1} resolution IR spectrum of the MOF is acquired at 77 K to act as a reference for IR spectra of the MOF containing hydrogen. At ~77 K, an amount of hydrogen isotopologue gas is loaded into the dome volume, and the system is cooled to ~15 K at a rate of 5 K/min. At ~15 K, a 2000 scan, 1 cm^{-1} resolution IR spectrum is acquired. As this spectrum takes ~1 hour, the adsorbed molecules have the further opportunity to come to thermodynamic equilibrium (though, at low temperature, the kinetics are certainly slowed). The system is then heated to 250 K at a rate of 5 K/min, while multiple 100 scan, 1 cm^{-1} resolution IR spectra are acquired. Deviations from this generalized procedure are noted in the following chapter.

2.5 Data Manipulation

2.5.1 Infrared Spectra

To obtain the infrared absorption spectrum of adsorbed hydrogen alone, we reference an IR spectrum of hydrogen adsorbed into a MOF to an IR spectrum of the MOF with no adsorbed hydrogen. All of the spectra presented in this thesis have been manipulated in this way, and, strictly speaking, are what is referred to in the literature as 'absorbance spectra.' Absorbance spectra, $A(\nu)$, are also functions of spatial frequency (ν), and bear the following mathematical relationship to the FTIR spectra described earlier:

$$A(\nu) = -\ln\left(\frac{S(\nu)}{S_0(\nu)}\right), \tag{2.5}$$

where $S(\nu)$ is an FTIR spectrum of hydrogen adsorbed into a MOF and $S_0(\nu)$ is an FTIR spectrum only of the MOF. Qualitatively, these absorbance spectra are sets of peaks corresponding to vibrational, rotational, and translational infrared transitions. The area under each peak is directly proportional to the amount of hydrogen adsorbed and the dipole moment of the adsorbed hydrogen.

When cooling the system to cryogenic temperatures, some thermal contraction is unavoidable. Explicitly, the thermal contraction of our cryostat cold finger, approximated as a rod, is

$$\Delta L = \alpha L \Delta T. \tag{2.6}$$

Here α is the coefficient of linear thermal expansion intrinsic to each material ($\sim 17\ \mu(\mathrm{K}^{-1})$ for copper), L is the length of the cold finger, and ΔT is the change in temperature. As the cold finger is approximately 20 cm long, upon cooling from 77 K to 15 K we expect around 0.2 mm of contraction. This length contraction is several hundred times the wavelength of infrared light, and accordingly has a non-negligible effect on the alignment of our highly sensitive DRIFTS optics. As the reference spectrum, $S_0(\nu)$, is generally taken at ~77 K and the spectrum of interest, $S(\nu)$, is generally taken at ~15 K, we expect this amount of change in alignment and IR signal strength between the two spectra. This change in alignment results in sloping, nonzero baselines, apparent in our absorbance spectra. These baselines are removed manually from our absorbance spectra with the Bomem spectrometer GRAMS software.

These two manipulations of our IR data allow for direct, uniform comparison of IR peaks and spectra.

2.5.2 Thermal-Desorption Spectra

Data on the number of desorbed molecules, $n(t)$, acquired with the procedure outlined above are differentiated with respect to time t to produce the function $\frac{dn}{dt}(t)$. These data for $\frac{dn}{dt}(t)$ are plotted against temperature T in accordance with the approach described in section 1.7, and a TD spectrum is produced. The total area underneath a TDS curve produced according to this procedure is directly proportional to the total number of molecules desorbed and is inversely proportional to the ramp rate. If we heat the system to a sufficient temperature such that all hydrogen initially adsorbed is desorbed, then the total area is also proportional to the number of molecules initially adsorbed.

The amount of hydrogen adsorbed into a given MOF is reported in terms of H_2 (or D_2 or HD) per open metal, or per primary site. This value is calculated based on the measured mass of the MOF that is loaded into the apparatus, the molar mass of the specific MOF, and the pressure of the hydrogen gas when at room temperature inside the known volume V_{ASAP}. To get the concentration of H_2 per metal, the pressure inside V_{ASAP} is converted to a number of hydrogen molecules with trivial application of the ideal gas law (Equation (2.3)), the mass of the MOF is converted to the number of open metals with the knowledge of the molar mass and metals per mole (as determined by the MOF's chemical formula), and the ratio of the two is taken. When there is a disparity between the number of primary binding sites and the number of open metals, the ratio is taken with respect to the number of primary binding sites (e.g. VSB-5 has 1 primary site per 4 nickel atoms—we report the H_2 concentration in terms of hydrogen molecules per primary site, instead of per 4 metal atoms).

Chapter 3: Results and Analysis

3.1 Co-MOF-74 (dobdc)

We begin our IR and TDS analysis of the MOFs under consideration with the most well-characterized in the literature: Co-MOF-74 (dobdc) [12, 22, 27, 29, 39]. We first present evidence for the reproducibility of our TD spectra. After establishing this reproducibility, we investigate the primary adsorption site—the cobalt open-metal site—as we report its TDS and *in situ* IR signature. Importantly, we observe a definite shift to higher temperature of the TD spectrum of D_2 when compared with H_2. This effect sheds light on the efficiency of Co-MOF-74 (dobdc) for Zero Point Energy Separation (ZPES) of hydrogen isotopologues, and speaks to the ability of our technique to probe this efficiency in MOFs more generally. We then present the TDS signature of the secondary, tertiary, and quaternary adsorption sites in Co-MOF-74 (dobdc), along with corresponding IR spectra. These adsorption sites are shown to exhibit sequential loading. Our ability to acquire IR and TD spectra as a function of hydrogen per cobalt concentration (as opposed to loading pressure—an approach more commonly taken in the literature) proves indispensable as it allows for acquisition of this site-specific information. We further probe the desorption dynamics of hydrogen adsorbed only onto the open-metal site, as we present coverage–varying and ramp-rate–varying TDS. With this latter set of TDS data we carry out a form of data analysis common in surface science literature in an attempt to extract the binding energy of the open-metal site in Co-MOF-74 (dobdc). After comparison with literature values, we conclude that this common analysis technique leads to an unphysical result for the binding energy, and while suitable for surface desorption, may not be suitable for hydrogen desorption from three-dimensional MOF structures. We accordingly seek to dissuade groups from applying this surface analysis technique to MOF desorption, as has begun to occur in the literature [57]. We further

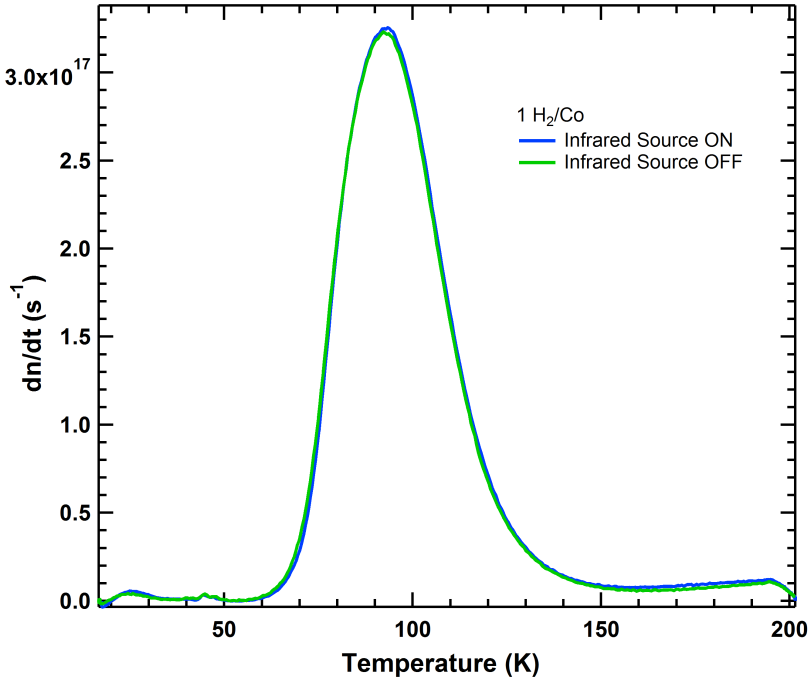

Figure 3.1: TD spectra of H_2 adsorbed onto the primary, open-metal site of Co-MOF-74 (dobdc) at a concentration of ~1 H_2 per cobalt (Co). One spectrum was acquired with the infrared source of the spectrometer on, one with it off; notably, the spectra are highly reproducible and the presence of the infrared source makes a negligible difference in the TD spectrum.

present an uncommon but straightforward form of analysis of a single TD spectrum: *ab initio* fitting of the spectrum to the Polanyi-Wigner equation. We perform these fits in both the desorption-order–independent and –dependent regime, and comment on the physicality of the results. Ultimately we conclude that thermal desorption of hydrogen from MOFs cannot be described accurately by the coverage-independent Polanyi-Wigner equation. While it provides pertinent information on the identification of adsorption sites, and the efficiency of isotopologue separation at these sites, our TDS method should thus not be used for extracting the binding energy of these sites. Instead, we suggest the use of isotherm analysis to extract the binding energy, which can be performed with the same apparatus as our TDS technique.

Figure 3.1 shows the TD spectrum of H_2 adsorbed onto the primary, open-metal site of Co-MOF-74 (dobdc), at a concentration of ~1 H_2 per cobalt (Co). Two spectra are

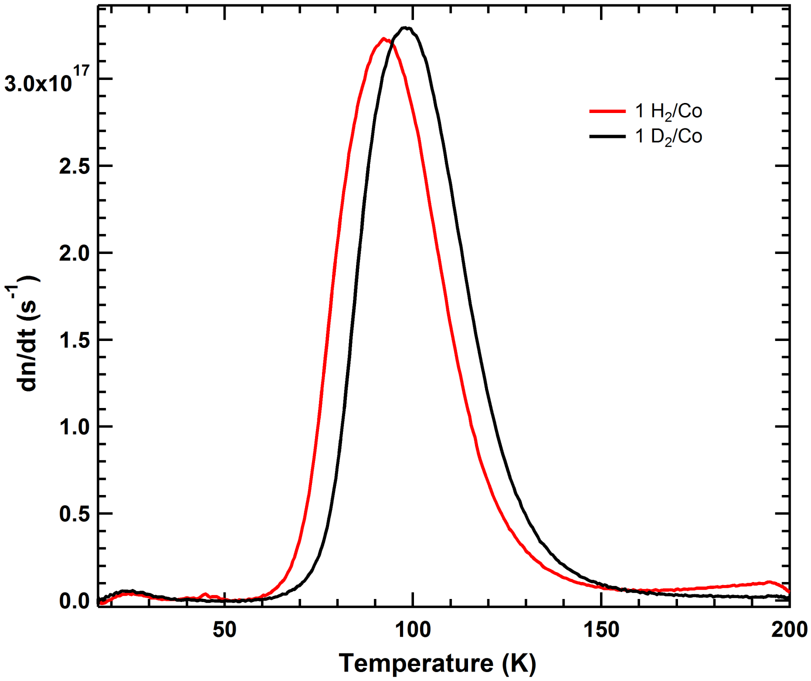

Figure 3.2: TD spectra of H_2 and D_2 adsorbed onto the primary, open-metal site of Co-MOF-74 (dobdc) at a concentration of ∼1 H_2 (or D_2) molecule per cobalt (Co).

presented, one taken with the TDS procedure outlined in Section 2.4.2, and one taken with an identical procedure in all respects except that IR spectra were not taken during the heating process. This figure provides two pertinent pieces of information: (1) that our TDS technique provides highly reproducible spectra, and (2) that the presence of an IR source makes a negligible difference in the TD spectrum. This latter piece of information allows us to take *in situ* IR spectra during TDS without fear of altering the TD spectrum.

Figure 3.2 presents the TDS signature of the primary, open-metal site of Co-MOF-74 (dobdc) for H_2 and D_2. Importantly, we can easily distinguish these spectra—the D_2 spectrum is clearly shifted to higher temperature than the H_2 spectrum. Given the reproducibility of our TD spectra established above, we can be certain this effect is intrinsic to the difference in adsorption properties of H_2 and D_2. Accordingly, our simple TDS technique provides pertinent information for H_2–D_2 separation through ZPES, as discussed in Section 1.1.1. We report temperatures of maximum desorption rate of $T^{\mathrm{H_2}}_{\mathrm{max}} = 92 \pm 5$ K for H_2 and $T^{\mathrm{D_2}}_{\mathrm{max}} = 98 \pm 5$ K for D_2, where we have taken the uncertainty in T_{max} to be 5%—the uncertainty in $T(t)$. The Full Width at Half Maximum (FWHM) of each peak is 32 ± 2 K, where we have taken the uncertainty here as the sum in quadrature of the uncertainty in temperature at each half-maximum (—5%, leading to an uncertainty in FWHM of 7%).

In the infrared, we see little evidence of D_2, but we do observe H_2 absorption peaks. Shown in Figure 3.3(a) is the infrared absorbance spectrum of H_2 in Co-MOF-74 (dobdc), at a concentration of $\sim$1 H_2/Co. This spectrum was taken at 1 cm^{-1} resolution, and is an average of 2000 scans. We follow the precedent set by Ref. [39], and label the two overlapping peaks around 4047 cm^{-1} as Q(1) and Q(0), and the peaks $\sim$200 cm^{-1} blueshifted from these as Q_{trans}—peaks arising from translational coupling to these fundamental vibrational Q transitions. The separation between the vibrational peak and the corresponding translational peak represents center of mass translational mode frequency. The presence of these IR peaks that have previously been identified as corresponding to the primary site in Co-MOF-74 (dobdc) give us further confidence in labeling the TDS peaks in Figures 3.1 and 3.2 as arising due to desorption from the primary site. Figure 3.3(b) shows the *in situ* IR spectra of H_2 in the open-metal site of Co-MOF-74 (dobdc) taken simultaneously with the TD spectrum shown in Figure 3.2. These spectra were taken at 4 cm^{-1} resolution, and are averages of 100 scans. Notably, we observe the disappearance of these IR peaks at temperatures consistent with what we observe in the TD spectra.

We now report on the desorption dynamics of Co-MOF-74 (dobdc) more generally, as we include in our discussion the secondary, tertiary, and quaternary adsorption sites. Figure 3.4 shows the TDS signature of all four adsorption sites, for (a) D_2 and (b) H_2. Importantly, these TD spectra agree with those in the literature for Co-MOF-74 (dobdc) [13]. Each D_2 desorption peak is shifted to slightly higher temperature than those same peaks for H_2; dotted lines guide the eye to this effect. Notably, the sites load in a highly systematic, sequential fashion—at the lowest loading, hydrogen occupies only the primary, open-metal site, and as the loading is increased the secondary, tertiary, and quaternary sites are occupied sequentially. An interesting feature of these spectra is that for both D_2 and H_2 the tertiary peak shifts to lower temperature upon increased loading (difference between green and blue spectra). This may indicate repulsive hydrogen–hydrogen interactions at this site. Finally, while we see clear evidence of a quaternary peak in the 4.5 H_2/Co spectrum in Figure 3.4(b), this quaternary peak seems to be overlapping with the tertiary peak in the case of D_2 (purple spectrum in Figure 3.4(a)). The presence of these four sites agrees with inelastic neutron scattering of hydrogen in Co-MOF-74 (dobdc) [22, 58].

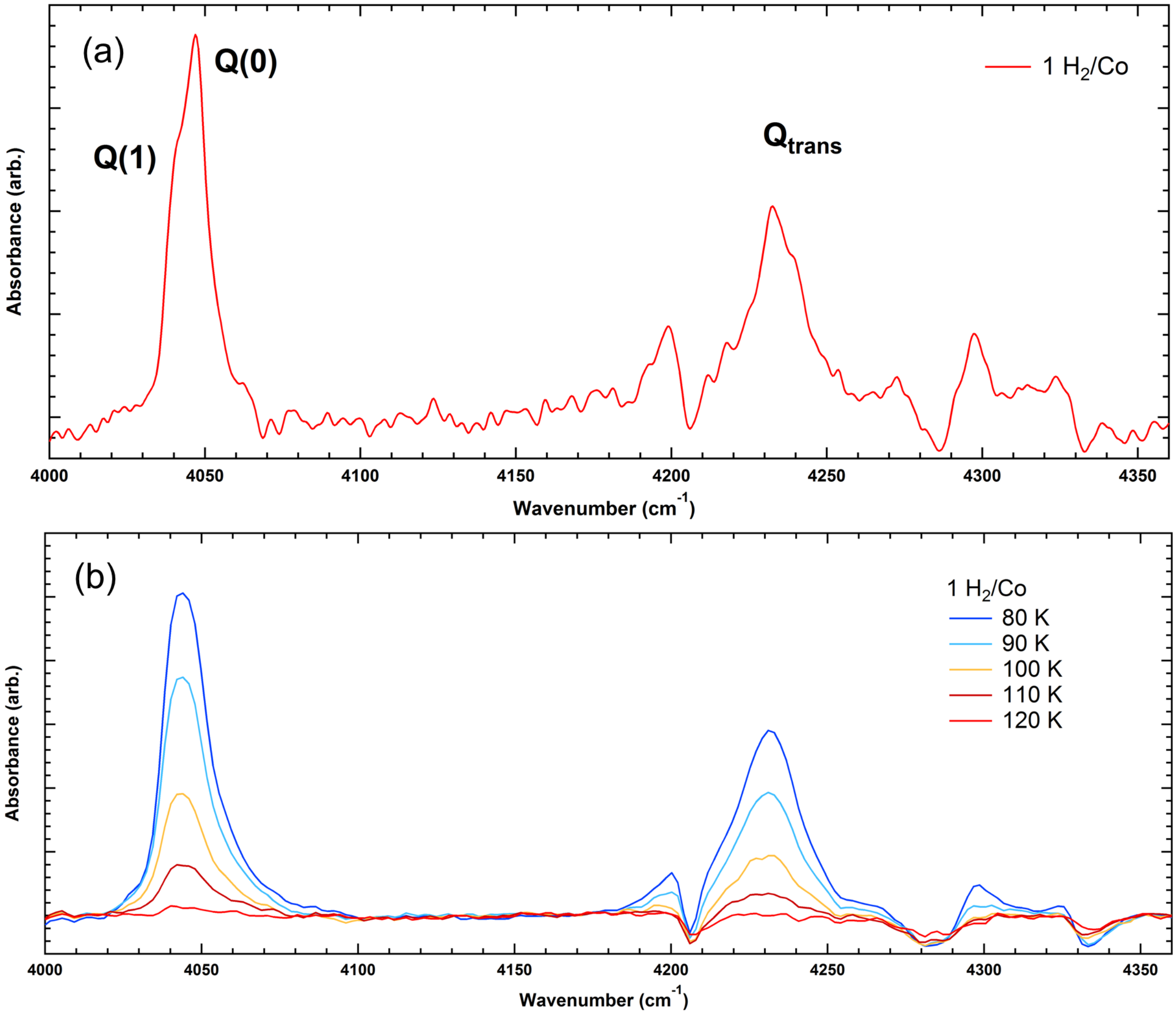

Figure 3.3: IR spectra of H_2 adsorbed onto the primary, open-metal site of Co-MOF-74 (dobdc) at an initial concentration of ~1 H_2 per cobalt (Co). (a) Following the precedent set by Ref. [39], we label the Q(1) and Q(0) peaks, as well as those translational peaks resulting from these Q transitions, Q_{trans}. This spectrum was taken at 1 cm^{-1} resolution, and is an average of 2000 scans. (b) *In situ* spectra of H_2 in the open-metal site of Co-MOF-74 (dobdc) taken simultaneously with the TD spectrum shown in Figure 3.2. These spectra were taken at 4 cm^{-1} resolution, and are averages of 100 scans.

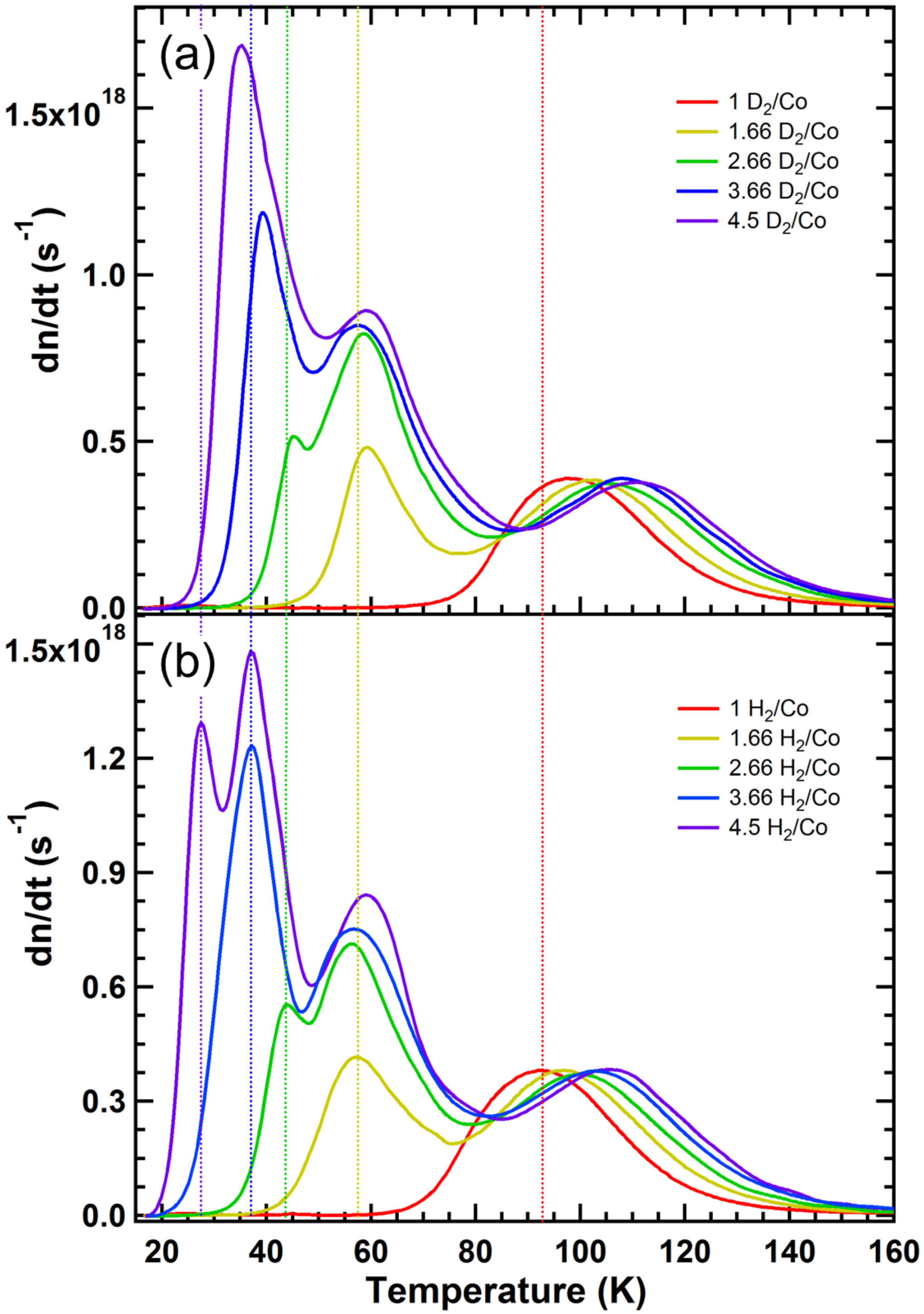

Figure 3.4: (a) TDS signature of D_2 in Co-MOF-74 (dobdc), for varying coverage. (b) An identical set of TD spectra H_2. Dotted lines are drawn to guide the eye when comparing D_2 and H_2 peaks.

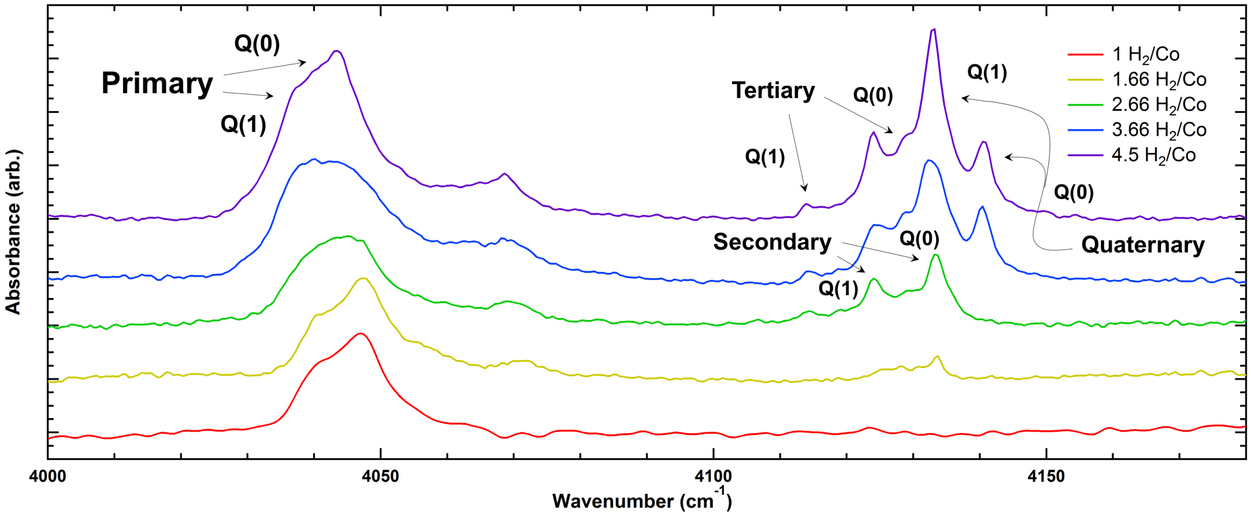

Figure 3.5: IR spectra of H_2 in Co-MOF-74 (dobdc) for varying concentrations. All spectra are an average of 2000 scans at resolution 1 cm^{-1}, taken at 15 K. Spectra are offset for clarity.

These TD spectra also give us an information on the effect of readsorption in our TDS technique. We take it that the systematic shift to higher temperature of the primary site peak upon increased loading is not the result of anything physical inside the MOF. Instead, we attribute this shift to readsorption. In all the spectra, once the system reaches 85 K (or 90 K for D_2), nearly all of the hydrogen has been desorbed from the secondary, tertiary, and quaternary sites. (For the ~1 H_2/Co spectrum, this is trivial as there was never hydrogen in these sites to begin with.) Thus, after 85 K, all the spectra should be identical—all that should be recorded in the TD spectrum after this temperature is desorption from the primary site, and this desorption should be exactly the same as when there was only hydrogen on the primary site to begin with. Clearly, however, we do see a shift in the primary site peak as the initial loading increases. As the only systematic difference between these spectra is the initial loading, and as the likelihood of readsorption of a given molecule should increase with pressure outside the MOF, we attribute this systematic shift to readsorption. The systematic nature of this readsorption effect, combined with its small magnitude—causing a shift of 10 K only after more than quadrupling the initial loading—does not detract from the qualitative structure of these TD spectra.

This sequential loading also agrees with and informs the structure of Co-MOF-74 (dobdc)

IR spectra. Shown in Figure 3.5 are five IR spectra of H_2 in Co-MOF-74 (dobdc), corresponding exactly to the five TD spectra shown in Figure 3.4(b). These spectra were all taken at 15 K at 1 cm^{-1}, and are averages of 2000 scans. The results of our TD spectra allow us to label these IR peaks in a site-specific fashion as they sequentially appear with increases in concentration. Notably, this labeling method agrees with the treatment given in Ref. [39]. First at a loading of 1.66 H_2/Co, Q(1) and Q(0) peaks for the secondary site appear, ∼100 cm^{-1} blueshifted from the primary Q(1) and Q(0) peaks. Then, at higher concentrations, two more peaks appear in this same region of the IR spectrum. We label these two peaks Q(1) and Q(0) arising from the tertiary site. Finally, at concentrations higher than 3 H_2/Co, the most blueshifted peak appears and the central feature (that we attributed to Q(0) transition of H_2 on the secondary site) grows. We take this highly blueshifted peak to be the Q(0) transition of H_2 on the quaternary site, while we take it that the Q(1) peak is overlapping with the secondary Q(0) peak. The translational peaks shown previously remain largely unchanged through this process. The locations of these IR features, as well as those peaks seen in the TD spectra, are summarized in Table 3.1. The uncertainty of 1 cm^{-1} in FTIR peak location has been established for our system by Refs. [24, 36, 37, 51].

Continuing the investigation of desorption from the open-metal site, we next examine the effect of varying initial coverage, and of varying ramp-rate on the open-metal site TDS signature of Co-MOF-74 (dobdc). The effect of varying initial coverage is shown in Figure 3.6(a), for initial coverages of ∼1, 0.8, 0.6, 0.4, and 0.2 H_2/Co. Here each peak has been scaled by respective initial coverage. In Section 1.7, we saw that for the case of first-order, coverage-independent Arrhenian desorption, these scaled peaks are identical. Notably, the peaks in Figure 3.6(a) are not identical, and in fact display highly systematic shifts to lower temperature and broadening with increases in initial coverage.

There are two possible explanations for this shift and broadening: (1) As any physical MOF has a distribution of primary sites arising from imperfections in the crystal lattice, etc., at low initial coverage only the strongest binding primary sites are occupied. Upon increasing the initial coverage, weaker binding primary sites are populated, and the ‘effective’ binding energy of the MOF appears to have decreased. This lower effective binding energy results in a peak with a lower T_{max}, and the increased distribution of sites leads to a broader peak. (2) The desorption simply cannot be described by the first-order, coverage-independent Polanyi-Wigner equation. While the premise of (1) is certainly true, it is difficult to know how much

Isotopologue	Adsorption Site	TDS T_{max} (K)	FTIR Peak Location (cm^{-1})
H_2	Primary	92 ± 5	Q(1): 4047 ± 1 Q(0): 4041 ± 1 Q_{trans}: 4199 ± 1 4232 ± 1 4298 ± 1
	Secondary	57 ± 3	Q(1): 4124 ± 1 Q(0): 4133 ± 1
	Tertiary	44 ± 2*	Q(1): 4114 ± 1 Q(0): 4129 ± 1
	Quaternary	27 ± 1	Q(1): 4133 ± 1 Q(0): 4140 ± 1
D_2	Primary	98 ± 5	n/a
	Secondary	59 ± 3	n/a
	Tertiary	45 ± 2*	n/a
	Quaternary	35 ± 2	n/a

*Peak shifts to lower temperature by ~7 K upon increased loading.

Table 3.1: Summary of TDS and FTIR peak locations for H_2 and D_2 in Co-MOF-74 (dobdc).

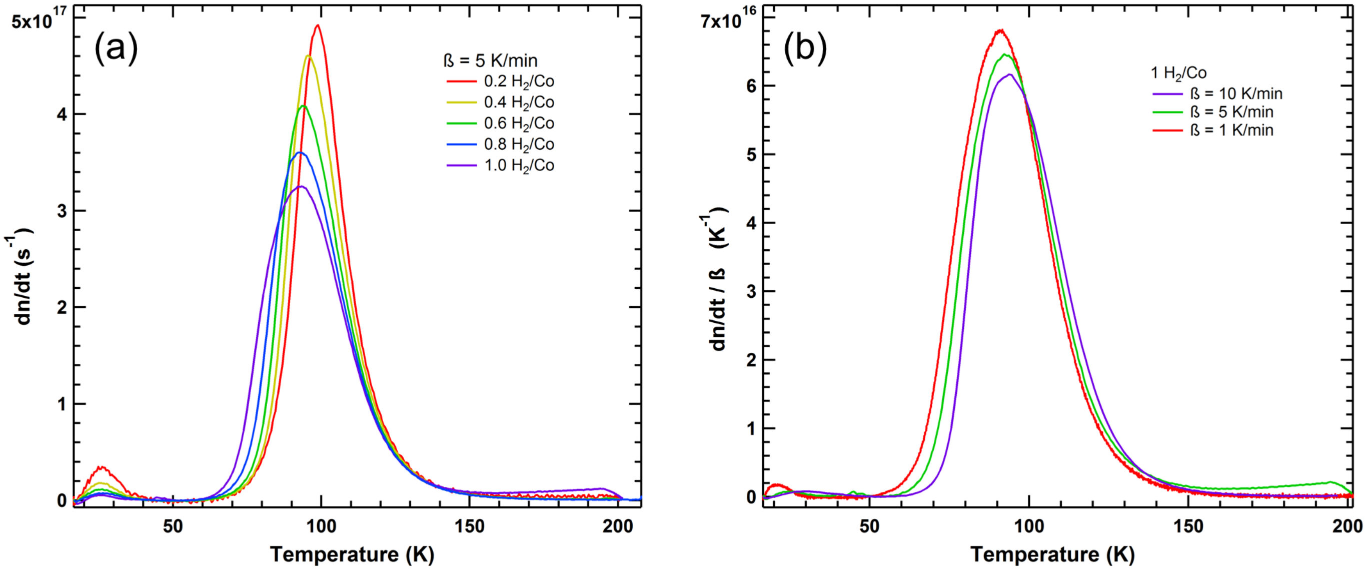

Figure 3.6: TD spectra of H_2 adsorbed onto the primary, open-metal site of Co-MOF-74 (dobdc) at (a) concentrations ranging from $\sim$1 H_2/Co to $\sim$0.2 H_2/Co, and (b) at a concentration of $\sim$1 H_2/Co for varying ramp rate, β. Spectra in (a) have been scaled by their respective initial concentrations. For clarity, the spectra in (b) have been scaled by their respective ramp rates.

of a shift in $T_{\max}$ and increase in peak width to expect. More evidence would be required to accept explanation (2), so we take no definite stance on the explanation here.

The ramp-rate–dependence of the open-metal site TD signature is shown in Figure 3.6(b). Here we observe shifts to higher temperature and perhaps some broadening upon increases in ramp rate. This kind of behavior has been well documented in the literature [48, 57, 59], and a noteworthy technique has been developed for extracting the binding energy out of such a ramp-rate varying family of TD spectra. The technique begins with differentiating the Polanyi-Wigner equation (Equation (1.19)) with respect to time, rearranging the expression evaluated at $T_{\max}$, and taking the natural logarithm of both sides to find:

$$\ln\left(\frac{\beta}{T_{\max}^2}\right) = -\frac{E_{\mathrm{b}}}{k_{\mathrm{B}} T_{\max}} + \ln\left(\frac{\nu k_{\mathrm{B}}}{E_{\mathrm{b}}}\right), \tag{3.1}$$

where, as before, β is the temperature ramp rate, E_{b} is the binding energy, k_{B} is Boltzmann's constant, and ν is the pre-exponential factor. Thus if a family of desorption curves are acquired with varying ramp rate, a plot of $\ln\left(\frac{\beta}{T_{\max}^2}\right)$ versus $\frac{1}{T_{\max}}$ yields a straight line with

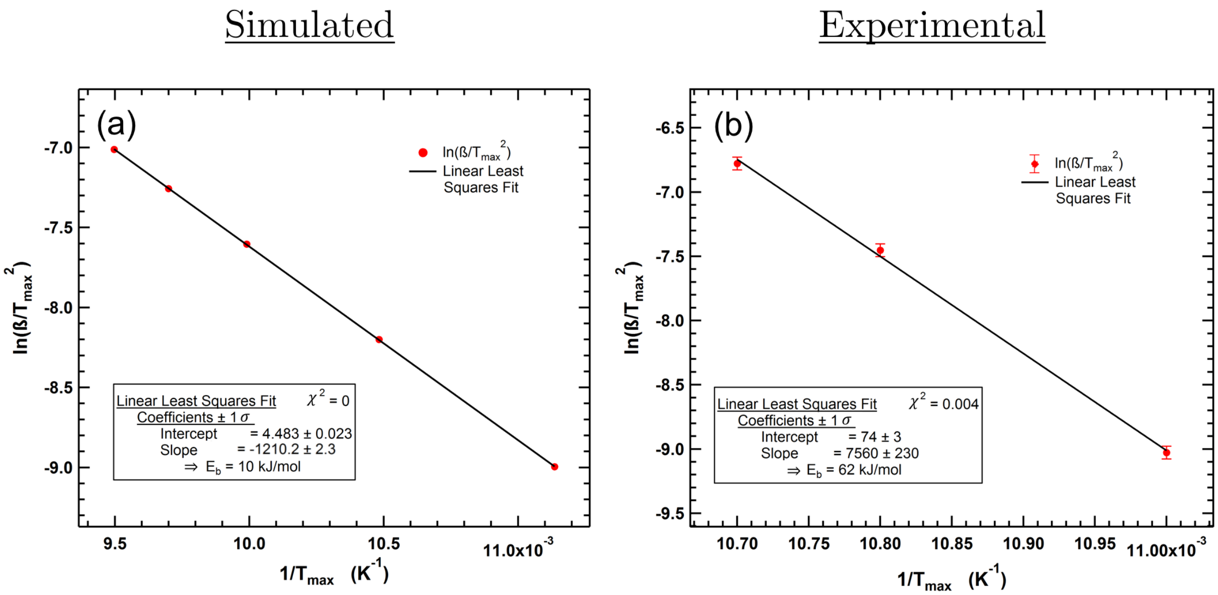
Simulated

Experimental

Figure 3.7: (a) Plot of $\ln(\beta/T_{\mathrm{max}}^2)$ for the simulated family of TD spectra in Figure 1.10(c), where β is the temperature ramp rate and T_{max} is the temperature of maximum desorption rate. (b) An identical plot for the family of TD spectra in Figure 3.6(b). While the slope of (a) can be used to correctly extract the simulated binding energy, the slope of (b) yields an unphysical binding energy for Co-MOF-74 (dobdc).

slope $\frac{E_{\mathrm{b}}}{k_{\mathrm{B}}}$. Figure 3.7(a) shows this analysis technique applied to the simulated data in Figure 1.10(c). The plot is indeed a straight line, which, when a linear least squares fit is performed, leads to a χ^2 of 0. The input binding energy of $E_{\mathrm{b}} = 10$ kJ/mol can be extracted correctly from the slope of this line, as described. Figure 3.7(b), however, shows the technique applied in an identical fashion to the data in Figure 3.6(b). Standard uncertainty propagation is used through Equation (3.1). While the three data do fall along a straight line, the binding energy extracted through this technique is $E_{\mathrm{b}} \approx 62$ kJ/mol. As the binding energy of Co-MOF-74 (dobdc) reported in the literature is $E_{\mathrm{b}} \approx 10.8$ kJ/mol [28], we take this to be an unphysical result. While suitable for two-dimensional surface desorption more closely following the Polanyi-Wigner Equation, we take this to be an inviable method for extracting the binding energy of a three-dimensional adsorbent, such as a MOF. At the very least, it is an inviable method for the novel TDS technique presented in this thesis. Until conclusively proven viable for MOF desorption using evacuation techniques, we seek to dissuade the use of this form of data analysis for TDS in MOFs, as has begun to occur in the field [57].

Another method of analysis for these TD spectra is fitting of the data *ab initio* to the Polanyi-Wigner equation, Equation (1.19). While this is a seemingly straightforward method of analysis, it is not one often reported on in the literature. Figure 3.8(a) shows such an *ab initio* fit to a single simulated TD spectrum. This *ab initio* fit correctly extracts the pre-exponential factor ν, and the binding energy E_{b}. These fits were performed with IGOR Pro analysis software. The identical fitting procedure is performed on the experimental D_2 spectrum of Figure 3.2, where $\frac{dn}{dt}(t)$ was converted to $\frac{d\theta}{dt}(t)$ with the manipulation given by Equation (1.21). The D_2 spectrum was chosen due to its uniformity, but the fits performed on H_2 data yield similarly unphysical results.. Figure 3.8(b) shows the *ab initio* fit of these data using the coverage–independent, desorption-order–independent Polanyi-Wigner equation (that is, assuming constant first order desorption, n_{des}=1). As can be seen very clearly, this *ab initio* fit is poor, and accordingly yields unphysical results for ν and E_{b}. If we relax the constraint of desorption-order–independence and make desorption-order n_{des} another parameter of the fit, we see in Figure 3.8(c) that the fit is improved. We now additionally approach more physical results for ν and E_{b}, however, while the three parameter fit matches the temperature location and width of the data, the shape profile remains different, indicating additional physics beyond that of this simple model. Additionally, it is unclear physically why the desorption of hydrogen from MOFs would obey $n_{\mathrm{des}} \approx 2$, a result usually reserved for dissociative chemical processes. The fits performed on H_2 data yield similarly unphysical results.

In this way we return to the claim that the desorption of hydrogen isotopologues from MOFs cannot be described by the first-order, coverage-independent Polanyi-Wigner equation. At this point we take it that there is enough evidence to affirm this claim, and the more general claim that the desorption of hydrogen from MOFs cannot be descirbed by the coverage-independent Polanyi-Wigner equation, regardless of desorption-order. This claim is supported by the initial-coverage–dependence of our TD spectra (Figure 3.6(a)), the unphysicality of the analysis technique described by Equation (3.1) and Figure 3.7 when applied to our TD spectra, and the poor *ab initio* fits of our TD spectra to the desorption-order–independent, coverage-independent Polanyi-Wigner equation (Figure 3.8).

Given that the desorption of hydrogen isotopologues from MOFs cannot be described with the coverage-independent Polanyi-Wigner equation, the use of many common surface science techniques for extracting the binding energy from TD spectra is ill-advised. Instead,

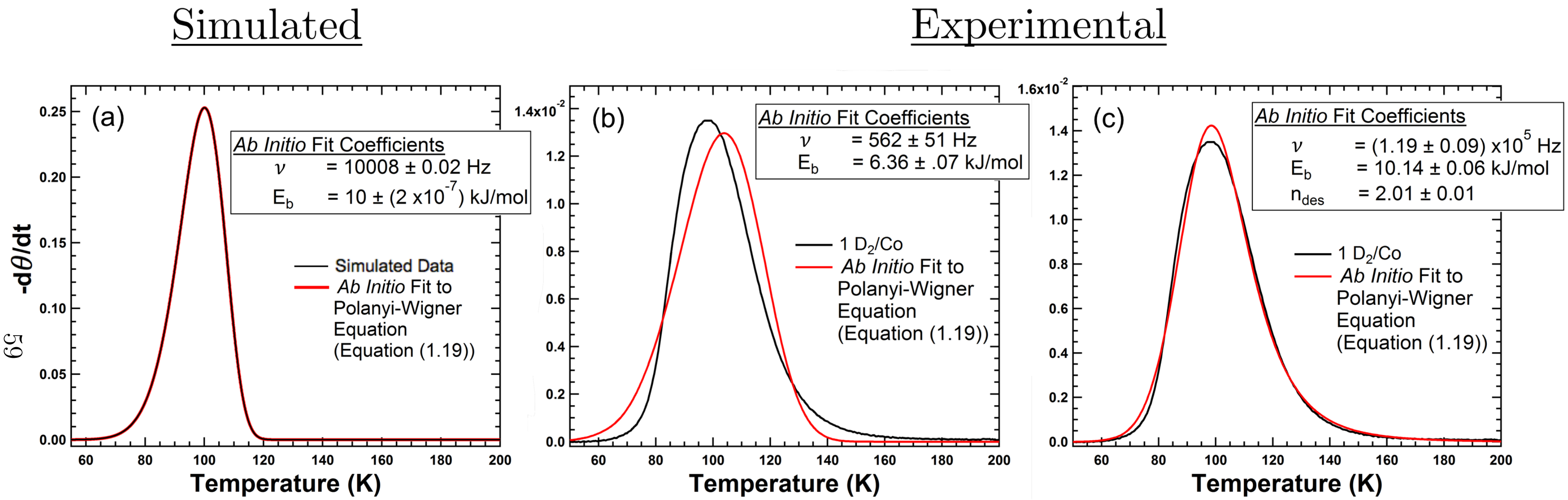

Figure 3.8: (a) *Ab initio* fit of a simulated TD spectrum with pre-exponential factor $\nu = 10000$ and binding energy $E_{\mathrm{b}} = 10$ kJ/mol to the first-order, coverage-independent Polanyi-Wigner equation. The fit correctly extracts ν and E_{b}. (b) An identical fit performed on the experimental D_2 spectrum in Figure 3.2, and (c) the same fit performed with the desorption-order n_{des} as a third fit parameter. Uncertainties reported are 1σ.

we suggest the use of isotherm analysis to extract such values of merit, as described in Ref. [60] for the MOF-74 (dobdc) series. Conveniently, as isotherm analysis consists of measuring the quantity of a particular gas adsorbed as a function of loading pressure (for a given temperature), this analysis can be performed with the same apparatus used in our TDS technique—both chiefly rely on the use of a pressure gauge at controlled temperature.

3.2 Co-MOF-74 (*m*-dobdc)

The recently synthesized MOF-74 (*m*-dobdc) series has garnered significant attention from the MOF community for its increased binding energy when compared to its structural isomers, the MOF-74 (dobdc) series [28, 61]. We again begin our analysis of this MOF with a presentation of the reproducibility of its TD spectra as acquired through our novel technique. We then report the TDS and *in situ* IR signature of the open-metal site, and again are able to resolve the difference in TD spectrum of H_2 and D_2. Consistent with Co-MOF-74 (*m*-dobdc) having a higher binding energy than Co-MOF-74 (dobdc), we observe a shift of the open-metal site TD spectra to higher temperature when compared to similar spectra for (dobdc). We further present the TDS and IR signature of (*m*-dobdc) as a function of H_2 and D_2 concentration, and comment on the site-specific information apparent. As with (dobdc), the adsorption sites in (*m*-dobdc) exhibit sequential loading of H_2 and D_2. We then perform *ab initio* fitting of the primary site TD peak to the Polanyi-Wigner equation, and report unphysical results similar to those found for (dobdc).

Figure 3.9 shows the reproducibility of our TD spectra for Co-MOF-74 (*m*-dobdc). As indicated, two spectra were taken, each at an initial concentration of $\sim$1 H_2/Co. In one spectrum an infrared source was shone on the sample during thermal desorption, and in the other this source was turned off. Again we note that our very simple TDS technique provides highly reproducible TD spectra, and that the presence of an infrared source makes a negligible difference in the peak shape and location in the TD spectrum.

In Figure 3.10 we present the TD spectrum of both H_2 and D_2 initially adsorbed onto (*m*-dobdc) at concentrations of $\sim$1 H_2/Co and $\sim$1D_2/Co. As with (dobdc), we can easily distinguish these spectra—the D_2 spectrum is clearly shifted to higher temperature than the H_2 spectrum. Given the reproducibility of our TD spectra established above, we can again be certain this effect is intrinsic to the difference in adsorption properties of H_2 and

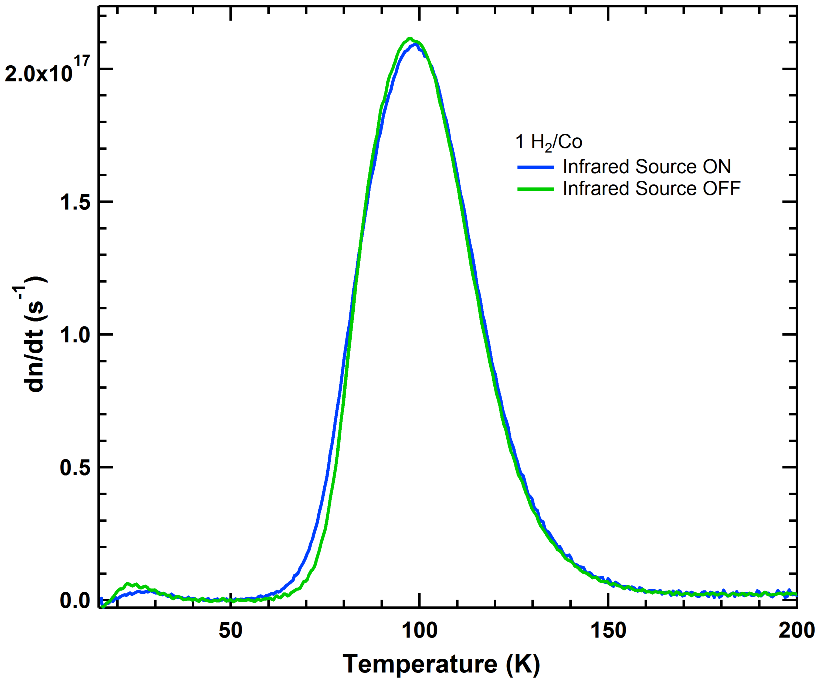

Figure 3.9: TD spectra of H_2 adsorbed onto the primary, open-metal site of Co-MOF-74 (m-dobdc) at a concentration of ∼1 H_2 per cobalt (Co). One spectrum was acquired with the infrared source of the spectrometer on, one with it off; notably, the spectra are highly reproducible and the presence of the infrared source makes a negligible difference in the TD spectrum.

D_2. We observe temperatures of maximum desorption rate of $T_{\text{max}}^{\text{H}_2} = 97 \pm 5$ K for H_2 and $T_{\text{max}}^{\text{D}_2} = 102 \pm 5$ K for D_2, where again we have supplied an overestimate of 5% for our uncertainties. The Full Width at Half Maximum (FWHM) of each peak is 34 ± 2 K, where we report an uncertainty of 7%, as before. Notably, both $T_{\text{max}}^{\text{H}_2}$ and $T_{\text{max}}^{\text{D}_2}$ are approximately 5 K higher than the corresponding T_{max} values for the TD spectra in Co-MOF-74 (dobdc). We take this shift to higher temperature to be indicative of stronger adsorption at the open-metal site, as is consistent with the literature on Co-MOF-74 (m-dobdc) [28]. This shift to higher temperature gives us confidence that our technique can not only resolve differences in TD spectrum of H_2 and D_2 for a given MOF, but can yield meaningful information on isotopologue adsorption across MOFs. With our simple TDS technique we can accurately predict the relative binding strengths of two adsorbents. We also notice that the FWHM of the TD peaks have increased from (dobdc)—this is highly significant for the prospect of

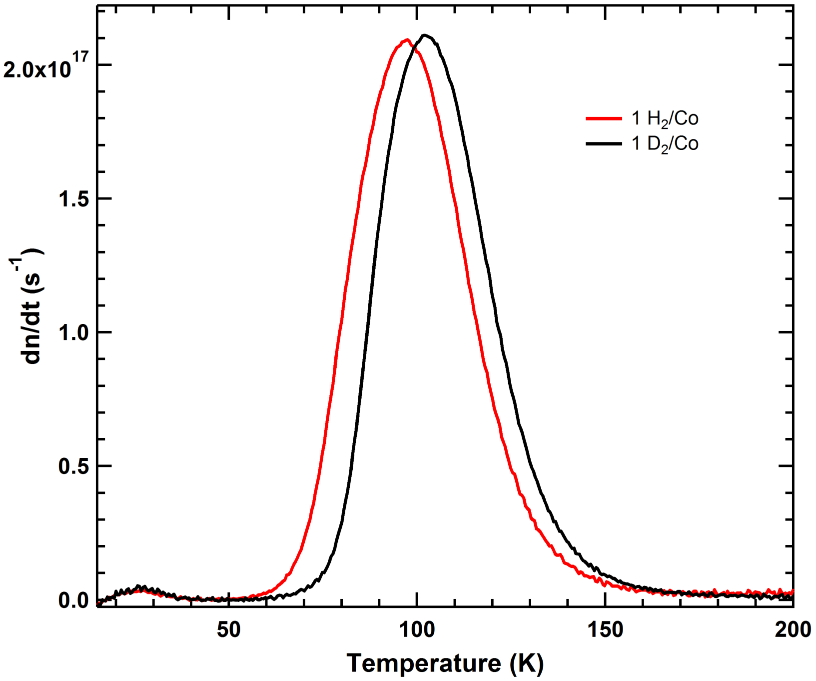

Figure 3.10: TD spectra of H_2 and D_2 adsorbed onto the primary, open-metal site of Co-MOF-74 (m-dobdc) at a concentration of ~1 H_2 (or D_2) per cobalt (Co).

temperature-programmed isotopologue separation. We discuss this effect in more detail in Section 3.4.

As with (dobdc), adsorbed D_2 is significantly less infrared active than H_2, so we focus here only on H_2 IR absorption peaks. Shown in Figure 3.11(a) is the infrared absorbance spectrum of H_2 in (m-dobdc), at a concentration of ~1 H_2/Co. This spectrum was taken at 1 cm^{-1} resolution, and is an average of 2000 scans. Following the treatment of Ref. [28], we label the overlapping peaks around 4037 cm^{-1} as Q(1) and Q(0) arising from H_2 on the primary site. As with the infrared signature of (dobdc) we observe several peaks ~200 cm^{-1} blueshifted from these fundamental vibrational Q peaks. As before we label these Q_{trans}—peaks arising from translational coupling to the Q(1) and Q(0) transitions. The separation between the vibrational peak and the corresponding translational peak represents the center of mass translational mode frequency. The presence of these IR peaks that have previously been identified in the literature as corresponding to the primary site (m-dobdc) give us confidence in labeling the TDS peaks in Figures 3.9 and 3.10 as arising due to desorption from the primary site. Figure 3.11(b) shows the *in situ* IR spectra of H_2 in the open-

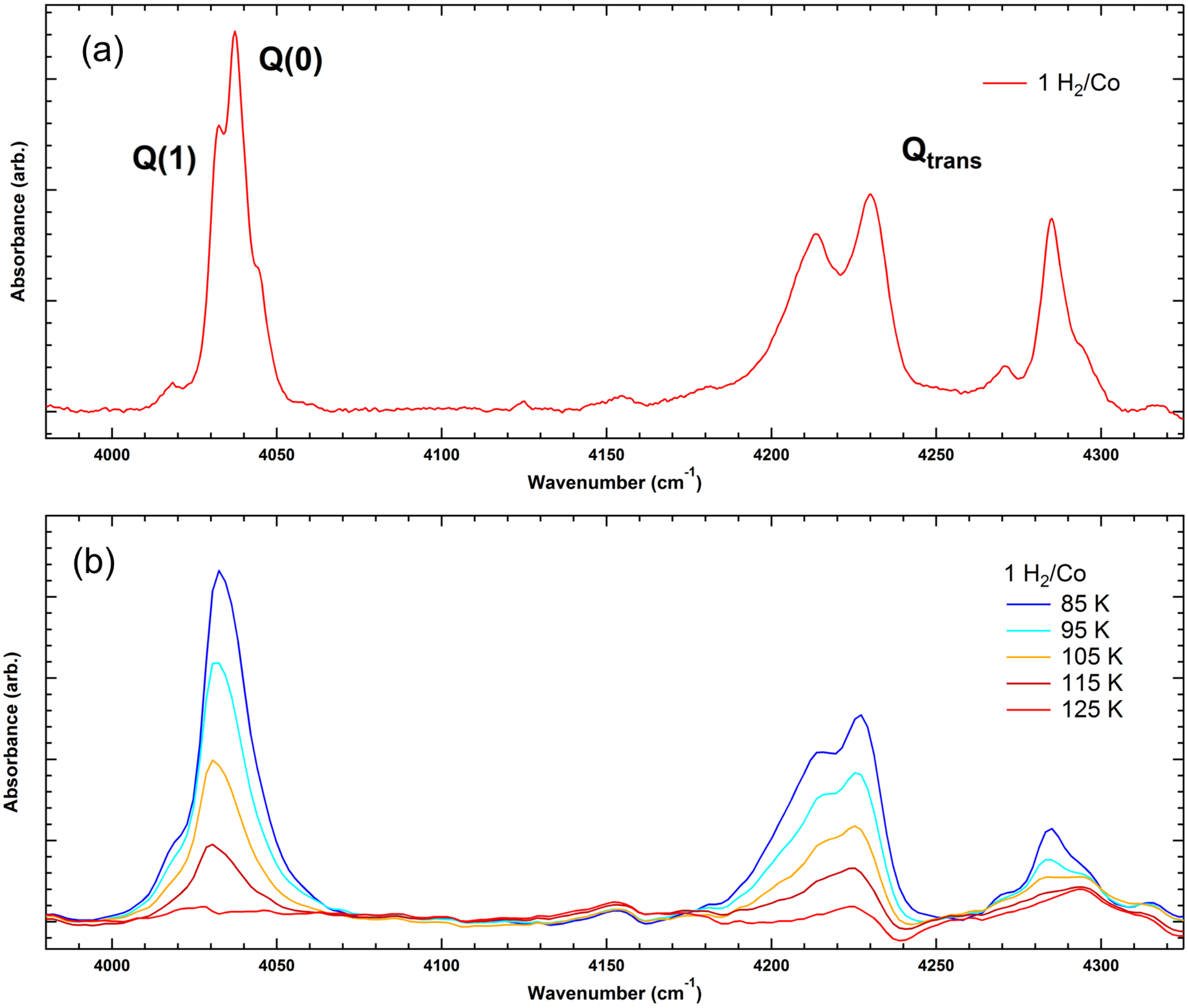

Figure 3.11: IR spectra of H_2 adsorbed onto the primary, open-metal site of Co-MOF-74 (*m*-dobdc) at an initial concentration of $\sim$1 H_2 per cobalt (Co). (a) Following the precedent set by Ref. [39] and [28], we label the Q(1) and Q(0) peaks, as well as those translational peaks resulting from these Q transitions, Q_{trans}. This spectrum was taken at 1 cm^{-1} resolution, and is an average of 2000 scans. (b) *In situ* spectra of H_2 in the open-metal site of Co-MOF-74 (dobdc) taken simultaneously with the TD spectrum shown in Figure 3.2. These spectra were taken at 4 cm^{-1} resolution, and are averages of 100 scans.

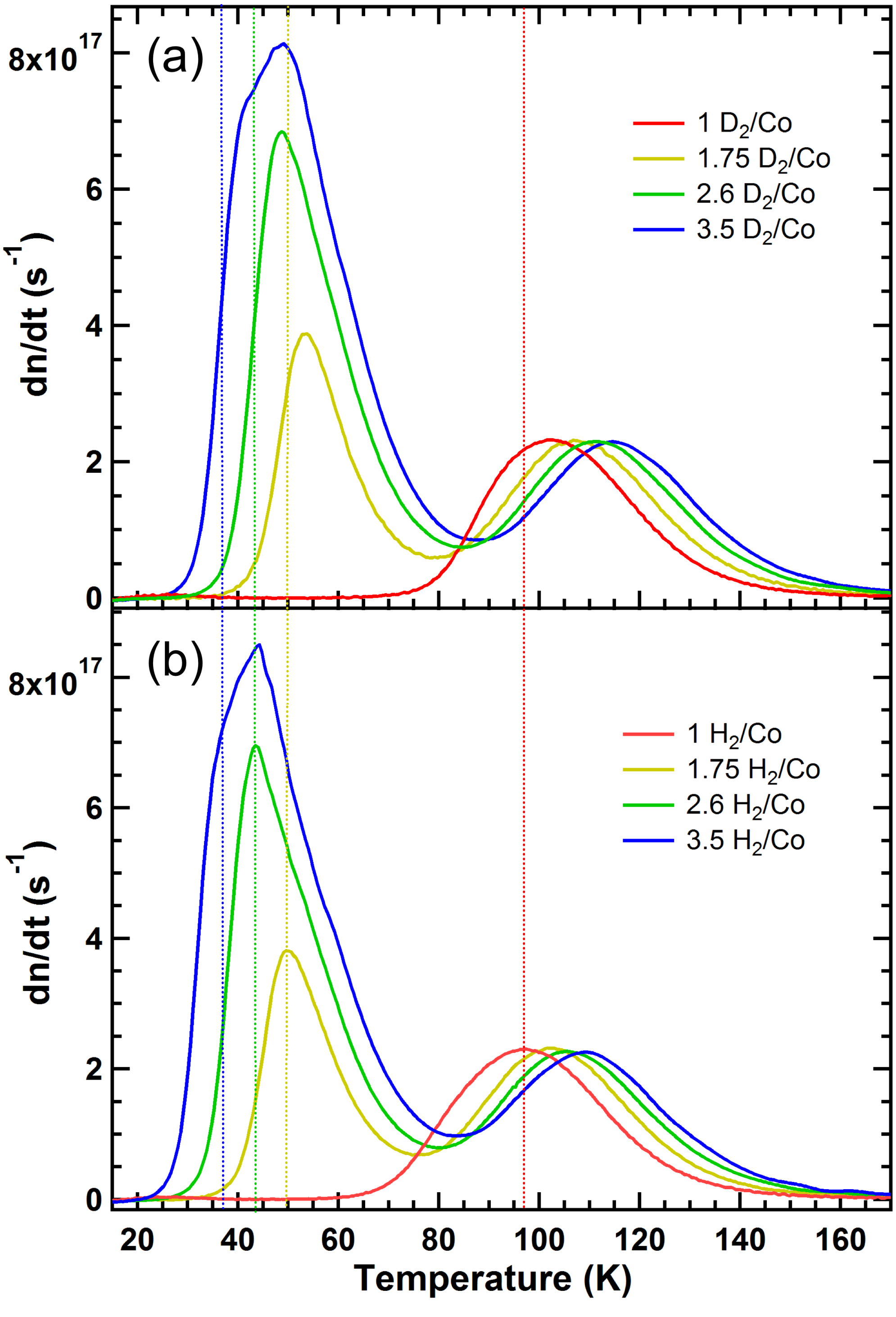

Figure 3.12: (a) TDS signature of D_2 in Co-MOF-74 (*m*-dobdc), for varying coverage. (b) An identical set of TD spectra H_2. Dotted lines are drawn to guide the eye when comparing D_2 and H_2 peaks.

metal site of (m-dobdc) taken simultaneously with the H_2 TD spectrum shown in Figure 3.10. These spectra were taken at 4 cm^{-1} resolution, and are averages of 100 scans. As before, the agreement between the TD and *in situ* IR spectra is remarkable—we observe the disappearance of the primary-site–related IR peaks at temperatures corresponding exactly to the desorption in the TD spectrum.

The TDS signature of the primary, secondary, and tertiary sites of Co-MOF-74 (m-dobdc) is shown in Figure 3.12. We observe a shift to higher temperature in all peaks when comparing H_2 to D_2, consistent with the smaller zero point energy and corresponding higher binding energy of adsorbed D_2. Similar to the tertiary peak in (dobdc), we note a shift of the secondary peak to lower temperature upon increased loading. This may indicate repulsive hydrogen–hydrogen interactions between molecules adsorbed on this site. We also notice that the tertiary TD peak is less well resolved than in (dobdc)—the tertiary peak appears to be overlapping with the secondary peak more than it was in the case of (dobdc), for both H_2 and D_2. This may indicated a lesser difference in binding energy between the tertiary and secondary sites in (m-dobdc) when compared with that difference in (dobdc). Further we are unable to resolve a distinct quaternary site in our TD spectra for either H_2 or D_2 in (m-dobdc). At higher concentrations than those shown in Figure 3.12, the central feature which we have taken as overlapping secondary and tertiary peaks simply grows. Again this may indicate a lesser difference in binding energy between the quaternary and tertiary sites in (m-dobdc) when compared with (dobdc). Similar to (dobdc) however is the apparent sequential loading of the adsorption sites in (m-dobdc). Though difficult to resolve for the tertiary and quaternary sites, we see definite evidence for hydrogen isotopologues first adsorbing onto the open-metal site, and then—only after saturating this site—adsorbing onto other sites. The amount of information that can be gleaned just from the qualitative nature of these TD spectra is remarkable, especially given the simplicity of the technique used to acquire them.

As with (dobdc), in these TD spectra we also notice an effect we attribute to readsorption. We take it that the systematic shift to higher temperature of the primary site peak upon increased loading is not the result of anything physical inside the MOF but instead is the result of readsorption. Once the system reaches a temperature such that nearly all of the hydrogen has been desorbed from the secondary, tertiary, and quaternary sites, all the spectra should be identical. All that should be recorded in the TD spectrum after this temperature is desorption from the primary site, and this desorption should be exactly the same as when

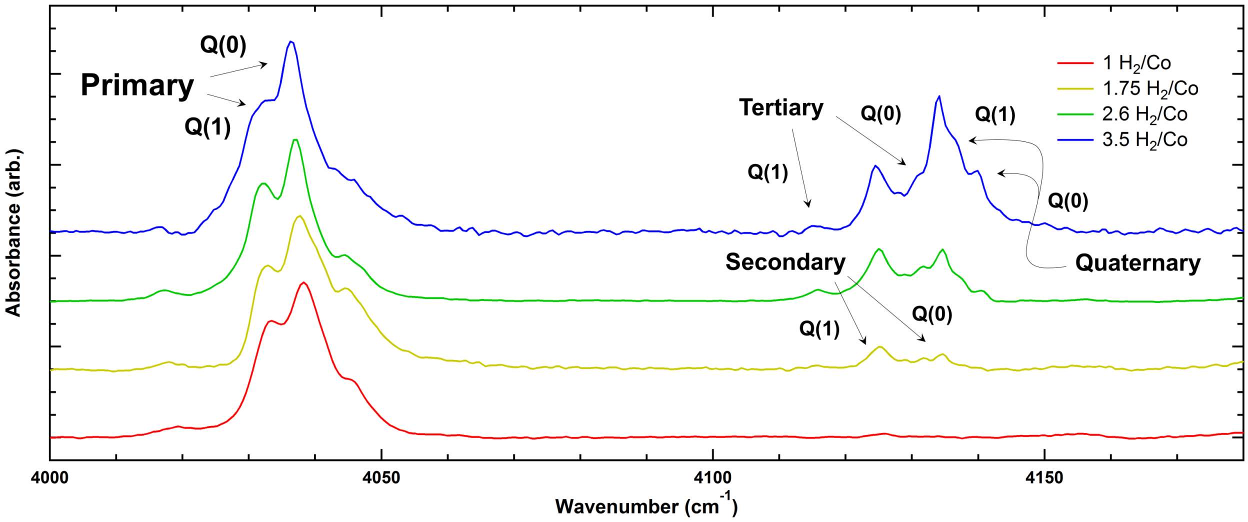

Figure 3.13: IR spectra of H_2 in Co-MOF-74 (m-dobdc) for varying concentrations. All spectra are an average of 2000 scans at resolution 1 cm^{-1}, taken at 15 K. Spectra are offset for clarity.

there was only hydrogen on the primary site to begin with. We do observe a shift in the primary site peak as the initial loading increases however. As the only systematic difference between these spectra is the initial loading, and as the likelihood of readsorption of a given molecule should increase with gaseous pressure outside the MOF, we attribute this systematic shift to readsorption. This readsorption effect does not detract from the qualitative structure of these TD spectra.

Figure 3.13 shows the IR signature of H_2 adsorbed onto the primary, secondary, tertiary, and quaternary sites of (m-dobdc). As it is a newly synthesized material, there is a relative dearth of literature on the infrared spectrum of (m-dobdc). Here we present high resolution infrared spectra of H_2 that partially fills this void. As they bear significant similarity to those IR spectra presented previously for H_2 in (dobdc), which have already been analyzed in the literature, we have a certain amount of confidence labeling the Q(1) and Q(0) peaks for the primary, secondary, tertiary, and quaternary sites as we have done. Further—and more robustly—corroborating these decisions are our TD spectra. As the IR spectra presented correspond exactly to the TD spectra in Figure 3.12(a), when peaks in the IR and TD spectrum appear for the first time simultaneously (that is, at the same concentration) we maintain that they arise from H_2 occupying a new site. Using this methodology, when we first observe a secondary peak in our TD spectra and we also observe two new peaks in the IR spectra, we are confident in our labeling these IR peaks as resulting from H_2 adsorbed onto the secondary site. Similarly, as we first observe H_2 desorption from the tertiary site in our TD spectrum, we also observe the appearance of two peaks in the corresponding IR spectrum. Accordingly, we label these IR peaks as arising due to H_2 adsorbed on the tertiary site. Though we do not see clear evidence of the quaternary site in the TDS signature of (m-dobdc), we do observe two additional peaks that arise most prominently after concentrations of 3 H_2/Co. Using the methodology we have established, we label these peaks as Q(1) and Q(0) transitions of H_2 in the quaternary site. The translational peaks shown in Figure 3.11 remain largely unchanged at these higher loadings.

The central features of the IR and TD spectra of Co-MOF-74 (m-dobdc) are summarized in Table 3.2. Again we cite an uncertainty in FTIR peak location of 1 cm^{-1}, as determined by Refs. [24, 36, 37, 51]. Here we note that the change in T_{max} between H_2 and D_2 is larger for the tertiary site than for the secondary, in contrast to what we observed in the case of (dobdc). Comparison with Table 3.1 reveals that although the modified organic ligand of (m-dobdc) leads to an increased T_{max}—and, accordingly, a speculated increased E_{b}—of H_2 adsorbed onto the primary site when compared to (dobdc), it appears that this modification has also led to a decrease in T_{max} and E_{b} of H_2 on the secondary and tertiary sites. As such, our simple technique indicates that the increase in binding energy at the primary, open-metal site in (m-dobdc) has come at the expense of the binding energies of the secondary and tertiary sites.

Further evidence that the desorption of hydrogen from MOFs cannot be accurately described by the coverage-independent Polanyi-Wigner equation is provided in Figure 3.14. Here we perform the same *ab initio* fit to the coverage-independent Polanyi-Wigner equation described in the previous section, using the experimental data from Figure 3.10. Again we perform this fit on the experimental D_2 data, in both the desorption-order–independent and –dependent regime. Just as with (dobdc), the desorption-order–independent fit is poor, and while the desorption-order–dependent fit is improved, the binding energy extracted is unphysical given the literature value of ∼11.5 kJ/mol for the binding energy of H_2 in (m-dobdc) [28]. (As we are performing the fit on D_2, we would expect a yet higher binding energy than 11.5 kJ/mol, however the fit extracts $E_{\text{b}} = 8.64 \pm 0.05$ kJ/mol.) The *ab initio* fit correctly determines the peak location and FWHM, however the shape profile remains

Isotopologue	Adsorption Site	TDS T_{max} (K)	FTIR Peak Location (cm^{-1})
H_2	Primary	97 ± 5	Q(1): 4032 ± 1 Q(0): 4037 ± 1 Q_{trans}: 4214 ± 1 4230 ± 1 4285 ± 1
	Secondary	50 ± 3*	Q(1): 4125 ± 1 Q(0): 4135 ± 1
	Tertiary	37 ± 2	Q(1): 4116 ± 1 Q(0): 4131 ± 1
	Quaternary	n/a	Q(1): 4137 ± 1 Q(0): 4141 ± 1
D_2	Primary	103 ± 5	n/a
	Secondary	53 ± 3*	n/a
	Tertiary	42 ± 2	n/a

*Peak shifts to lower temperature by ~7 K upon increased loading.

Table 3.2: Summary of TDS and FTIR peak locations for H_2 and D_2 in Co-MOF-74 (*m*-dobdc).

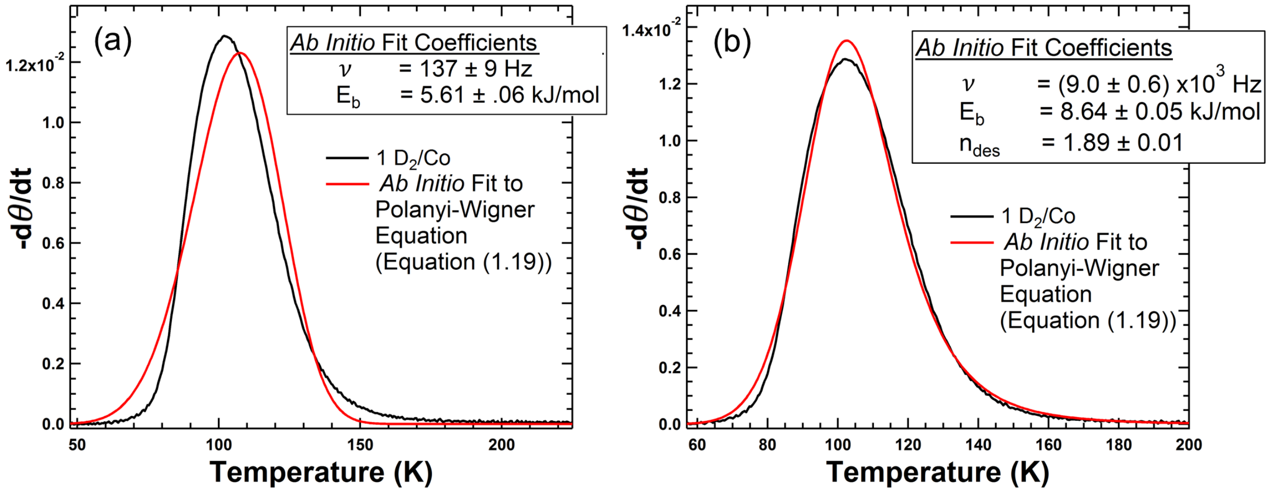

Figure 3.14: (a) *Ab initio* fit of the experimental D_2 spectrum in Figure 3.10 to the first-order, coverage-independent Polanyi-Wigner equation, and (b) the same fit performed with the desorption-order n_{des} as a third fit parameter. Uncertainties reported are 1σ.

importantly different. This indicates additional physics beyond the coverage-independent Polanyi-Wigner equation. The fits performed on H_2 data yield similarly unphysical results. This equation may be an appropriate place to start for modeling the desorption of hydrogen from MOFs, but likely some dependence of ν and E_{b} on coverage (θ) or temperature has to be determined and included in this equation to accurately model the desorption.

3.3 VSB-5

While less well-characterized and documented in the literature than Co-MOF-74 (dobdc) and (m-dobdc), VSB-5 has a significantly stronger binding energy than either of the MOFs discussed previously. This makes VSB-5 a more attractive contender for Zero Point Energy Separation (ZPES) of H_2 and D_2, though not a great amount of attention has been paid to VSB-5 in the literature since its synthesis in 2001 [30]. Here we present concentration-varying TD spectra of H_2 and D_2 in VSB-5, attained through a highly reproducible, novel TDS technique. We report the existence of two peaks in the TD signature of VSB-5, as is consistent with other TD spectra in the literature [62]. We observe a larger separation of TD spectra for H_2 and D_2 adsorbed on the primary site than observed with Co-MOF-74 (dobdc) and (m-dobdc), consistent with its having a stronger binding energy than these MOFs. We

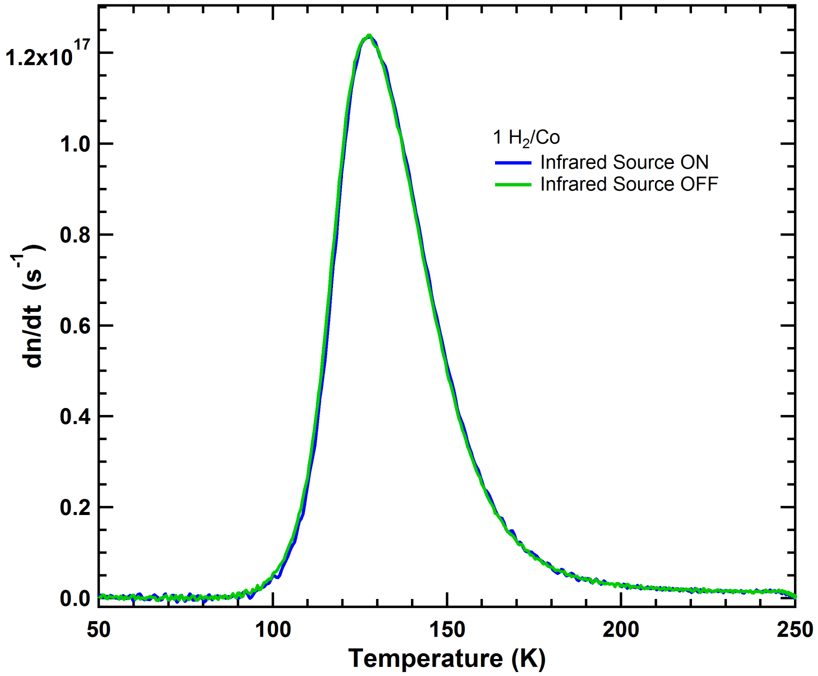

Figure 3.15: TD spectra of H_2 adsorbed onto the primary, coordinatively-unsaturated metal site of VSB-5 at a concentration of ~1 H_2 per primary site. One spectrum was acquired with the infrared source of the spectrometer on, one with it off; notably, the spectra are highly reproducible and the presence of the infrared source makes a negligible difference in the TD spectrum.

also present *in situ* IR spectra of H_2 adsorbed into VSB-5, in much the same way we reported the IR spectra of H_2 in the preceding MOFs. Finally we present further evidence that the desorption of hydrogen from VSB-5—and MOFs in general—is not captured adequately by the coverage-independent Polanyi-Wigner equation, as we report unphysical results given by *ab initio* fits of VSB-5 TD spectra to the coverage-independent Polanyi-Wigner equation.

The reproducibility of the TD spectra of hydrogen in VSB-5 is emphasized in Figure 3.15. Our novel technique again provides TD spectra with excellent reproducibility. As with the other MOFs discussed in this work, the presence of an IR source during desorption makes a negligible difference in the TD spectrum. Unlike Co-MOF-74 (dobdc) and (*m*-dobdc), there is not one primary, open-metal site per metal atom in VSB-5. As we saw in Section 1.5.3, in Figure 1.7, there are six primary sites within a single VSB-5 pore, where each pore is made up of a 24-membered ring of nickel (Ni) atoms. Filling the primary site with H_2 thus refers

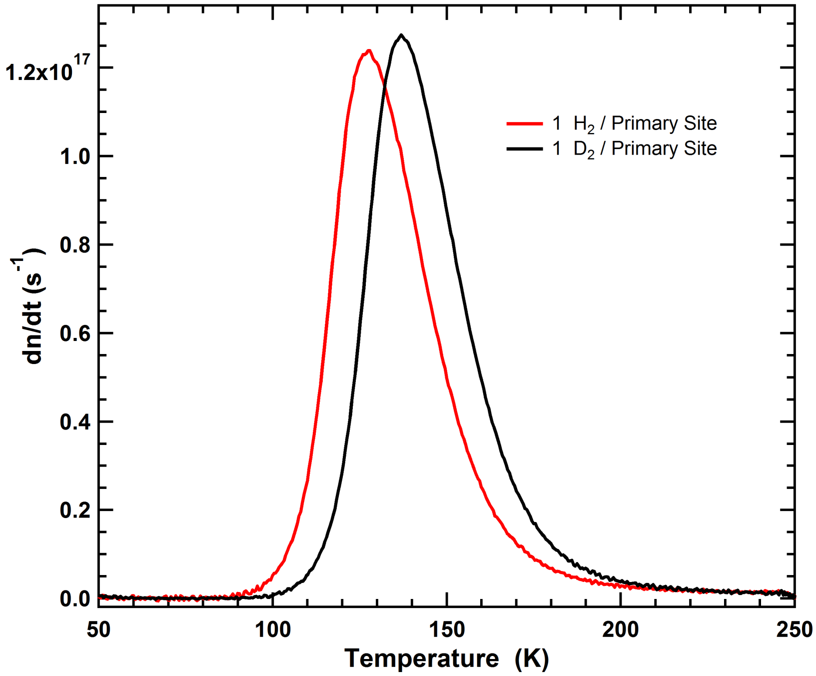

Figure 3.16: TD spectra of H_2 and D_2 adsorbed onto the primary site of VSB-5 at a concentration of ∼1 H_2 (or D_2) per primary site (0.25 H_2 or D_2 per Ni).

to an H_2-Ni concentration of 0.25 H_2/Ni. To avoid confusion on this front, we simply label full occupancy of the primary site as 1 H_2 / Primary site.

Figure 3.16 shows the TD spectra of H_2 and D_2 at this concentration of one molecule per primary site. Here we are also able to resolve the difference in H_2 and D_2. We find that although the binding energies of H_2 and D_2 are greater in VSB-5, and accordingly the difference in these binding energies is greater in VSB-5 than in Co-MOF-74, the separation of the two peaks has increased only slightly. As we report temperatures of maximum desorption rate of $T_{\mathrm{max}}^{\mathrm{H_2}} = 127 \pm 6$ K for H_2 and $T_{\mathrm{max}}^{\mathrm{D_2}} = 137 \pm 6$ K for D_2, we see that the separation between $T_{\mathrm{max}}^{\mathrm{H_2}}$ and $T_{\mathrm{max}}^{\mathrm{D_2}}$ has increased from 6 K in the case of Co-MOF-74 (dobdc) to 10 K here. The peaks, however, remain largely unseparated on account of the Full Width at Half Maximum (FWHM) of each peak, which has also increased to 46 ± 3 K. Uncertainties are tabulated as before.

The infrared signature of VSB-5 proves difficult to attain compared to those of Co-MOF-74 (dobdc) and (*m*-dobdc). The relative signal strength of adsorbed H_2 is low, perhaps contributing to why IR spectra of H_2 in VSB-5 have yet to be published. The following

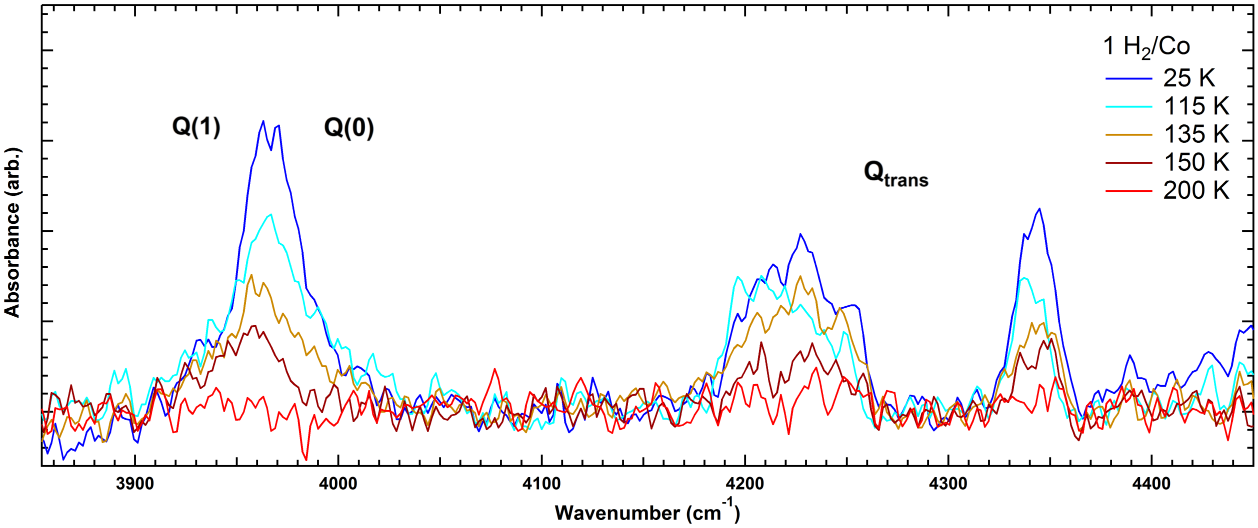

Figure 3.17: IR spectra of H_2 adsorbed onto the primary site of VSB-5 at an initial concentration of ~1 H_2 per primary site. Following the precedent set by the analysis of the previous two MOFs, we label the Q(1) and Q(0) peaks, as well as those peaks we speculate to be translational, Q_{trans}. These spectrum were taken at 4 cm^{-1} resolution, and are averages of 100 scans. These *in situ* spectra were taken simultaneously with the TD spectrum shown in Figure 3.16.

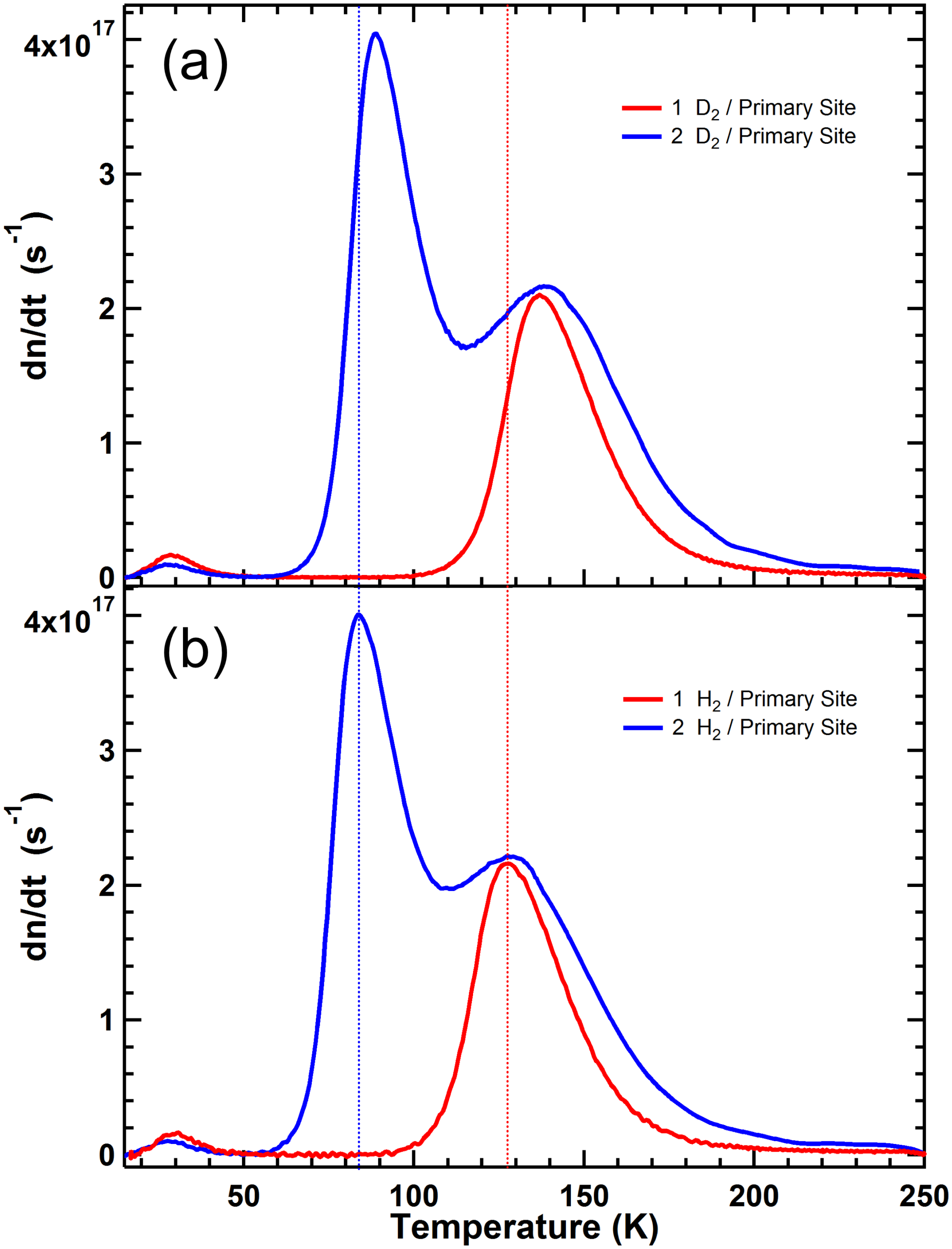

Figure 3.18: (a) TDS signature of D_2 in VSB-5, for varying coverage. (b) An identical set of TD spectra H_2. Dotted lines are drawn to guide the eye when comparing D_2 and H_2 peaks.

IR spectra are accordingly noticeably noisier than those for the preceding MOFs. Shown in Figure 3.17 are *in situ* IR spectra of H_2 in the primary site of VSB-5, taken simultaneously with the H_2 TD spectrum shown in Figure 3.16. These spectra were taken at 4 cm^{-1} resolution, and are averages of 100 scans. As before, even with the increase in noise, the agreement between the TD and *in situ* IR spectra is remarkable. We observe the disappearance of the primary-site–related IR peaks at temperatures corresponding exactly to the desorption in the TD spectrum. Following the precedent set in the analysis of the IR spectra of the previous two MOFs, we label what must be overlapping peaks around cm^{-1} as Q(1) and Q(0) arising from H_2 on the primary site. As with the previous infrared signatures, we observe several peaks $\sim$300 cm^{-1} blueshifted from these fundamental vibrational Q peaks. As before we label these Q_{trans}—peaks arising from translational coupling to the Q(1) and Q(0) transitions—though this should only be understood as a speculation, as no conclusive IR data and quantum mechanical calculations are available in the literature. If these are translational peaks, the separation between the vibrational peak and the corresponding translational peak represents center of mass translational mode frequency.

The TDS signature of the primary and secondary sites of VSB-5 is shown in Figure 3.18. We observe only two peaks in this signature, as is consistent with the literature [62]. At larger initial loadings of H_2 and D_2 we simply observe an increase in the central feature around 85 K. If there is a tertiary site in VSB-5, as reported by X-ray diffraction data [31], the binding energy of H_2 and D_2 on this site must be very close to the binding energy of these isotopologues on the secondary site. In the spectra shown, we report a shift to higher temperature in both peaks when comparing H_2 to D_2, consistent with the smaller zero point energy and corresponding higher binding energy of adsorbed D_2. This shift is lesser for the secondary peak than for the primary. Similar to Co-MOF-74, we observe sequential loading of the adsorption sites in VSB-5. Hydrogen isotopologues first adsorb onto the primary site, and then, after saturating this site, adsorb onto the secondary site. Again we note that the amount of information that can be gleaned just from the qualitative nature of these TD spectra is remarkable, especially given the simplicity of the technique used to acquire them.

Figure 3.19 shows the IR signature of H_2 adsorbed onto the primary, secondary, and what we assume is the tertiary site of VSB-5. As we have mentioned, there is a relative dearth of literature on the infrared spectrum of VSB-5, but we can use the same methodology used in the analysis of the IR spectra of the preceding MOFs to label the peaks we observe.

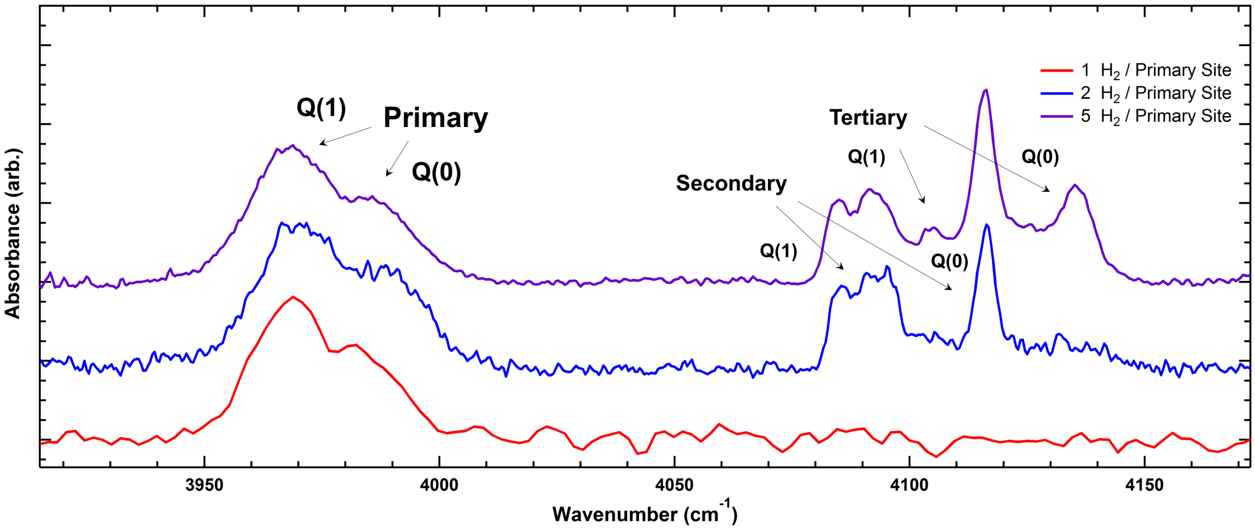

Figure 3.19: IR spectra of H_2 in VSB-5 for varying concentrations. Except for the 4 cm^{-1}, 100 scan spectrum shown in red, all spectra are an average of 1000 scans at resolution 1 cm^{-1}, taken at 15 K. Spectra are offset for clarity.

Given that they appear first, at concentrations of 1 H_2 per primary site and below, we have confidence labeling the Q(1) and Q(0) peaks for the primary site as we have done. Similarly, as they are the next to appear, we label the secondary Q(1) and Q(0) peaks. There is evidence of either splitting of the secondary Q(1) peak or high-intensity fine structure overlapping with this peak. As it is beyond the scope of this work to engage in the necessary quantum mechanical calculations to identify which peak is more likely Q(1), we simply note this as an observation. At very high H_2 concentrations we observe the presence of two more IR peaks (though no additional TD peak), which we attribute to Q(1) and Q(0) transitions of H_2 in the tertiary site. The translational peaks shown in Figure 3.17 remain largely unchanged at these higher loadings.

The central features of the IR and TD spectra of VSB-5 are summarized in Table 3.3. Uncertainties are calculated as before.

Further evidence that the desorption of hydrogen from MOFs cannot be accurately described by the coverage-independent Polanyi-Wigner equation is provided in Figure 3.20. Here we perform the same *ab initio* fit to the coverage-independent Polanyi-Wigner equation described in the previous sections, using the experimental data from Figure 3.16. We perform this fit on the experimental H_2 data, in both the desorption-order–independent and

Isotopologue	Adsorption Site	TDS T_{max} (K)	FTIR Peak Location (cm^{-1})
H_2	Primary	127 ± 6	Q(1): 3969 ± 1
			Q(0): 3985 ± 1
			Q_{trans}: 4227 ± 1
			4345 ± 1
	Secondary	83 ± 4	Q(1): 4085 ± 1 or[†] 4092 ± 1
			Q(0): 4116 ± 1
	Tertiary	n/a	Q(1): 4104 ± 1
			Q(0): 4135 ± 1
D_2	Primary	137 ± 6	n/a
	Secondary	89 ± 4	n/a
	Tertiary	n/a	n/a

[†] Two peaks, unknown which is Q(1)—see text.

Table 3.3: Summary of TDS and FTIR peak locations for H_2 and D_2 in VSB-5.

–dependent regime. Just as with Co-MOF-74, the desorption-order–independent fit is poor, and while the desorption-order–dependent fit is improved, the binding energy extracted is unphysical given the value of 16.9 kJ/mol for the binding energy, as calculated in Appendix A. (There exists no literature value for the binding energy of H_2 in VSB-5—we calculate it from isotherm analysis in Appendix A.) The *ab initio* fit correctly determines the peak location and FWHM, however the shape profile remains importantly different. This indicates additional physics beyond the coverage-independent Polanyi-Wigner equation. The fits performed on D_2 data yield similarly unphysical results. We note that in fact these fits seem to be extracting results further from physicality for VSB-5 than for Co-MOF-74. The desorption of hydrogen from MOFs may deviate further from desorption that follows the coverage-independent Polanyi-Wigner equation at higher binding energies.

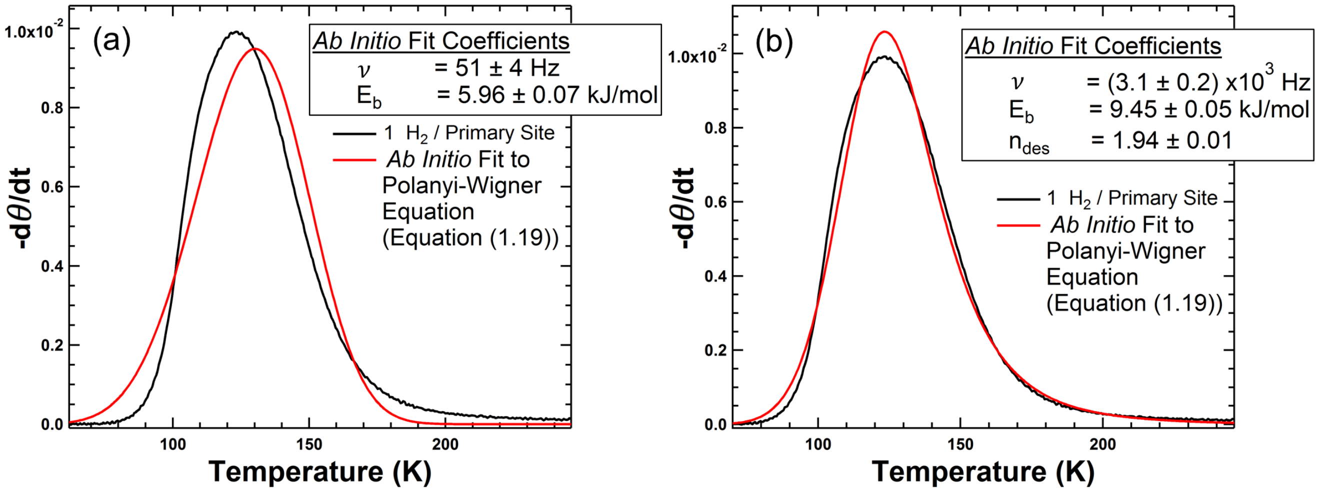

Figure 3.20: (a) *Ab initio* fit of the experimental H_2 spectrum in Figure 3.10 to the first-order, coverage-independent Polanyi-Wigner equation, and (b) the same fit performed with the desorption-order n_{des} as a third fit parameter. Uncertainties reported are 1σ.

3.4 Temperature-Programmed Separation Generally

One major result presented in this thesis is that the coverage-independent Polanyi-Wigner equation does not accurately describe desorption of H_2 or D_2 from MOFs, or at least from the representative sample of MOFs we have analyzed in this work. As we have argued at several points in this thesis, it does not adequately capture the peak shape of hydrogen desorption from MOFs, and physical binding energies are not extracted when this equation is applied to hydrogen-MOF TD spectra. We have also argued, however, that TD spectra derived from the Polanyi-Wigner equation bear resemblance to hydrogen-MOF desorption spectra in terms of peak location and width. In this way the equation serves as a fair launching point for the modeling of hydrogen desorption from MOFs. Here we take this conclusion a step further, and arrive at a second major result: Stronger binding MOFs exhibit diminishing returns with respect to the efficacy of temperature-programmed separation of hydrogen isotopologues.

This result is best demonstrated through analysis of Figure 3.21. Here we have provided four sets of simulated TD spectra, where each set contains a simulated H_2 and D_2 spectrum for varying binding energies. We calculate the binding energy of D_2 as simply 1.1 times that of H_2; this choice approximates the TD spectra we see in the MOFs considered in the

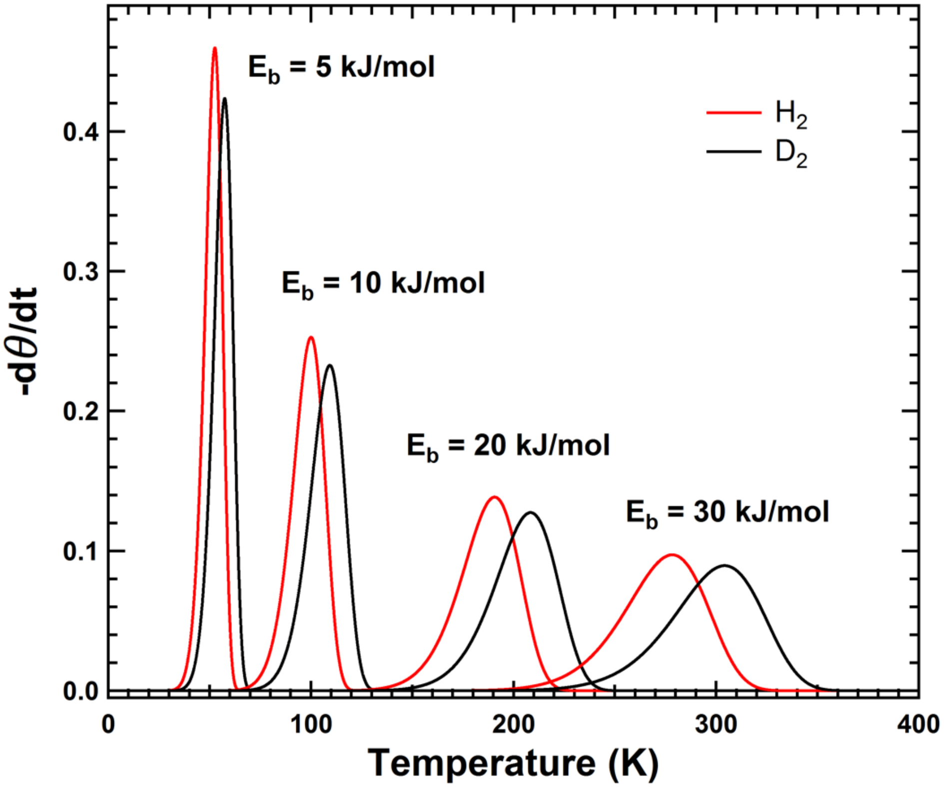

Figure 3.21: Simulated H_2 and D_2 TD spectra for varying binding energies.

previous section. As can be seen in the simulated spectra, even at H_2 binding energies as high as 30 kJ/mol the separation of the H_2 and D_2 peaks is less than ideal. As discussed in Section 1.1.1, the ultimate aim of temperature-programmed separation of H_2 and D_2 with MOFs is to find a material wherein those peaks shown are separated such that they do not overlap at all. For such a MOF, if the MOF is exposed to a mixture of H_2 and D_2, the hydrogen-MOF system can be heated to a certain temperature such that all the adsorbed H_2 desorbs, but all D_2 remains adsorbed.

We quantify the separation of these simulated H_2 and D_2 peaks in Figure 3.22, as we report the area of overlap of H_2 and D_2 spectra as a function of H_2 binding energy. Here we have normalized the overlapping area so as to be a percent, where 0% overlap refers to totally separated peaks (wherein there is zero overlapping area) and where 100% overlap refers to two identical peaks directly on top of one another. As can be seen in the inset of this figure, while the overlap area function is indeed monotonically decreasing with binding energy, it is decreasing at a rate lesser than linear. Insofar as this rate is lesser than linear,

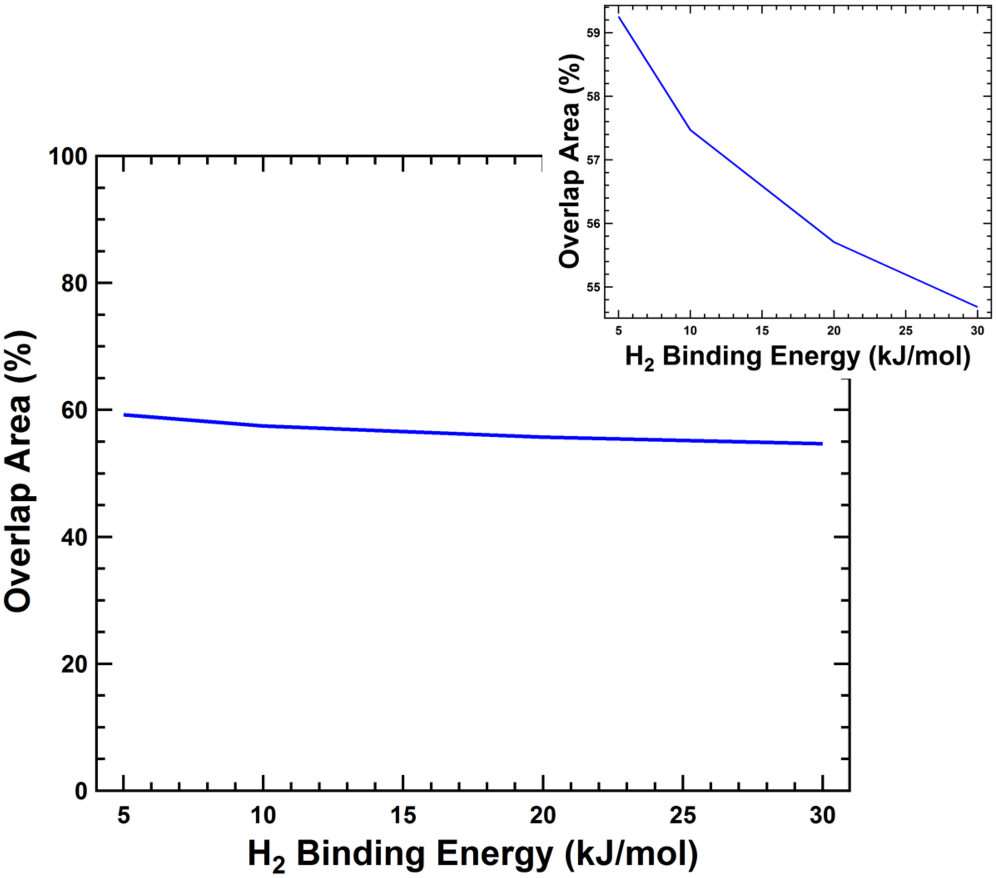

Figure 3.22: Area of overlap for simulated H_2 and D_2 TD spectra shown in Figure 3.21, as a function of H_2 binding energy.

we argue that stronger binding MOFs exhibit diminishing returns with respect to the efficacy of temperature-programmed separation of hydrogen isotopologues. This is a profound result for the prospect of temperature-programmed separation of H_2 and D_2. While there may be industrial benefit to isotopologue separation at higher temperatures—namely that the separation can be performed at temperatures less costly to reach—there is little benefit as far as the efficiency of temperature-programmed separation of H_2 and D_2 is concerned. These data suggest that in all likelihood, the initial goal of temperature-programmed separation—the separation of isotopologues by total adsorption of one isotopologue and desorption of the other at a specific temperature—will never be achieved.

This conclusion is supported by those area-overlap data for the MOFs under consideration in this thesis. In fact, the situation is exceedingly bleak from the perspective of these data.

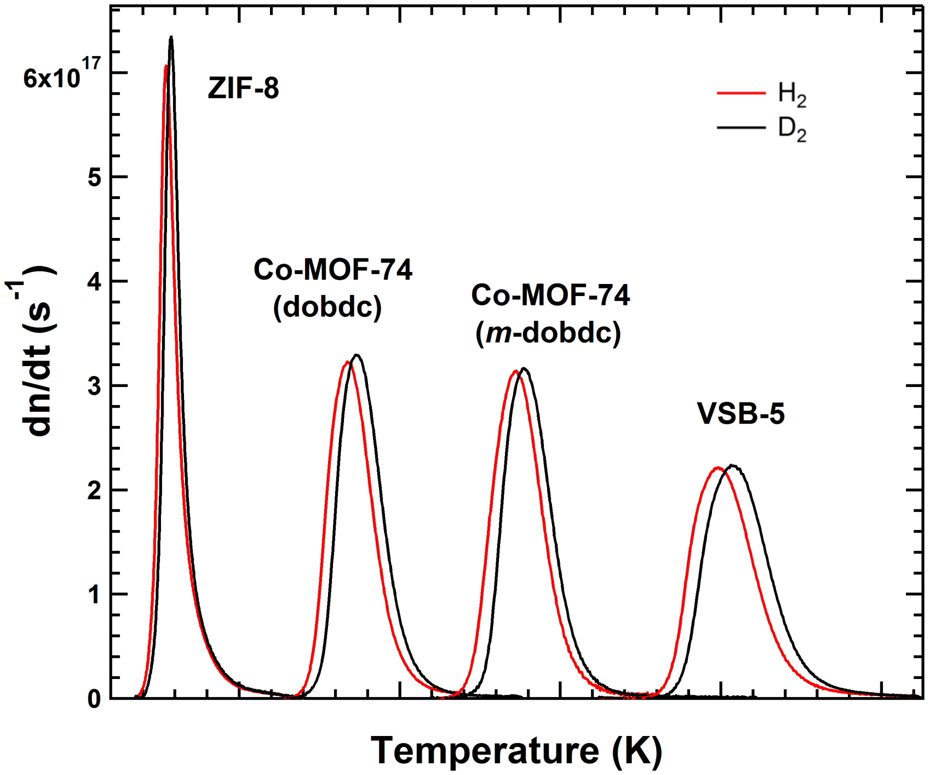

Figure 3.23: Experimental H_2 and D_2 TD spectra for the MOFs under consideration in this thesis, in addition to TD spectra of H_2 and D_2 in ZIF-8. Spectra have been offset horizontally for clarity.

Shown in Figure 3.23 are the H_2 and D_2 at concentrations of one molecule per primary site, for all the MOFs considered extensively in this thesis, as well as one not considered: ZIF-8. ZIF-8 is a zeolitic imidazolate framework with a relatively low H_2 binding energy. Its low binding energy accounts for why it was not included more prominently in this work, however here it serves the important role of providing an overlap-area datum for the low binding energy regime. More information on these TD spectra and ZIF-8 generally can be found in Appendix B. It is important to note that in Figure 3.23 the sets of spectra have been offset along the temperature axis for clarity. For an accurate sense of the temperature scale, see the individual sets of spectra in Figures B.1, 3.2, 3.10, and 3.16.

The same analysis that was performed on the simulated data is performed on these sets of experimental TD spectra. Figure 3.24 presents the area of overlap of these spectra as a function of H_2 binding energy. This figure also provides in its inset the shape of

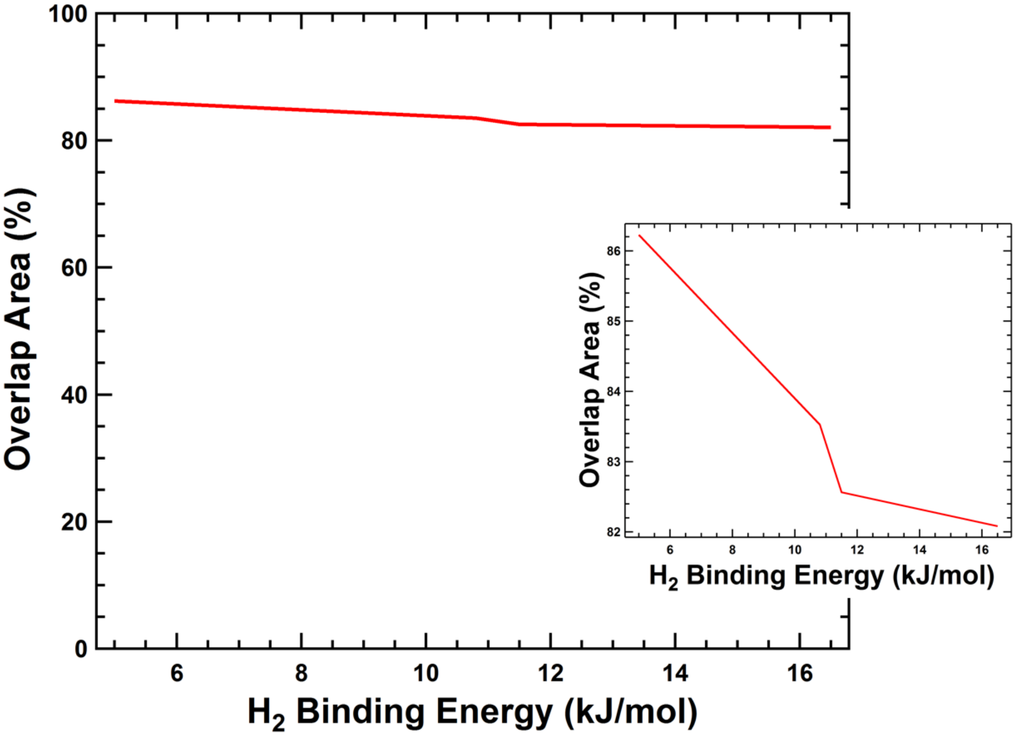

Figure 3.24: Area of overlap for experimental H_2 and D_2 TD spectra shown in Figure 3.23, as a function of H_2 binding energy.

this monotonically decreasing function. Again it appears to decrease at a rate lesser than linear, though this is debatable. Whatever the case, these experimental data cast a bleak picture for the prospects of temperature-programmed desorption. The strongest binding MOF presented in this thesis achieves an normalized area of overlap in excess of 82%. This is rather far removed from an area of overlap of zero, and the trend of the data shown in Figure 3.24 does not provide evidence that this area will go to zero on a physically realizable binding energy scale. This result is corroborated by very recent TDS data for the framework Cu(I)-MFU-4*l*, reported in Ref. [57]. Even in the case of Cu(I)-MFU-4*l*, which has a binding energy in excess of 30 kJ/mol, the separation of H_2 and D_2 TD peaks is small.

This conclusion of course does not extend to more clever uses of MOFs for isotopologue separation. If, for instance, one isotopologue could be preferentially adsorbed onto the primary site of a MOF, and another isotopologue could be adsorbed onto the secondary site, there is still a genuine possibility for temperature-programmed separation of these isotopologues. An example of this kind of separation is given in Appendix C. This conclusion and the foregoing analysis simply provides information suggesting that the most straightforward use of MOFs for temperature-programmed separation is infeasible.

Further, this result does not apply to the preferential adsorption mechanism for isotopologue separation, discussed in Section 1.1.1. Stronger binding MOFs may well posses significantly higher selectivities than weaker binding MOFs. We simply report that the temperature-programmed mechanism for isotopologue separation—a mechanism tacitly assumed to be feasible by the field at large [11–13, 46, 57, 60]—is infeasible.

Chapter 4: Conclusions and Future Work

In this thesis we provide an introduction to the use of MOFs for the separation of hydrogen isotopologues, H_2 and D_2, and for H_2 storage. We provide some background on the quantum mechanical structure of hydrogen isotopologues, the structure of a few state-of-the-art MOFs, the quantum mechanics of infrared spectroscopy, and the desorption dynamics of adsorbates generally. We provide a description of an experimental apparatus and procedure used to acquire thermal desorption (TD) and simultaneous, *in situ* infrared (IR) spectra. Notably, this apparatus makes use of a capacitive manometer pressure gauge to record TD spectra—to the best of the author's knowledge, this is the first time such an apparatus has been created and shown to produce reproducible, physically-informative TD spectra. We demonstrate the potential of this novel spectroscopic technique on three MOFs, as we report their respective TDS and IR signatures.

One dramatic result presented this thesis is the agreement between our TDS and IR techniques. This agreement is remarkable, as is the amount of information apparent in the TD spectra, and the agreement of our TD spectra with those in the literature. Given the simplicity of this TDS technique, that we are able to clearly distinguish the TD spectra of H_2 and D_2 is noteworthy. This simple technique allows for the straightforward evaluation of MOFs with respect to their isotopologue separating ability.

In addition to a proof of concept as far as the experimental apparatus is concerned, this work reports two main findings: that the desorption of hydrogen isotopologues from MOFs does not obey the coverage-independent Polanyi-Wigner equation, and that stronger binding MOFs exhibit diminishing returns with respect to the efficacy of temperature-programmed separation of these isotopologues. As we have argued on several occasions in this thesis, the TD spectra of hydrogen desorbing from the representative MOFs examined do not follow the coverage-independent Polanyi-Wigner equation; this is demonstrated by the unphysical results achieved by fitting the TD spectra of all three MOFs *ab initio* to the coverage-independent Polanyi-Wigner equation. This result is further corroborated by the initial coverage dependence of the TD spectra of Co-MOF-74 (dobdc), and by the ramp rate dependence of these spectra. As techniques based on the coverage-independent Polanyi-Wigner are being applied to MOF desorption in the literature, this result proves highly pertinent.

We arrive at the latter conclusion by examining the MOFs presented upon as a group, and examining the separation of H_2 and D_2 peaks as a function of MOF binding energy. We conclude from experimental as well as simulated data that the prospect of temperature-programmed separation through total desorption of H_2 and total adsorption of D_2 is exceedingly bleak. It is important to note that this latter conclusion affects the field broadly, as at the time of this thesis the tacit assumptions of the field with regard to the advantages of stronger binding MOFs are: (1) stronger binding MOFs allow for separation of H_2 and D_2 at higher temperatures, which are more economically feasible, (2) stronger binding MOFs possess larger separation factors and allow for more efficient separation through what we have named the preferential adsorption mechanism, and (3) stronger binding MOFs provide H_2 and D_2 TD spectra with significantly larger separations, allowing for what we deem the temperature-programmed separation mechanism. While this work does not comment on (1) and (2), we provide experimental and computational evidence that (3) is false. Accordingly, there may yet be advantages of stronger binding MOFs with regard to isotopologue separation, however (3) is not one of them, and this proves exceedingly relevant to the field at large.

The future work for this project is clear: to corroborate the novel TDS technique presented here with evacuation techniques, and to more thoroughly probe the ability and inability of this system. The first steps toward this end have already been taken, as the group has purchased a quadrupole mass spectrometer. Further, this mass spectrometer will allow for the investigation of the preferential adsorption mechanism for H_2–D_2 separation, as it can distinguish between desorbing isotopologues. Additional theoretical work directed toward modeling the coverage dependence of MOF desorption may be warranted, as may be further investigation of the fine structure of the MOF IR signatures presented here. Lastly, the recent synthesis of MOF thin films provides the opportunity for more completely investigating the coverage dependence of MOF desorption [63–65]. Further work on these novel materials may illuminate the desorption dynamics of hydrogen isotopologues in MOFs generally.

Appendix A: Isotherm Analysis of H_2 and D_2 in VSB-5

Shown in Figure A.1 are isosteric heats of adsorption of H_2 and D_2 in VSB-5, as a function of amount of H_2 or D_2 adsorbed. These heats of adsorption are derived from isotherm analysis according to the procedure documented in Refs. [28] and [60]. Isotherms were taken at temperatures in excess of 130 K, so even at the lowest loadings hydrogen may have been occupying secondary as well as primary sites. This high temperature accounts for the lack of an abrupt change in isosteric heat as secondary sites are filled. From these data we take it that the binding energies of H_2 and D_2 in the primary site of VSB-5 are 16.9(5) kJ/mol and 18.5(5) kJ/mol, respectively.

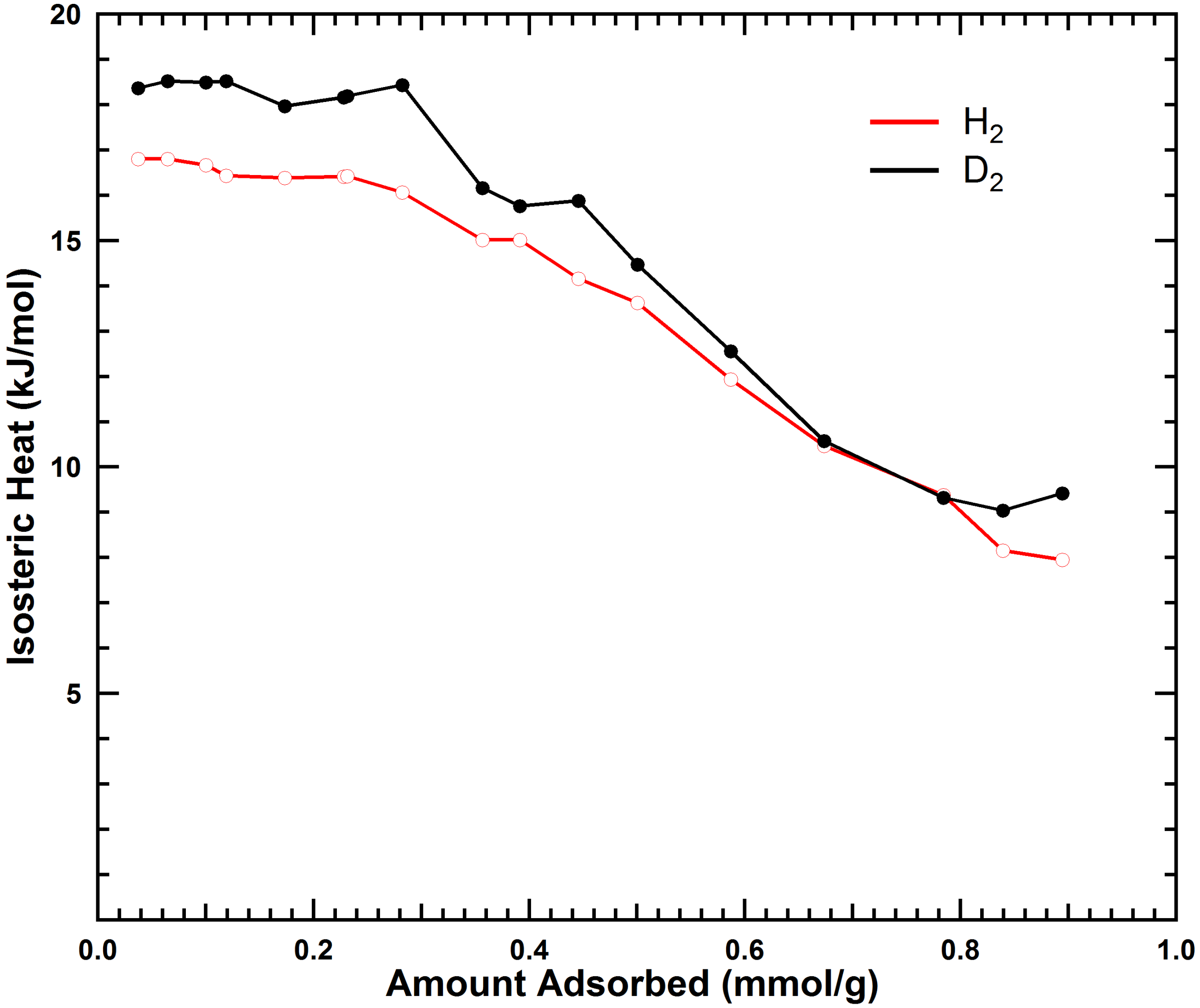

Figure A.1: Isosteric heat of adsorption for H_2 and D_2 in VSB-5 as a function of amount of H_2 or D_2 adsorbed, derived from isotherms taken at temperatures >130 K.

Appendix B: ZIF-8 TD Spectra

Figure B.1 shows the TD spectra of H_2 and D_2 adsorbed on the primary site of ZIF-8. These TD spectra were taken with a slightly different procedure than that described in Chapter 2, though the central features remain the same. A notable difference in procedure was the use of ∼6 mbar of helium exchange gas, as opposed to the ∼1 mbar used in this work—this difference accounts for the peak around 20 K, which arises from helium desorption.

ZIF-8 is a zeolitic framework without coordinatively-unsaturated open-metal sites. Accordingly it possesses a relatively low binding energy, as evidenced by its low T_{max} in Figure B.1. Information on the structure of ZIF-8 can be found in Refs. [66] and [67]. The literature reports a 4.8 kJ/mol binding energy for the primary site of ZIF-8 [67–69].

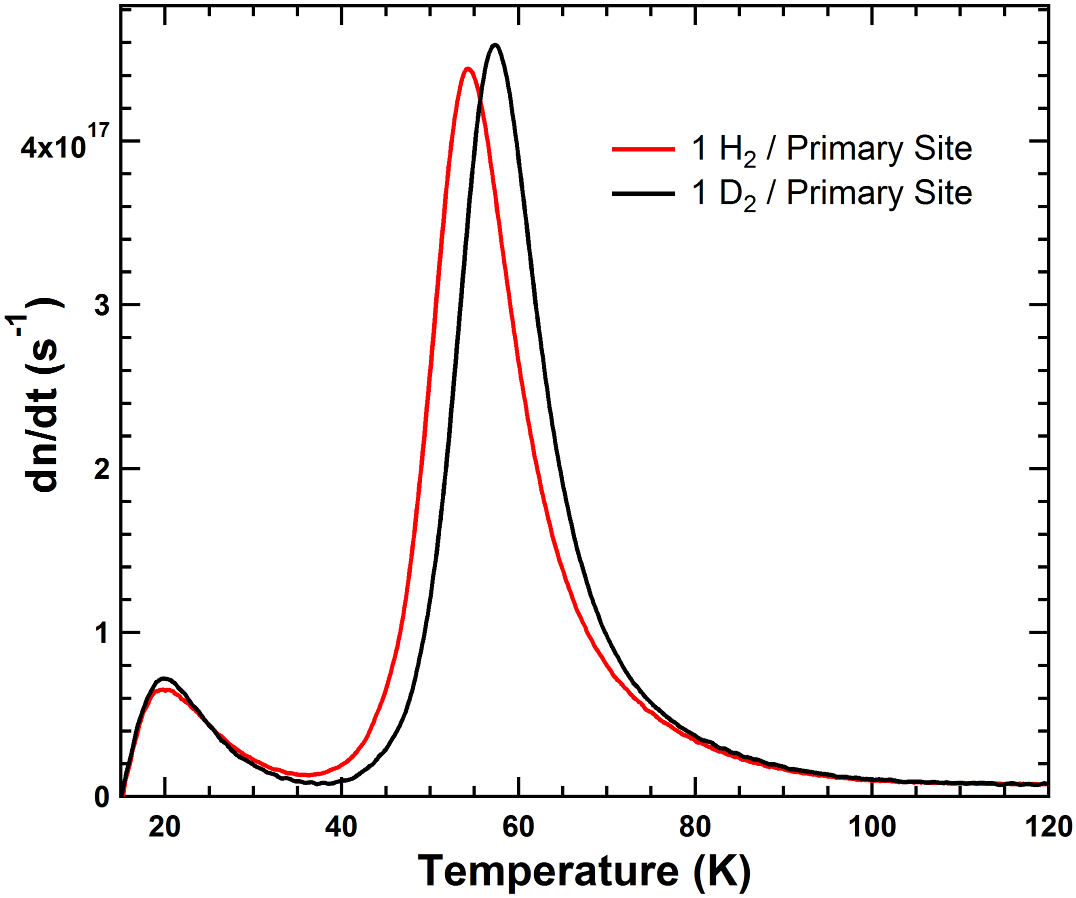

Figure B.1: TD spectra of H_2 and D_2 adsorbed onto the primary site of ZIF-8 at a concentration of ~1 H_2 (or D_2) per primary site.

Appendix C: Temperature-Programmed Separation of H_2 and N_2 in Co-MOF-74 (*m*-dobdc)

As shown in Figure C.1, Co-MOF-74 (*m*-dobdc) can quite effectively separate H_2 and molecular nitrogen, N_2. This TD spectrum was acquired by first exposing Co-MOF-74 (*m*-dobdc) powder to ∼1 N_2/Co at 150 K, ramping down to 75 K at 5 K/min, adding ∼1 H_2/Co at 75 K, and following the standard procedure described in Chapter 2. Based on its peak location and width, we identify the lowest temperature peak as arising due to H_2 on the secondary site. As the other two peaks in this spectrum were not seen in the TDS signature of H_2 in Co-MOF-74 (*m*-dobdc), we attribute them to N_2 on the primary and secondary sites.

To separate H_2 and N_2 by the temperature-programed separation mechanism, one would simply load H_2 and N_2 as we have, heat the system to 100 K to desorb the H_2, and evacuate this gaseous H_2. Our data suggests that this process would lead to near pure H_2 gas, and low impurity adsorbed-phase N_2.

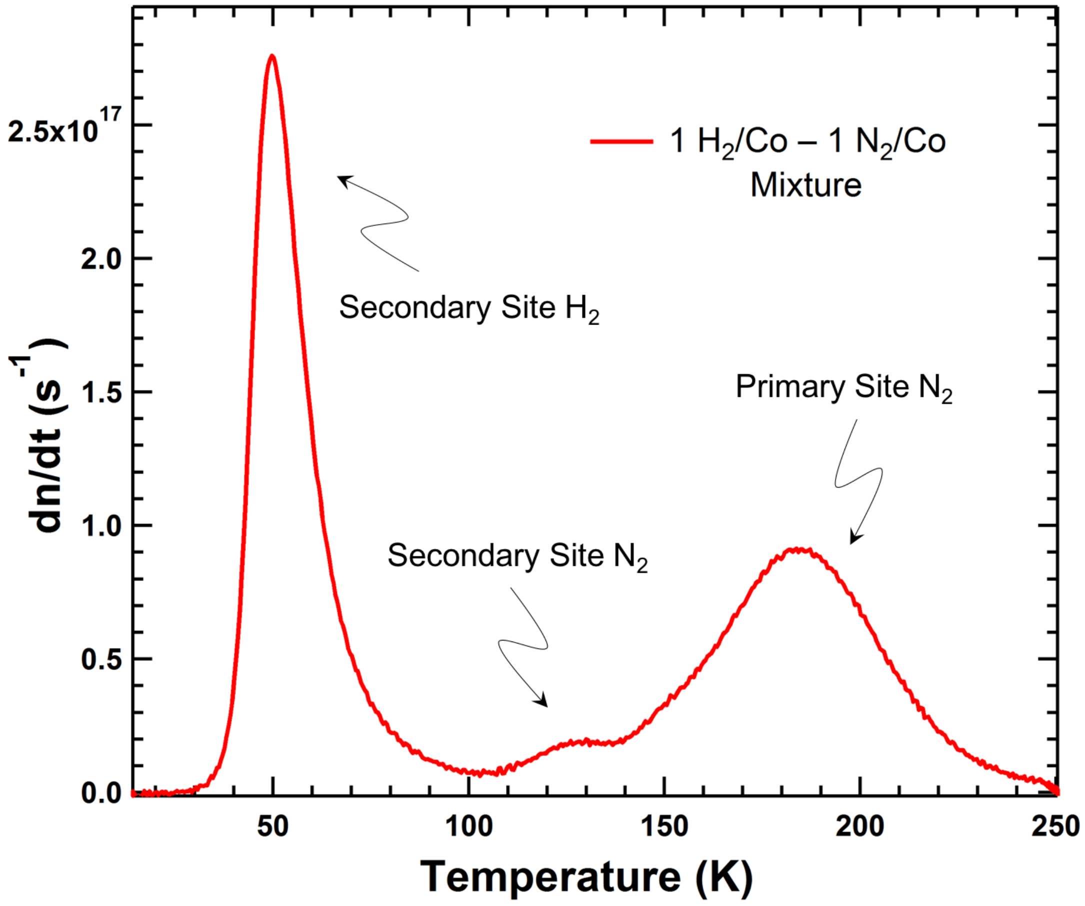

Figure C.1: TD spectrum of H_2 and N_2 adsorbed in Co-MOF-74 (*m*-dobdc) at a concentration of ∼1 H_2/Co and ∼1 N_2/Co.

Appendix D: Extracting Effective Binding Energies from Single TD Spectra

A technique of merit that does not factor in to the aims of this thesis, but which we have developed and deserves mention, concerns extracting an 'effective' binding energy from a single TD spectrum. While we have argued in this thesis that the desorption kinetics of hydrogen from MOFs on the whole does not follow the coverage-independent Polanyi-Wigner equation, we contend that the low-coverage regime of this desorption can be approximated as Arrhenian in this way, and our TDS technique accordingly allows for the extraction of an effective binding energy of the primary site of a MOF. Recall the coverage-independent Polanyi-Wigner equation:

$$r(T) = -\frac{d\theta}{dt} = \nu \ \theta^n \ e^{-E_\mathrm{b}/k_\mathrm{B}T}, \tag{D.1}$$

where r is the desorption rate of the species from the substrate, θ the fractional surface coverage of the species, t the time, ν the aptly named 'pre-exponential factor' of desorption with units of frequency, n the order of desorption, E_b the binding energy of the species to the substrate, k_B Boltzmann's constant, and T the temperature of the system. In this thesis we maintain that this form of the equation does not sufficiently capture the desorption of hydrogen from MOFs, and should instead be written with coverage- and temperature-dependent terms:

$$r(T) = -\frac{d\theta}{dt} = \nu(\theta, T) \ \theta^n \ e^{-E_\mathrm{b}(\theta,T)/k_\mathrm{B}T}. \tag{D.2}$$

An explicit form for these terms is not known, however we can still extract information on E_b for a certain coverage and temperature regime. Setting $-\frac{d\theta}{dt} = \frac{dn}{dt}/n_\mathrm{max}$, taking the natural

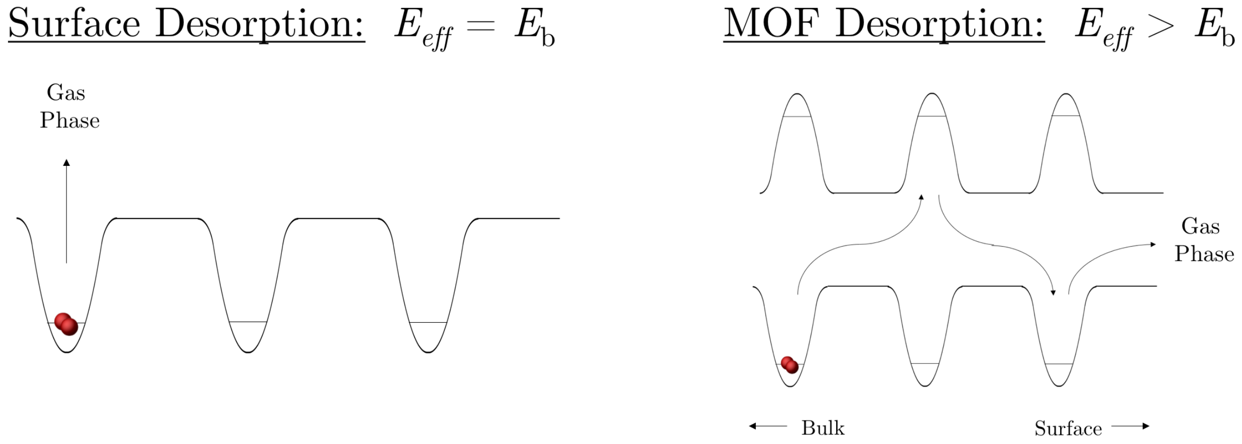
Surface Desorption: $E_{eff} = E_\mathrm{b}$

MOF Desorption: $E_{eff} > E_\mathrm{b}$

Figure D.1: Comparison of desorption from surfaces and desorption from MOFs. An H_2 molecule is shown in red, initially in the adsorbed state on a caricatured potential energy surface.

logarithm of both sides of this equation, rearranging terms, and multiplying by k_B and N_A (Avogadro's number), we find:

$$k_\mathrm{B} N_\mathrm{A} \ln\left(\frac{dn}{dt}\right) = k_\mathrm{B} N_\mathrm{A} \ln\left(n_\mathrm{max}\nu(\theta,T)\theta^n\right) - \frac{E_\mathrm{b}(\theta,T)}{T}. \tag{D.3}$$

This equation describes a linear relationship between $\ln\left(\frac{dn}{dt}\right)$ and $\frac{1}{T}$ when $\ln\left(n_\mathrm{max}\nu(\theta,T)\theta^n\right)$ is constant. As n_max and $\nu(\theta,T)$ are large, the argument of this natural logarithm is always large. The term as a whole is constant when $\nu(\theta,T)$ and θ^n are approximately constant. We contend that at low coverage, when $\theta \ll 1$, both of these terms are near to constant, and so in this regime a plot of $k_\mathrm{B} N_\mathrm{A} \ln\left(\frac{dn}{dt}\right)$ versus $\frac{1000}{T}$ should yield a straight line with slope $E_\mathrm{b}(\theta,T) \approx E_\mathrm{b}$ in units of kJ/mol. This regime describes the 'trailing edge' of a TD peak.

We note that the binding energy extracted in this way may not represent the binding energy proper, but a consistently overestimated 'effective' binding energy, E_{eff}. The reason for this is sketched in Figure D.1. Whereas in surface desorption a molecule only has to overcome the single potential well of a binding site to achieve the gas phase, in desorption from a MOF that molecule may have to travel past other, unoccupied, potential minima within a pore before reaching the gas phase. This desorption process leads to an effective binding energy that is larger than E_b.

This technique has the advantage that it can be performed on a single TD spectrum.

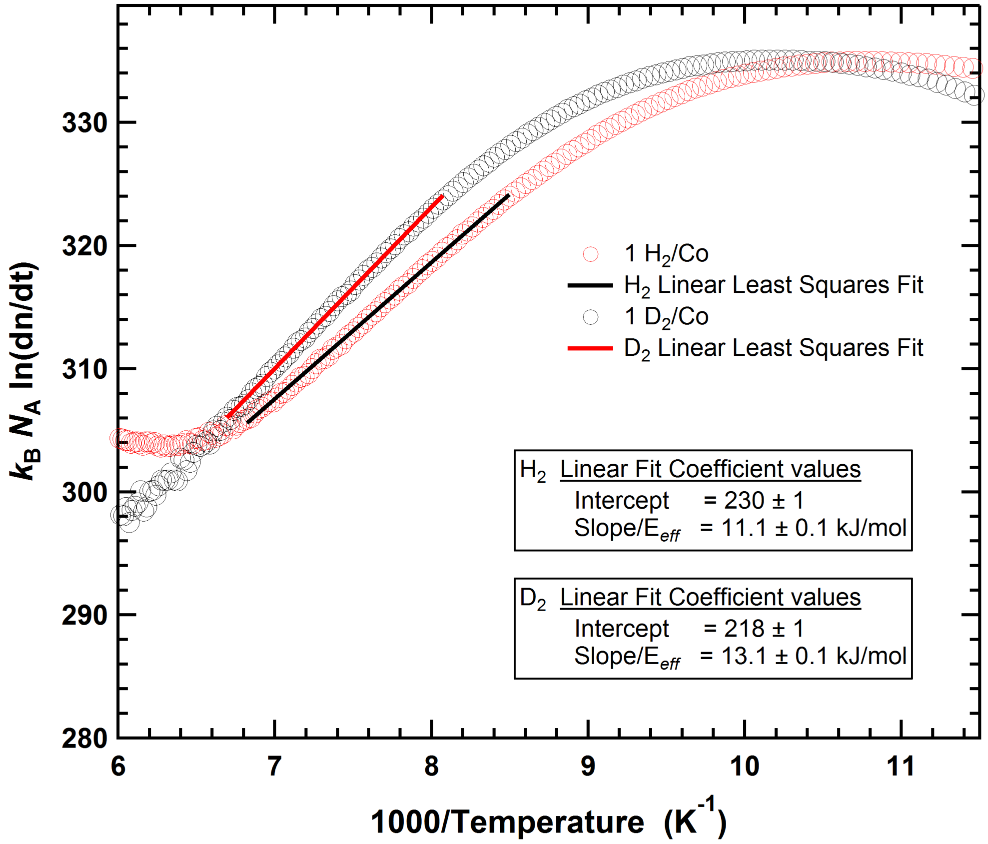

Figure D.2: Extraction of the effective binding energy, E_{eff}, of Co-MOF-74 (dobdc). Uncertainty in data points are smaller than the markers. Uncertainty given in the linear fit coefficients is 1σ.

In Figures D.2, D.3, and D.4, we perform the manipulations described above on H_2 and D_2 spectra at concentrations of 1 molecule per primary site, for Co-MOF-74 (dobdc), Co-MOF-74 (m-dobdc), and VSB-5, respectively. As reported in the figures, this technique consistently extracts a higher binding energy for D_2 spectra than for H_2, and these binding energies are consistently overestimated by around 10% percent when compared to the literature values quoted in Chapter 3.

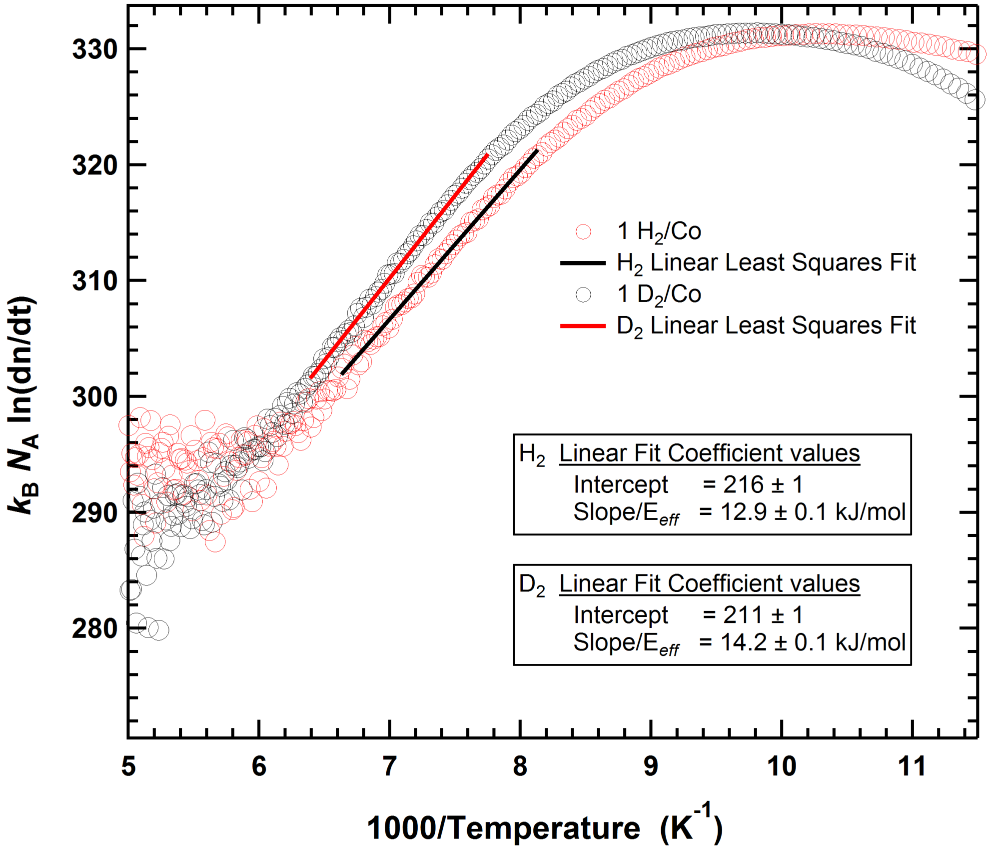

Figure D.3: Extraction of the effective binding energy, E_{eff}, of Co-MOF-74 (m-dobdc). Uncertainty in data points are smaller than the markers. Uncertainty given in the linear fit coefficients is 1σ.

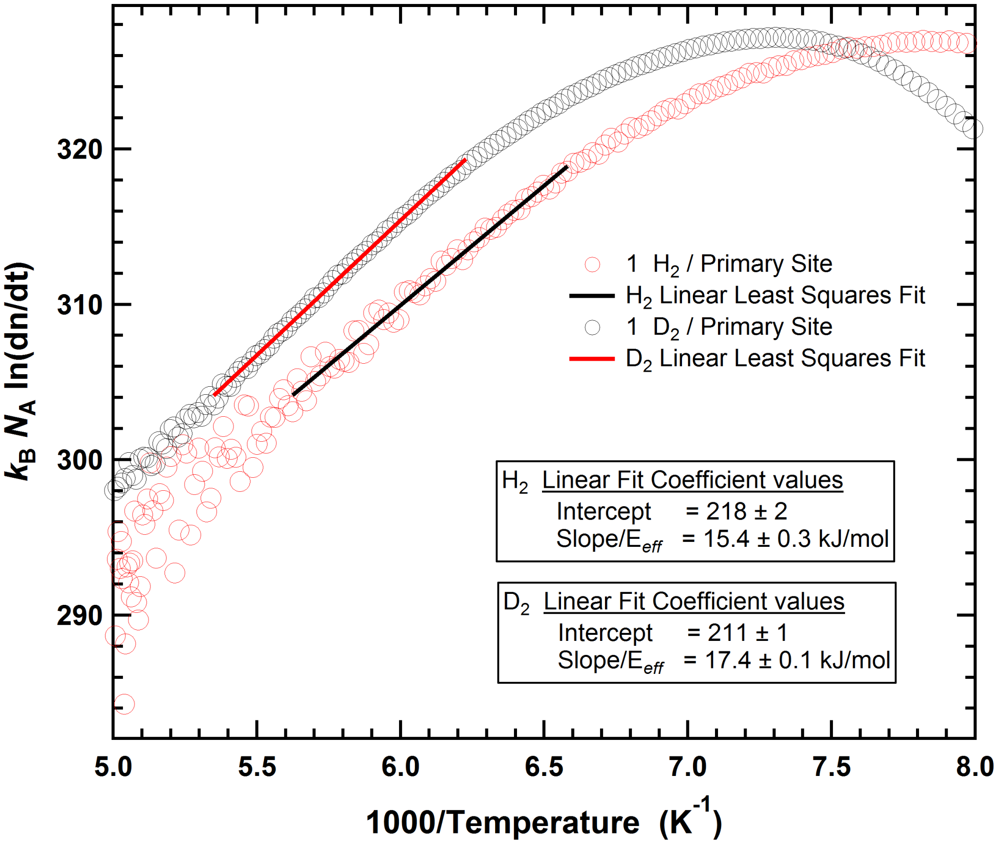

Figure D.4: Extraction of the effective binding energy, E_{eff}, of VSB-5. Uncertainty in data points are smaller than the markers. Uncertainty given in the linear fit coefficients is 1σ.

Acknowledgments

I would like to personally acknowledge the following people, without whom this work would not have been possible:

Of course, my advisor, Stephen FitzGerald—for his teaching, mentorship, and heroic editorial work, I am deeply thankful.

For her help in taking much of the data presented in this thesis, I would like to thank Katie Rigdon.

For their help acquiring thermal desorption data on ZIF-8, I would like to thank Daniel Mukasa, Enrico Milletti, and Josh Parker.

For his lionhearted soldering of the impossibly thin silicon diode thermometer wires, I thank Bill Mohler.

For their support, encouragement, and camaraderie, I thank the rest of my peers in the Physics department.

Bibliography

[1] S. F. Lincoln, “Fossil Fuels in the 21st Century,” *Ambio*, vol. 14, pp. 621–627, 2005.

[2] M. S. Dresselhaus and I. L. Thomas, “Alternative Energy Technologies,” *Nature*, vol. 414, pp. 332–337, 2001.

[3] United States Department of Energy, Office of Science, *Basic Research Needs for the Hydrogen Economy*, 2004. `https://science.energy.gov/~/media/bes/pdf/reports/files/Basic_Research_Needs_for_the_Hydrogen_Economy_rpt.pdf`.

[4] United States Department of Energy, Fuel Cell Technologies Program, *The Department of Energy Hydrogen and Fuel Cells Program Plan*, 2011. `https://www.hydrogen.energy.gov/pdfs/program_plan2011.pdf`.

[5] R. J. Press, K. S. V. Santhanam, M. J. Miri, A. V. Bailey, and G. A. Takacs, *Introduction to Hydrogen Technology.* John Wiley & Sons, 2009.

[6] A. I. Miller, “Heavy Water: A Manufacturers’ Guide for the Hydrogen Century,” *Canadian Nuclear Society Bulletin*, vol. 22, no. 1, 2001.

[7] R. D. Tung, “The Development of Deuterium-Containing Drugs,” *Innovations in Pharmaceutical Technology*, 2010.

[8] S. L. Harbeson and R. D. Tung, “Deuterium Medicinal Chemistry: A New Approach to Drug Discovery and Development,” *MedChem News*, no. 2, pp. 8–22, 2014.

[9] J.-R. Li, R. J. Kuppler, and H.-C. Zhou, “Selective Gas Adsorption and Separation in Metal-Organic Frameworks,” *Chem. Soc. Rev.*, vol. 38, pp. 1477–1504, 2009.

[10] J. L. C. Rowsell and O. M. Yaghi, "Metal-Organic Frameworks: A New Class of Porous Materials," *Microporous and Mesoporous Materials*, vol. 73, pp. 3–14, 2004.

[11] H. Oh, I. Savchenko, A. Mavrandonakis, T. Heine, and M. Hirscher, "Highly Effective Hydrogen Isotope Separation in Nanoporous Metal-Organic Frameworks with Open Metal Sites: Direct Measurement and Theoretical Analysis," *ACS Nano*, vol. 8, no. 1, pp. 761–770, 2014.

[12] H. Oh and M. Hirscher, "Quantum Sieving for Separation of Hydrogen Isotopes Using MOFs," *Eur. J. of Inorg. Chem.*, vol. 2016, pp. 4265–4529, 2016.

[13] I. Savchenko, *Exploiting Nuclear Quantum Effects for Hydrogen Isotopologues Separation in Metal-Organic Frameworks*. PhD thesis, Jacobs University, 2016.

[14] J. J. M. Beenakker, V. D. Borman, and S. Y. Krylov, "Molecular Transport in Subnanometer Pores: Zero-Point Energy, Reduced Dimensionality and Quantum Sieving," *Chem. Phys. Lett.*, vol. 232, pp. 379–382, 1995.

[15] D. J. Griffiths, *Introduction to Quantum Mechanics*. Pearson, 2 ed., 2005.

[16] United States Department of Energy, Office of Energy Efficiency & Renewable Energy. Alternative Fuels Data Center, "Alternative Fueling Station Counts by State," 2017. `http://www.afdc.energy.gov/fuels/stations_counts.html`.

[17] United States Department of Energy, Office of Energy Efficiency & Renewable Energy, *Fuel Cell Technologies Market Report 2015*, 2015. `https://energy.gov/sites/prod/files/2016/10/f33/fcto_2015_market_report.pdf`.

[18] United States Department of Energy, Office of Energy Efficiency & Renewable Energy, *Multi-Year Research, Development, and Demonstration Plan*, 2012. `https://energy.gov/eere/fuelcells/downloads/fuel-cell-technologies-office-multi-year-research-development-and-22`.

[19] I. Barin, *Thermochemical Data of Pure Substances*, vol. 1. VCH, 3 ed., 1995.

[20] S. K. Bhatia and A. L. Myers, "Optimum Conditions for Adsorptive Storage," *Langmuir*, vol. 22, pp. 1688–1700, 2006.

[21] C. O. Areán, S. Chavan, C. P. Cabello, E. Garrone, and G. T. Palomino, “Thermodynamics of Hydrogen Adsorption on Metal-Organic Frameworks,” *ChemPhysChem*, vol. 11, pp. 3237–3242, 2010.

[22] Y. Liu, H. Kabbour, C. M. Brown, D. A. Neumann, and C. C. Ahn, “Increasing the Density of Adsorbed Hydrogen with Coordinatively Unsaturated Metal Centers in Metal-Organic Frameworks,” *Langmuir*, vol. 24, pp. 4772–4777, 2008.

[23] H. Wu, W. Zhou, and T. Yildirim, “High-Capacity Methane Storage in Metal-Organic Frameworks M_2(dhtp): The Important Role of Open Metal Sites,” *J. Am. Chem. Soc.*, vol. 131, pp. 4995–5000, 2009.

[24] S. A. FitzGerald, T. Yildirim, L. J. Santodonato, D. A. Neumann, J. R. D. Copley, and J. J. Rush, “Quantum Dynamics of Interstitial H_2 in solid C_{60},” *Phys. Rev. B*, vol. 60, no. 6439, 1999.

[25] I. F. Silvera, “The Solid Molecular Hydrogens in the Condensed Phase: Fundamentals and Static Properties,” *Rev. Mod. Phys.*, vol. 52, no. 2, p. 383, 1980.

[26] E. Ilisca and F. Ghiglieno, “Nuclear Conversion Theory: Molecular Hydrogen in Non-Magnetic Insulators,” *R. Soc. Open Sci.*, vol. 3, no. 9, 2016.

[27] N. Rosi, J. Kim, M. Eddaoudi, B. Chen, M. O’Keeffe, and O. M. Yaghi, “Rod Packings and Metal-Organic Frameworks Constructed from Rod-Shaped Secondary Building Units,” *J. Am. Chem. Soc.*, vol. 127, pp. 1504–1518, 2005.

[28] M. T. Kapelewski, S. J. Geier, M. R. Hudson, D. Stück, J. A. Mason, J. N. Nelson, D. J. Xiao, Z. Hulvey, E. Gilmour, S. A. FitzGerald, M. Head-Gordon, C. M. Brown, and J. R. Long, “M_2(*m*-dobdc) (M = Mg, Mn, Fe, Co, Ni) Metal-Organic Frameworks Exhibiting Increased Charge Density and Enhanced H_2 Binding at the Open Metal Sites,” *J. Am. Chem. Soc.*, vol. 136, pp. 12119–12129, 2014.

[29] N. Nijem, L. Kong, Y. Zhao, H. Wu, J. Li, D. C. Langreth, and Y. J. Chabal, “Spectroscopic Evidence for the Influence of the Benzene Sites on Tightly Bound H_2 in Metal-Organic Frameworks with Unsaturated Metal Centers: MOF-74-Cobalt,” *J. Am. Chem. Soc.*, vol. 133, pp. 4782–4784, 2011.

[30] N. Guillou, Q. Gao, P. M. Forster, J.-S. Chang, M. Noguès, S.-E. Park, G. Férey, and A. K. Cheetham, “Nickel(II) Phosphate VSB-5: A Magnetic Nanoporous Hydrogenation Catalyst with 24-Ring Tunnels,” *Angew. Chem. Int. Ed.*, vol. 113, no. 15, pp. 2831–2834, 2001.

[31] N. Guillou, P. M. Forster, Q. Gao, A. K. Cheetham, and G. Férey, “*Ab Initio* Crystal Structure Determination and Thermal Behavior of a Large-Pore, 24-Membered Ring, Zeolitic Nickel(II) Phosphate, VSB-5,” *Materials Science Forum*, vol. 378, pp. 576–581, 2001.

[32] P. R. Griffiths and J. A. de Haseth, *Fourier Transform Infrared Spectrometry.* Wiley-Interscience Publication, 1986.

[33] E. Moore, ed., *Fourier Transform Infrared Spectroscopy (FTIR): Methods, Analysis, and Research Insights.* Nova Science, 2017.

[34] D. B. Chase and J. F. Rabolt, *Fourier Transform Raman Spectroscopy.* Academic Press, 1994.

[35] W. W. Wendlandt and H. G. Hecht, *Reflectance Spectroscopy.* Interscience Publishers, 1966.

[36] C. Simmons, “The Quantum Dynamics of H_2 in a C_{60} Lattice,” Oberlin College Honors Thesis, 2005.

[37] H. Churchill, “Low Temperature Infrared Spectroscopy of H_2 in solid C_{60},” Oberlin College Honors Thesis, 2006.

[38] L. Wolniewicz, “Nonadiabatic Energies of the Ground State of the Hydrogen Molecule,” *J. Chem. Phys.*, vol. 103, pp. 1792–1799, 1995.

[39] S. A. FitzGerald, B. Burkholder, M. Friedman, J. B. Hopkins, C. J. Pierce, J. M. Schloss, B. Thompson, and J. L. C. Rowsell, “Metal-Specific Interactions of H_2 Adsorbed within Isostructural Metal-Organic Frameworks,” *J. Am. Chem. Soc*, vol. 133, pp. 20310–20318, 2011.

[40] L. Kong, G. Román-Pérez, J. M. Soler, and D. C. Langreth, "Energetics and Dynamics of H_2 Adsorbed in a Nanoporous Material at Low Temperature," *Phys. Rev. Lett.*, vol. 103, 2009.

[41] H. Hamaguchi, A. D. Buckingham, and W. J. Jones, "Determination of Derivatives of the Polarizability Anisotropy in Diatomic Molecules: 2. The Hydrogen and Nitrogen Molecules," *Mol. Phys.*, vol. 43, pp. 1311–1319, 1981.

[42] K. Rosnow, "Solving for Eigenvalues and Eigenstates of a MOF-5 Potential," Oberlin College Honors Thesis, 2017. Manuscript in Progress.

[43] Z. Zhao, S. Wang, Y. Yang, X. Li, J. Li, and Z. Li, "Competitive Adsorption and Selectivity of Benzene and Water Vapor on the Microporous Metal Organic Frameworks (HKUST-1)," *Chemical Engineering Journal*, vol. 259, pp. 79–89, 2015.

[44] Z. Chen, D. Zhou, T. Gao, W. Shen, X. Dong, S. Naito, L. Qin, and Y. Huang, "Unusual Adsorption and Desorption behaviors of NO and Co on Nanoporous Nickel Phosphate VSB-5: In situ FT-IR and TPD Study," *Catalysis Today*, vol. 258, pp. 199–204, 2015.

[45] B. Panella, M. Hirscher, and B. Ludescher, "Low-Temperature Thermal-Desorption Mass Spectroscopy Applied to Investigate the Hydrogen Adsorption on Porous Materials," *Microporous and Mesoporous Materials*, vol. 103, pp. 230–234, 2007.

[46] B. Panella, K. Hönes, U. Müller, N. Trukhan, M. Schubert, H. Pütter, and M. Hirscher, "Desorption Studies of Hydrogen in Metal-Organic Frameworks," *Angew. Chem. Int. Ed.*, vol. 47, pp. 2138–2142, 2008.

[47] F. von Zeppelin, M. Haluška, and M. Hirscher, "Thermal Desorption Spectroscopy as a Quantitative Tool to Determine the Hydrogen Content in Solids," *Thermochimica Acta*, vol. 404, pp. 251–258, 2003.

[48] A. M. de Jong and J. W. Niemantsverdriet, "Thermal Desorption Analysis: Comparative Test of Ten Commonly Applied Procedures," *Surf. Sci.*, vol. 233, pp. 355–365, 1990.

[49] T. Sugimoto and K. Fukutani, "Effects of Rotational-Symmetry Breaking on Physisorption of Ortho- and Para-H_2 on Ag(111)," *Phys. Rev. Lett.*, vol. 112, pp. 146101–1–146101–5, 2014.

[50] Hiden Analytical Inc. Email Correspondence, 2017.

[51] S. A. FitzGerald, H. O. H. Churchill, P. M. Korngut, C. B. Simmons, and Y. E. Strangas, "Cryogenic Apparatus for Diffuse Reflection Infrared Spectroscopy with High-Pressure Capabilities," *Rev. Sci. Instrum.*, vol. 77, pp. 093110–1–093110–4, 2006.

[52] Setra Systems, "Model 760 Vactron^{TM} Series: Capacitance Manometer - Absolute Pressure Transducer." U.S. Patent no. 4093915.

[53] MKS Instruments, Inc., "Analog 600 Series Selection Guide: Baratron® Absolute Capacitance Manometers," 2007.

[54] ABB Bomem, Inc., "The DA Product Line: PCDA SOFTWARE, User's Guide," July 1999. Revision 1.3.

[55] G. W. Chantry and J. W. Fleming, "Resolution Limits in Fourier Transform Spectrometry," *Infrared Phys.*, vol. 16, pp. 655–660, 1976.

[56] National Institute of Standards and Technology (NIST): Physical Meas. Laboratory, "Atomic Spectra Database." `https://www.nist.gov/pml/atomic-spectra-database`.

[57] I. Weinrauch, I. Savchenko, D. Denysenko, S. M. Souliou, H.-H. Kim, M. L. Tacon, L. L. Daemen, Y. Cheng, A. Mavrandonakis, A. J. Ramirez-Cuesta, D. Volkmer, G. Schütz, M. Hirscher, and T. Heine, "Capture of Heavy Hydrogen Isotopes in a Metal-Organic Framework with active Cu(I) sites," *Nat. Commun.*, vol. 8, p. 14496, 2017.

[58] Y. Liu, C. M. Brown, D. A. Neumann, H. Kabbour, and C. C. Ahn, "Hydrogen Adsorption in MOF-74 Studied by Inelastic Neutron Scattering," *MRS Proc.*, vol. 1041, 2008.

[59] D. A. King, "Thermal Desorption from Metal Surfaces: A Review," *Surf. Sci.*, vol. 47, pp. 384–402, 1975.

[60] S. A. FitzGerald, C. J. Pierce, J. L. C. Rowsell, E. D. Bloch, and J. A. Mason, "Highly Selective Quantum Sieving of D_2 from H_2 by a Metal-Organic Framework As Determined by Gas Manometry and Infrared Spectroscopy," *J. Am. Chem. Soc.*, vol. 135, pp. 9458–9464, 2013.

[61] M. T. Kapelewsi, T. Tunčevski, J. D. Tarver, H. Z. H. Jiang, K. E. Hurst, A. Ayala, T. Gennett, S. A. FitzGerald, C. M. Brown, and J. R. Long, "Evaluating Metal-Organic Frameworks for High-Pressure H_2 Storage: Record High Volumetric H_2 Capacity in Ni_2(m-dobdc)," *Energy Environ. Sci.*, 2017. Manuscript in Progress.

[62] P. M. Forster, J. Eckert, J.-S. Chang, S.-E. Park, G. Férey, and A. K. Cheetham, "Hydrogen Adsorption in Nanoporous Nickel(II) Phosphates," *J. Am. Chem. Soc.*, vol. 125, no. 5, pp. 1309–1312, 2003.

[63] A. Bétard and R. A. Fischer, "Metal-Organic Framework Thin Films: From Fundamentals to Applications," *Chem. Rev.*, vol. 112, pp. 1055–1083, 2012.

[64] L. Heinke, M. Tu, S. Wannapaiboon, R. A. Fischer, and C. Wöll, "Surface-Mounted Metal-Organic Frameworks for Applications in Sensing and Separation," *Microporous and Mesoporous Materials*, vol. 216, pp. 200–215, 2015.

[65] D. Zacher, O. Shekhah, C. Wöll, and R. A. Fischer, "Thin Films of Metal-Organic Frameworks," *Chem. Soc. Rev.*, vol. 38, pp. 1418–1429, 2009.

[66] H. Bux, F. Liang, Y. Li, J. Cravillon, M. Wiebcke, and J. Caro, "Zeolitic Imidazolate Framework Membrane with Molecular Sieving Properties by Microwave-Assisted Solvothermal Synthesis," *J. Am. Chem. Soc.*, vol. 131, pp. 16000–16001, 2009.

[67] H. Oh, K. S. Park, S. B. Kalidindi, R. A. Fischer, and M. Hirscher, "Quantum Cryo-sieving for Hydrogen Isotope Separation in Microporous Frameworks: An Experimental Study on the Correlation between Effective Quantum Sieving and Pore Size," *J. Mater. Chem. A*, vol. 1, pp. 3244–3248, 2013.

[68] H. Wu, W. Zhou, and T. Yildirim, "Hydrogen Storage in a Prototypical Zeolitic Imidazolate Framework-8," *J. Am. Chem. Soc.*, vol. 129, pp. 5314–5315, 2007.

[69] W. Zhou, H. Wu, M. R. Hartman, and T. Yildirim, "Hydrogen and Methane Adsorption in Metal-Organic Frameworks: A High-Pressure Volumetric Study," *J. Phys. Chem. C*, vol. 111, no. 44, pp. 16131–16137, 2007.